KU LEUVEN

ARENBERG DOCTORAL SCHOOL
Faculty of Science

Nuclear structure studies of rare francium isotopes using Collinear Resonance Ionization Spectroscopy (CRIS)

CERN-THESIS-2015-236
01/09/2015

Ivan Budinčević

Supervisor:
Prof. dr. G. Neyens

Dissertation presented in partial fulfillment of the requirements for the degree of Doctor in Science

September 2015

Nuclear structure studies of rare francium isotopes using Collinear Resonance Ionization Spectroscopy (CRIS)

Ivan BUDINČEVIĆ

Examination committee:
Prof. dr. M. Huyse, chair
Prof. dr. G. Neyens, supervisor
Prof. dr. P. Van Duppen
Prof. dr. R. Raabe
Prof. dr. N. Severijns
Prof. dr. E. Janssens

dr. K. Flanagan
(The University of Manchester,
Manchester, United Kingdom)

Dissertation presented in partial fulfillment of the requirements for the degree of Doctor in Science

September 2015

Uitgegeven in eigen beheer, Ivan Budinčević, Celestijnenlaan 200D box 2418, 3001 Leuven (Belgium)

Acknowledgements

"I'm bored" is a useless thing to say.
You live in a great, big, vast world
that you've seen none percent of.
Louis C.K.

This thesis marks the end of an important chapter in my life, a chapter filled with many exciting adventures and discoveries, but also many challenges. I am proud to have been able to contribute to the advancement of human knowledge, however humble the contribution may have been. However, I would have by no means been able to finish this journey without the help of many wonderful people, whom I am very happy to be able to thank here.

First and foremost, I would like to thank my supervisor Gerda Neyens, for giving me the opportunity to come to Leuven and to experience being a scientist at CERN. I have learned many things and had unforgettable experiences, all for which I am very grateful.

Secondly, I would like to thank the members of my Examination Committee: Mark Huyse, Piet Van Duppen, Riccardo Raabe, Nathal Severijns, Ewald Janssens and Kieran Flanagan. Thank you very much for your helpful comments and our interesting discussions concerning the thesis.

I am very grateful to have had such wonderful colleagues from the Nuclear Moments group: Jasna, Wouter, Hanne, Ronald, Ruben, Xiaofei, Stijn, Matthias and Sarina. Thank you for all the things I have learned during "Cultural Fridays", all the times you have helped me when I got stuck with theory, all the laughs we had and so much more.

I will also always be indebted to everyone from the CRIS team: Kieran, Jon, Kara, Thomas, Tom, Ilya, Mark, Shane, Greg, thank you all for being a very fun but also very efficient team, and helping me manage my way around

the CRIS beamline. I wish you countless more successful experiments, but I do hope they are not all on francium.

For the other members of the ISOLDE family: Frank, Vladimir, Bruce, Sebastien, Ralph, Tom, Laura, Stephan, Martin, Tomica, Magda and many others, thank you all for letting me borrow your tools and for being great neighbors.

I am very grateful to everyone from the secretariat: Isabelle, Fabienne, Sally and Danielle, to Luc and Bert for fun talks and their IT support, to Willy, Dries, Bart and everyone from the mechanical and electronics workshops for all of their hard work.

Luckily my four years at Leuven were not limited to just working, and I am very grateful for having wonderful colleagues who were not related to my field but with whom I had many interesting discussions over our Alma lunches, coffee breaks and beers in the Oude Markt. Hiwa, Gergely, Tomas, Camillo, Daniel, Manisha, Vera, Johana, Riccardo, Freddy, Sara, Deyan and everyone, thank you for all the fun conversations we had.

As for everyone outside of IKS, the volleyball gang, my Japanese class buddies, everyone from Dutch class, kung fu and salsa, all of my friends from Serbia, thank you for the countless fun times.

To my loving parents, thank you for all of your support throughout my entire life and for giving me so many opportunities. I will be forever grateful.

Finally, thank you Maro for all the fun things you have shown me, thank you Mali for always wanting to play with me and for visiting me in Leuven and in CERN and for always being my wonderful little brother, and thank you Tatjana, thank you for all of your support throughout my PhD and for all of the awesome adventures we had.

Thank you all.

Ivan
September 2015, Leuven

Preface

The goal of this PhD work was to study the structure of exotic francium isotopes by measuring their magnetic dipole and electric quadrupole moments as well as changes in mean-square charge radii, using the newly developed technique of Collinear Resonance Ionization Spectroscopy (CRIS).

The first experimental campaigns yielding hyperfine structure and alpha decay results for the francium isotopes $^{202-206}$Fr and ^{218m,219,229,231}Fr were performed in August and October 2012 at ISOLDE, CERN. These experiments used the low-resolution pulsed lasers from the RILIS group at ISOLDE, resulting in highly-sensitive background-free measurements, with a linewidth of 1.50(5) GHz. That was sufficient to deduce charge radii and magnetic moments of isomers and ground states, but not sufficient to resolve hyperfine components from isomers and ground states nor to determine quadrupole moments. Four articles were published as a result of this work. The first article by Cocolios *et al.* [1] gives a description of the CRIS experimental setup. The second article by Flanagan *et al.* [2] reports on the novelty and sensitivity of the CRIS technique and its application to the study of neutron-deficient francium isotopes and isomers down to ^{202}Fr. The third article by Lynch *et al.* [3] was the subject of the PhD thesis of Kara Lynch (University of Manchester) who focussed on the analysis and interpretation of the neutron-deficient francium isotopes using decay-assisted collinear resonance ionisation spectroscopy [4]. The fourth article by Budinčević *et al.* [5] is the core article of this PhD thesis and it is added in the discussion section. It focuses on the study of the neutron-rich francium isotopes in a region of reflection asymmetry. The measurement of the magnetic dipole moments provided insights into the orbital occupations of the valence protons in ^{219,229,231}Fr and supported the tentative spin assignments in ^{229,231}Fr, while the changes in mean-square charge radii provided additional support for the transitional character of ^{220}Fr, having weak octupole correlations, and showed that ^{228}Fr lies outside of the region where such octupole correlations cause reflection-asymmetric nuclear deformations.

During the ISOLDE long shutdown period, an upgrade to the CRIS off-line stable ion source was performed as part of this PhD work, enabling tests of a pulsed CW (continuous wave) laser system leading to high-resolution studies on francium isotopes in November 2014. Thanks to the improvement in resolution by nearly 2 orders of magnitude, the spectroscopic quadrupole moment of ^{219}Fr could be measured, which confirmed that the motion of the odd proton in this nucleus is decoupled from the core deformation. This was previously suggested from decay spectroscopy studies. A thorough description of the laser system technical developments, which forms the subject of the PhD thesis by Ruben de Groote, has been described in the paper by de Groote, Budinčević *et al.*[6], along with a short discussion on the evolution of the structure in the odd neutron-rich francium isotopes. This paper is given in the Appendix of this thesis, while a more extended discussion about shapes and deformation in the francium isotopes is given in the Discussion chapter. In summary, the following papers resulted from the experiments that were carried out as part of my PhD thesis:

1. **The Collinear Resonance Ionization Spectroscopy (CRIS) experimental setup at CERN-ISOLDE**
   T.E. Cocolios, H.H. Al Suradi, J. Billowes, I. Budinčević, R.P. de Groote, S. De Schepper, V.N. Fedosseev, K.T. Flanagan, S. Franchoo, R.F. Garcia Ruiz, H. Heylen, F. Le Blanc, K.M. Lynch, B.A. Marsh, P.J.R. Mason, G. Neyens, J. Papuga, T.J. Procter, M.M. Rajabali, R.E. Rossel, S. Rothe, G.S. Simpson, A.J. Smith, I. Strashnov, H.H. Stroke, D. Verney, P.M. Walker, K.D.A Wendt and R.T. Wood
   Nuclear Instruments and Methods in Physics Research B ***317****, 565-569 (2013)*

2. **Collinear Resonance Ionization Spectroscopy of Neutron-Deficient Francium Isotopes**
   K.T. Flanagan, K.M. Lynch, J. Billowes, M.L. Bissell, I. Budinčević, T.E. Cocolios, R.P. de Groote, S. De Schepper, V.N. Fedosseev, S. Franchoo, S. R.F. Garcia Ruiz, H. Heylen, B.A. Marsh, G. Neyens, T.J. Procter, R.E. Rossel, S. Rothe, I. Strashnov, H.H. Stroke, and K.D.A Wendt
   Physical Review Letters ***111****, 212501 (2013)*

3. **Decay-Assisted Laser Spectroscopy of Neutron-Deficient Francium**
   K.M. Lynch, J. Billowes, M.L. Bissell, I. Budinčević, T.E. Cocolios, R.P. de Groote, S. De Schepper, V.N. Fedosseev, K.T. Flanagan, S. Franchoo, R.F. Garcia Ruiz, H. Heylen, B.A. Marsh, G. Neyens, T.J. Procter, R.E. Rossel, S. Rothe, I. Strashnov, H.H. Stroke, and K.D.A Wendt
   Physical Review X ***4****, 011055 (2014)*

4. **Laser spectroscopy of francium isotopes at the borders of the region of reflection asymmetry**
   I. Budinčević, J. Billowes, M.L. Bissell, T.E. Cocolios, R.P. de Groote, S. De Schepper, V.N. Fedosseev, K.T. Flanagan, S. Franchoo, R.F. Garcia Ruiz, H. Heylen, K.M. Lynch, B.A. Marsh, G. Neyens, T.J. Procter, R.E. Rossel, S. Rothe, I. Strashnov, H.H. Stroke, and K.D.A Wendt
   Physical Review C ***90****, 014317 (2014)*

5. **Use of Continuous Wave Laser and Pockells Cell for Sensitive High-Resolution Collinear Resonance Ionization Spectroscopy**
   R.P. de Groote, I. Budinčević, J. Billowes, M.L. Bissell, T.E. Cocolios, G.J. Farooq-Smith, V.N. Fedosseev, K.T. Flanagan, S. Franchoo, R.F. Garcia Ruiz, H. Heylen, R. Li, K.M. Lynch, B.A. Marsh, G. Neyens, R.E. Rossel, S. Rothe, H.H. Stroke, K.D.A Wendt, S.G. Wilkins, and X. Yang
   Accepted in *Physical Review Letters*, August 2015

This thesis is organized in six chapters. Chapter 1 presents the previous studies performed on francium, introduces the region of reflection-asymmetric shapes, and motivates the development of the CRIS technique. Chapter 2 then introduces the theoretical concepts of the magnetic dipole moment, electric quadrupole moment and nuclear mean-square charge radii. Afterwards Chapter 3 describes radioactive ion beam production at the ISOLDE facility, introduces the basic concepts of laser spectroscopy, describes the CRIS beamline setup, and ends with a description of the technical developments of the new CRIS ion source. The following Chapter 4 discusses the analysis procedures for determining the nuclear moments and charge radii of the francium isotopes from the measured hyperfine spectra. Chapter 5 presents the physics discussion of these results, starting with an introduction into different types of nuclear deformations including octupole deformations, followed by Article I (item number 4 in the above list). Then the Coriolis interaction is introduced and the physics discussion of article number 5 from the above list is extended in detail. Finally, Chapter 6 provides a summary of the thesis, while also giving an outlook into future studies on francium and other isotopes using the CRIS technique. As previously mentioned, the Appendix of the thesis contains paper 5 from the above list, which will be referred to as Article II.

Abstract

It was known for many years that nuclei possessing certain numbers of protons (Z) and neutrons (N), called the magic numbers ($8, 20, 28, 50, 82, 126...$), exhibit characteristic behavior and are in general more stable than their neighboring isotopes. As the capabilities of producing isotopes with more extreme values of Z and N increased, it was realized that those spherical nuclei only represent a small fraction of the total number of isotopes and that most isotopes are deformed. In order to study exotic isotopes and their deformation, it was necessary to develop new experimental techniques that would be powerful enough to be able to cope with very small production yields, but precise enough to measure the nuclear properties (such as radii and moments) with relatively small uncertainties. One technique that can measure nuclear properties of scarcely produced isotopes is in-source resonant ionization, but this technique does not allow for sufficient precision to deduce nuclear quadrupole moments. Furthermore, this technique can only be applied to isotopes that are not surface-ionized, and is therefore not applicable for alkaline elements. On the other hand, a technique that can precisely measure atomic hyperfine structures and therefore precisely extract nuclear properties such as nuclear spin, magnetic dipole and electric quadrupole moments and mean-square charge radii is collinear laser spectroscopy with fluorescence detection. This technique however lacks the efficiency needed to study very exotic species. The aim of this PhD work was to apply a new technique which would be both efficient and precise: Collinear Resonance Ionization Spectroscopy (CRIS), to the study of the rare francium isotopes.

The interest in studying the francium ($Z = 87$) isotopes lies in the fact that its neutron-rich isotopes (around mass $A = 225$) are located in a region of the nuclear chart that exhibits a rare form of deformation: octupole deformation. Such type of deformation leads to reflection-asymmetric nuclear shapes (pear shapes). Previously the $^{220-228}$Fr isotopes were studied with collinear laser spectroscopy with fluorescence detection, which showed that the charge radii of these isotopes exhibited unusual behavior. This stimulated decay spectroscopy

studies to be performed on these francium isotopes, which showed that they exhibit several signatures of reflection asymmetry. The goal of this work was to extend the laser spectroscopy measurements to either side of this region, to determine the range in which these octupole deformations occur. Additionally, the francium isotopes with less than the magic $N = 126$ neutrons, were known to exhibit a lowering of the proton $3s^{-1}_{1/2}$ intruder state as more neutrons are removed, and it was the goal of these experimental campaigns to push the limits of the studied francium isotopes towards ^{199}Fr, where this state is predicted to be the ground state.

The experiments were performed in two periods. The first two experimental campaigns in August and October 2012 at ISOLDE, CERN, measured for the first time the magnetic dipole moments and changes in mean-square charge radii of the $^{202-206}$Fr (and their isomers) and the neutron rich ^{218m,219,229,231}Fr isotopes. The measurement of the hyperfine structure of ^{202}Fr, produced by less than 100 particles/s, was made possible due to the demonstrated $> 1\%$ high efficiency of the CRIS technique. The high resolution was not attained however, as it was limited by the 1.50(5) GHz linewidth of the used laser system. The measured magnetic dipole moments showed that the odd proton occupies the $1h_{9/2}$ shell model orbit in ^{219}Fr, while in ^{229,231}Fr it occupies the deformed Nilsson 1/2[400] orbital, originating from the $3s^{-1}_{1/2}$ intruder state. The mean-square charge radii results agreed with ^{220}Fr being a transitional isotope exhibiting weak octupole correlations, while ^{228}Fr lies outside of the region of reflection-asymmetric shapes.

Following these experiments, technical developments were performed as part of this work on the CRIS off-line ion source, leading to the possibility of providing stable beams of potassium. These beams were used to test the new laser scheme consisting of a narrowband continuous wave laser which was chopped by use of a Pockels cell, with this pulse being separated in time from the ionization laser pulse for reducing line broadening effects. This enabled the CRIS technique to reach the goal of high resolution, exemplified by the obtained 20(1) MHz wide hyperfine structure peaks of francium during a run in November 2014. The very well resolved hyperfine spectra allowed the extraction of the spectroscopic quadrupole moment of ^{219}Fr. This value showed that the motion of the odd proton is decoupled from the deformation-axis of the nucleus, as was the case in ^{221}Fr as well. This experiment showed that the CRIS technique is able to achieve high resolution without sacrificing efficiency, which has opened the door to many studies of exotic nuclei using the technique.

Beknopte samenvatting

Men weet reeds geruime tijd dat kernen met een bepaald aantal protonen (Z) en neutronen (N), de zogenoemde magische getallen ($8, 20, 28, 50, 82, 126...$), karakteristieke eigenschappen vertonen zoals een sferische grondtoestand en een verhoogde stabiliteit ten opzichte van de naburige isotopen. Door de spectaculaire vooruitgang in de productie van kernen met extreme waarden van Z en N (exotische kernen), heeft men ingezien dat zulke kernen eerder de uitzondering dan de regel zijn, en dat de meeste kernen in werkelijkheid vervormd zijn. Om deze exotische isotopen en hun vervorming te kunnen bestuderen, was de ontwikkeling van nieuwe experimentele technieken essentieel. Deze technieken moeten krachtig genoeg zijn om met lage productie-opbrengsten te kunnen werken, maar tegelijkertijd ook nauwkeurig genoeg om kerneigenschappen met een relatief kleine onzekerheid te kunnen meten. Een techniek die kerneigenschappen van in kleine hoeveelheden geproduceerde isotopen kan meten, is "in-source resonant ionization", maar deze techniek ontbreekt nauwkeurigheid. Anderzijds, een techniek die de atomaire hyperfijnstructuur nauwkeurig kan meten en vervolgens kerneigenschappen zoals kernspin, magnetisch dipool en elektrisch quadrupool moment en gemiddelde-kwadratische ladingsstraal kan bepalen, is collineaire laserspectroscopie met fluorescentiedetectie. Deze techniek ontbreekt helaas de efficiëntie die nodig is om zeer exotische isotopen te kunnen bestuderen. Het doel van dit doctoraat was een nieuwe techniek toe te passen, die zowel nauwkeurig en efficient is, namelijk Collinear Resonance Ionization Spectroscopy (CRIS), voor de studie van exotische franciumisotopen.

De neutron-rijke franciumisotopen ($Z = 87$) met massa $A = 225$ bevinden zich in een interessant gebied op de kernkaart, gekenmerkt door een weinig voorkomende kernvervorming: octopoolvervoming. Deze vervorming kan zich manifesteren door reflectie-asymmetrische kernvormen (peervorm). De $^{220-228}$Fr isotopen werden in het verleden reeds door collineair laserspectroscopie met fluorescentiedetectie bestudeerd, waaruit bleek dat de ladingsstralen van deze isotopen ongewoon gedrag vertonen. Deze observatie leidde dan tot

vervalspectroscopie-metingen waarin aangetoond werd dat deze isotopen ook andere tekenen van reflectie-asymmetrie vertonen. Het doel van dit werk was de laserspectroscopie metingen uit te breiden naar beide kanten van het gebied met reflectie-asymmetrie om te bepalen tot hoe ver deze octopoolvervorming voorkomt. Bovendien worden de franciumisotopen met minder neutronen dan (het magische) $N = 126$ gekenmerkt door een verlaging van de energie van de proton $3s^{-1}_{1/2}$ indringertoestand met een afnemend aantal neutronen. Een bijkomend doel van onze experimenten was dan ook de neutron-deficiënte franciumisotopen in de richting van ^{199}Fr ($N = 122$) te bestuderen, vermits in deze isotoop de indringtoestand als grondtoestand is voorspeld.

De experimenten werden uitgevoerd in de ISOLDE-facilteit in CERN en kunnen in twee reeksen worden opgedeeld. De eerste twee experimentele campagnes van augustus en oktober 2012, hebben voor de eerste keer de magnetische dipoolmomenten en veranderingen van gemiddelde-kwadratische ladingsstralen van de $^{202-206}$Fr (en hun isomeren) en de neutron-rijke ^{218m,219,229,231}Fr isotopen gemeten. De meting van de hyperfijnstructuur van ^{202}Fr, geproduceerd met minder dan 100 deeltjes/s, werd mogelijk gemaakt door de gedemonstreerde $> 1\%$ hoge efficiëntie van de CRIS-techniek. Met een 1.50(5) GHz lijnbreedte van het gebruikte lasersysteem, werd de vooropgestelde hoge resolutie helaas niet bereikt. De gemeten magnetische dipool-momenten toonden aan dat het oneven proton het $1h_{9/2}$ schilmodel-orbitaal bezet in ^{219}Fr, terwijl in ^{229,231}Fr het vervormde Nilsson 1/2[400] orbitaal, afkomstig de spherische $3s^{-1}_{1/2}$ orbitaal, wordt bezet. De resultaten in verband met de gemiddelde-kwadratische ladingsstraal zijn consistent met de interpretatie dat ^{220}Fr een overgangsisotoop is, die zwakke octopoolcorrelaties vertoont, terwijl ^{228}Fr buiten de regio van reflectie-asymmetrische vormen ligt.

Behalve deze experimenten, werden ook technische ontwikkelingen aan de CRIS off-line ionenbron uitgevoerd als deel van dit doctoraat. Deze hebben geleid tot de mogelijkheid om stabiele ionenbundels van kalium naar de CRIS bundellijn te sturen. Deze bundels werden gebruikt om het nieuwe lasersysteem te testen. Dit bestond uit een cw laser voor de resonante excitatie van de Fr hyperfijnniveaus. Door het gebruik van een Pockels cell werd de amplitude van de cw laser straal gemoduleerd, zodat een gepulst cw-signaal met de Fr atomen interageert. Deze resonante excitatiepuls werd gevolgd door een gepulste ionisatie stap met een gepulste Nd:YAG laser. De gemoduleerde cw laserpuls wordt in de tijd gescheiden van de ionisatie stap, wat de lijnverbredende effecten verminderde. Hierdoor kon de CRIS techniek het doel van hoge resolutie bereiken, experimenteel aangetoond door de meting van 20(1) MHz brede hyperfijnstructuur-pieken van francium (november 2014). Door de uitstekende resolutie van de hyperfijn-spectra, was het mogelijk om de spectroscopisch quadrupool-moment van ^{219}Fr te bepalen. Deze waarde toonde dat de beweging

van het oneven proton ontkoppeld is van de deformatie van de kern, zoals het geval was in ^{221}Fr. Tevens bewees dit experiment dat de CRIS techniek hoge resolutie kan bereiken zonder in te boeten op efficiëntie. Dit opent de deur voor onderzoek van zeer exotische kernen.

Contents

List of Figures

List of Tables

Chapter 1

Motivation

This chapter introduces the francium isotopes and the work that has previously been performed on them, showing that they exhibit signatures of reflection-asymmetric shapes. The region of the nuclear chart around francium where such shapes are observed is described in the subsequent section. The final section of this chapter provides a motivation for developing the Collinear Resonance Ionization Spectroscopy (CRIS) technique, which is capable of measuring basic nuclear properties such as the spin, magnetic dipole moment, electrical quadrupole moment and change in mean-square charge radii in a model independent way, and is capable of doing this for radioactive isotopes produced with rates as low as 100 atoms/s.

1.1 Previous studies on francium

Investigating the properties of francium has always been challenging, due to the fact that this element has no stable isotopes, with the lifetimes of the known francium isotopes ranging from 86(5) ns for ^{215}Fr [23] up to 22.00(7) min for ^{223}Fr [24]. It is estimated that there is less than 30 g of francium present in the earth's crust at any given point [25]. Therefore, extensive studies on the radioactive isotopes of francium could only be performed at radioactive isotope production facilities, with the first laser spectroscopy measurements being performed on francium in 1978 by Liberman et al. [26] at the ISOLDE facility, which will be introduced in Chapter 3. In this experiment the wavelength of the atomic transition line $7s\ ^2S_{1/2} - 7p\ ^2P_{3/2}$ was for the first time determined to be $\lambda = 717.7(1)$ nm. This transition was studied via optical pumping

by interaction with a tunable laser with an atomic jet of ^{211}Fr atoms, after which a sextupole magnet separated the differently populated magnetic states, which were subsequently sent through a mass spectrometer and detected by an electron multiplier. The measurements were repeated in 1980 by Liberman et al. [25] confirming the transition wavelength and extending the study to the hyperfine structure constants of the ground and excited state $A(7s\ ^2S_{1/2})$ and $A(7p\ ^2P_{3/2})$ and the isotope shifts of the $^{208-213}$Fr isotopes. The transition $7s\ ^2S_{1/2} - 7p\ ^2P_{1/2}$ was studied by Bendali et al. in 1984 [27] by applying the same technique on ^{211}Fr. The transition wavelength was determined to be $\lambda = 816.90(2)$ nm.

The work on francium using the technique previously described of optical pumping of an atomic jet by laser light was continued by Coc et al. [28], extending the study to the isotopes $^{207-213,220-228}$Fr. Note that the isotopes $^{214-219}$Fr could not be measured because of their short lifetime (between 86(5) ns and 20(2) ms) and thus lower production yield at ISOLDE. A following publication in 1987 by the same authors [29] reported a re-analysis of the previous data set using a more efficient fitting routine in order to separate the hyperfine structure peaks more efficiently. One of the more interesting findings in those studies, was the inversion of the odd-even staggering order of the isotope shift for the isotopes $^{222-225}$Fr. This effect will be explained in more detail in Chapter 5. The same effect in the isotope shift has been observed in the neighboring radium and radon isotopes [30, 31] and has been associated with the presence of octupole deformations. The nuclei in this region of the nuclear chart, centered approximately around ^{225}Ac [10], are known to exhibit signs of reflection-asymmetric shapes. These rare types of deformations, along with the region of the chart close to francium in which such deformations have been observed, are introduced in the next section.

Besides the laser spectroscopy studies, the neutron-rich francium isotopes were also studied in the past using nuclear decay spectroscopy. Liang *et al.* [18] studied the nuclear level structure of ^{219}Fr by measuring α-decay from the parent ^{223}Ac. They concluded that the nuclear energy levels could be organized into $K^\pi = \frac{1}{2}^\pm, \frac{3}{2}^\pm, \frac{5}{2}^\pm$ parity doublet rotational bands, which are a sign of the presence of nucelar octupole deformations [17]. The ground state spin of $I = 9/2$ for ^{219}Fr was interpreted as a consequence of the decoupled nature of this nucleus, leading to a changing level ordering within the $K^\pi = \frac{1}{2}^\pm$ bands. The parity doublet and decoupling concepts will be discussed in Chapter 5. The odd-odd isotope ^{220}Fr was studied by α-decay spectroscopy of ^{224}Ac [32]. A parity doublet $K^\pi = 1^\pm$ band was observed which again implies octupole deformations, but the α-decay transition rates implied a transitional nature of this nucleus between quadrupole-octupole deformation and a more spherical shape. The isotope ^{221}Fr was studied by α-decay spectroscopy of ^{225}Ac [33, 34]

and was interpreted as having $K^\pi = \frac{1}{2}^\pm, \frac{3}{2}^\pm$ parity doublet rotational bands where the $K^\pi = \frac{1}{2}^\pm$ are also of a decoupled nature as in ^{219}Fr.

Decay spectroscopy was also used to study the nuclear structure of ^{223}Fr by studying the γ-rays following the β^--decay of ^{223}Rn [35]. The obtained nuclear level structure for ^{223}Fr was interpreted in terms of $K^\pi = \frac{1}{2}^\pm, \frac{3}{2}^\pm$ doublet bands. The obtained level structure was found to be in good agreement with theoretical predictions of a reflection-asymmetric rotor model which includes octupole deformations [8], which is introduced in Chapter 5. The isotope ^{225}Fr has been studied by Burke *et al.* [36], by γ-ray and conversion-electron spectroscopy following the β-decay of ^{225}Rn and by a nuclear reaction ^{226}Ra(t, α)^{225}Fr during which a proton is taken from ^{226}Ra by a tritium nucleus ^{3}H which turns into an α-particle, leaving ^{225}Fr as the reaction product. Rotational bands of both parities for $K = \frac{1}{2}, \frac{3}{2}$ were observed, but could not be conclusively interpreted as belonging to parity doublets. Electric dipole (E1) transition rates, which are another sign of reflection asymmetric shapes [17], between the $K^\pi = \frac{3}{2}^\pm$ bands were of an intermediate character between nuclei with reflection-symmetric shapes and octupole deformed ones. Also the (t, α) cross sections studied in the same work were in better agreement with a reflection symmetric nuclear shape. The final conclusion by Burke *et al.* [36] was that octupole correlations are important in ^{225}Fr, but that there is no large stable octupole deformation. Finally, the isotope ^{227}Fr was studied by Kurcewicz *et al.* [37], via the γ-rays following the β^--decay of ^{227}Rn. The nuclear energy levels were interpreted in terms of seven rotational bands, however none of them could conclusively be determined to form a parity doublet band. Observed E1 transition rates between the lowest $K^\pi = \frac{3}{2}^\pm$ bands were consistent with the transitional character of ^{227}Fr, but still implied some octupole correlations.

1.2 Octupole deformations and the region of reflection asymmetry

Stable nuclei possessing a magic number of protons and neutrons $Z, N = 2, 8, 20, 28, 50, 82, 126$ are spherical in shape. This reflects the fact that the protons and neutrons in these nuclei occupy closed shells. This greatly reduces the correlations between protons and neutrons and also reduces the probability for nucleon excitations across the shell gaps. Both phenomena are the cause of nuclear deformations. However, only a small fraction of the nuclear chart consists of such spherical nuclei, as most known isotopes have a number of protons or neutrons different from the magic numbers. The majority of the nuclei exhibits quadrupole-deformed shapes, which will be elaborated upon in Chapter 5.

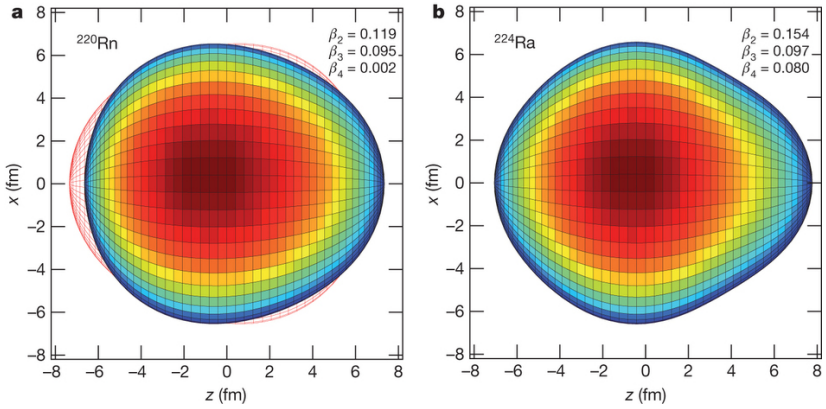

Figure 1.1: Figure taken from [7]. Panel **a** shows the vibrational character of the shape of ^{220}Rn in the difference of the surface and the red line, while panel **b** shows the statically deformed pear-shape of ^{224}Ra. The nuclear shapes were determined by calculating the deformation parameters β_2, β_3 from the measured intrinsic moments Q_2 and Q_3 by using equations 2.23, 2.26,2.27 from [8] and using the theoretical values for β_4 from [9].

A more exotic form of deformation, which has been suggested to exist for the first time in the 1950s, are deformations that are asymmetric under reflection, such as a pear shape (Fig. 1.1) [38]. Recently, the research on these distinct types of nuclear shapes has gained more momentum due to the possibility to produce increasingly more exotic isotopes at radioactive ion beam facilities. This area of research is also capturing the attention of a broader audience, such as the Nature publication by Gaffney et al. [7]. Figure 1.1, taken from that

article, shows the deduced nuclear shapes for ^{220}Rn and ^{224}Ra. These nuclei were studied by Coulomb excitation, a technique used to study excited nuclear states populated by electromagnetic interaction between an accelerated ion beam and a macroscopic target. The isotope ^{220}Rn has been interpreted as exhibiting octupole vibrations of the nuclear shape, while ^{224}Ra displays stable octupole deformation.

The importance of studying nuclei with octupole deformation lies in the fact that this is a rare form of deformation, the conditions for which are only available in particular regions of the nuclear chart with proton and neutron numbers $Z, N \approx 34, 56, 88, 134$ [17]. However, the study of such nuclei is additionally important for weak interaction studies. The presence of parity doublet bands which are close in energy can be used to study various parity non-conservation effects (PNC) in nuclei [39]. As for francium, this element is also interesting for studies of PNC effects via the nuclear anapole moment [40]. The anapole moment is a parity non-convserving time-reversal conserving nuclear moment that arises from weak interactions between the nucleons. Due to this moment, hyperfine E1 transitions which would otherwise be parity forbiden, become possible. In francium the nuclear anapole moment arises from the interaction of the valence nucleons with the core. Francium is interesting for such studies since the effects are proportional to Z and the atomic PNC (APNC) effects are predicted to be very large [41]. Due to this and the relatively simple atomic structure of francium with one valence electron, a dedicated facility called the Francium Trapping Facility [41], has been established at the TRIUMPH facility in Vancouver, Canada [42], in order to study these APNC effects in francium.

As mentioned in the previous section, the francium, radon and radium isotopes are located close to the actinide region of the nuclear chart which has been associated with quadrupole-octupole deformations [10]. This region is centered approximately around ^{225}Ac and is illustrated in Fig. 1.2. Raymond K. Sheline [10] defined this region in 1987 by comparing the experimentally known ground state spins of the isotopes in the region with predictions of an axially-symmetric but reflection-asymmetric model using a folded Yukawa nuclear potential [11]. In essence this model is used to predict the properties of nuclei possessing quadrupole-octupole-deformed shapes. The isotopes that have shown good agreement with the predictions of the model are within the solid lines in Fig. 1.2, while the isotopes close to the dashed lines are within a transition region in which the determination of the presence of octupole-deformed shapes is more ambiguous.

The spins of the odd-A francium isotopes ^{221,223,225}Fr agree with the predictions of the model, while the spins of the even-A francium isotopes ^{220,222,224,226}Fr were treated in a separate publication by Sheline [33] and also seemed to agree with the octupole-deformed model predictions. In [10], ^{227}Fr is

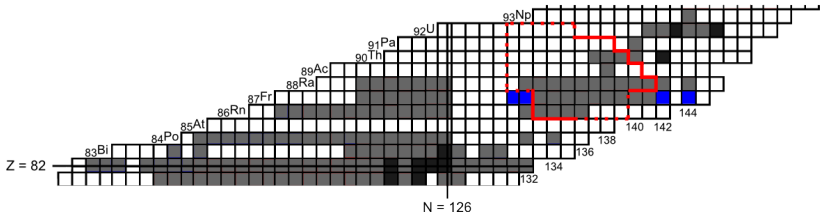

Figure 1.2: The actinide region of reflection asymmetry as defined by Sheline [10]. The isotopes within the solid line agree well with theoretical predictions for nuclei with reflection-asymmetric shapes [11]. The isotopes around the dashed lines are in a transition region where the determination of the presence of octupole-deformed shapes is more ambiguous. The isotopes in gray have been studied before 2010 by laser spectroscopy [12]. The isotopes in blue are ^{218m,219,229,231}Fr, measured in this PhD work.

placed outside of the region of reflection-asymmetric shapes, since the ground-state spin can be well explained by the normal Nilsson orbital [400 1/2]. The isotope ^{219}Fr is also not considered to be inside this region, due to the low hindrance factor of HF = 1.2 [43] for the alpha decay to the known shell-model $h_{9/2}$ [44] state in ^{215}At. However as mentioned in the previous section, this isotope also exhibits parity doublets with large decoupling parameters [18, 45], which are a sign of octupole deformation. Hence this isotope is considered to have transitional character between quadrupole-octupole-deformed shapes and spherical symmetry.

As mentioned in the previous section, the most neutron deficient francium isotope belonging to the region of reflection asymmetry that was studied by laser spectroscopy [28] was ^{220}Fr, while on the neutron rich side it was ^{228}Fr. The aim of this PhD work was to extend these measurements on both sides of this region using the new technique of Collinear Resonance Ionization Spectroscopy - CRIS.

1.3 Developing efficient high-resolution laser spectroscopy

A powerful method for determining, in a model independent way, the values of nuclear observables such as the magnetic dipole and electric quadrupole moments, nuclear spin and changes in mean-square charge radii is laser spectroscopy on radioactive ion beams. The values of these observables are determined by studying the atomic hyperfine structure via the interaction of laser light with the radioactive ions. The hyperfine structure and its relation to the magnetic dipole and electric quadrupole moments will be explained in Chapter 2.

Laser spectroscopy has provided information about the nuclear structure of exotic isotopes for the past half a century. During this time a significant portion of the known nuclear chart has been investigated, as can be seen in Fig. 1.3 (adapted from [12]). Extensive overviews of the different laser spectroscopy techniques and their developments can be found in [46, 47, 12].

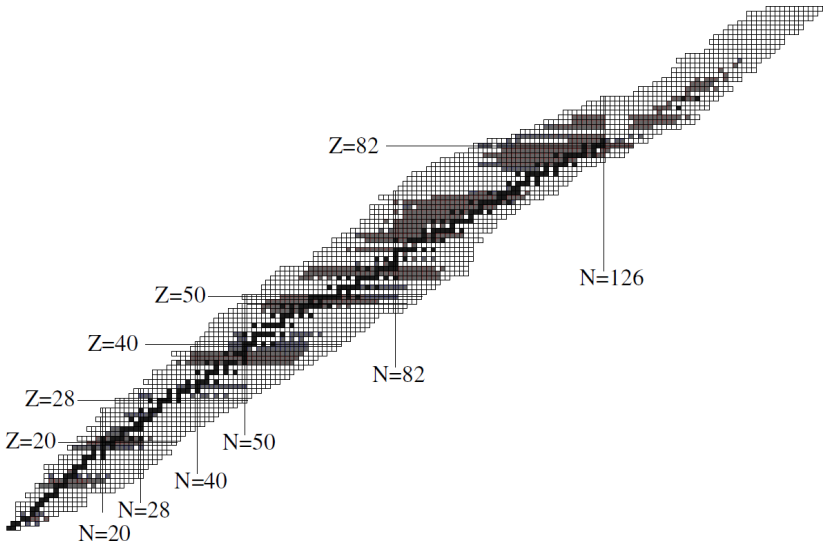

Figure 1.3: Overview of isotopes studied by optical measurements before 2010. The stable isotopes are colored in black, while the isotopes colored gray are radioactive and have been measured by laser spectroscopy. The isotopes in white are also radioactive but have not yet been measured by laser spectroscopy. The original figure is found in the review by Cheal and Flanagan [12].

Two of the most successful laser spectroscopy techniques that have been used to study the ground state properties of rarely produced radioactive nuclei are collinear laser spectroscopy with fluorescence detection and in-source laser spectroscopy. The major limitation for performing laser spectroscopy on an atomic (or ionic) ensemble is the Doppler broadening of the spectral lines due to the thermal motion of the atoms/ions. In the case of in-source laser spectroscopy within a hot ionizer cavity, the broadening originates from the temperature of the cavity and is typically on the order of several GHz [12]. In a gas-cell approach, where the atoms of interest are confined by a gas flow, the temperature is lower but additional issues arise such as the pressure broadening and pressure shift, both depending on the element and both being on the order of 10 MHz mbar^{-1} [48]. In order to reduce the Doppler broadening effect, collinear laser spectroscopy takes advantage of the fact that the total kinetic energy spread δE of an ion ensemble leaving a source will remain constant under acceleration by an electrostatic field

$$\delta E = \delta(\frac{1}{2}mv^2) = mv\delta v = const. \tag{1.1}$$

Since the product of the ion beam velocity spread δv with the beam velocity v is constant, the velocity spread will decrease as the beam is accelerated. This will lead to a decrease in the Doppler broadening of the ion ensemble and in the case of a typical beam energy of 40 keV after acceleration at ISOLDE, the Doppler broadening will reach the order of the natural linewidth of an atomic transition: $\sim$ 10 MHz.

In order to perform laser spectroscopy on such an accelerated ion (or atom) beam, it is necessary to determine when the laser frequency matches the frequency of a transition between the ionic (or atomic) hyperfine energy levels. The approach that has been extensively used in the past is the detection of photons from the de-excitation of the atom/ion back to the ground state after it had been resonantly excited by the laser light. Such collinear laser spectroscopy measurements using photon detection are performed at the COLLAPS beamline at ISOLDE [49]. While the technique benefits from the reduced Doppler broadening as discussed above, the detection of photons limits the total experimental efficiency and sensitivity. Since the photons are emitted in all directions, the detection efficiency will depend on the solid angle coverage of the photo-multiplier tubes (PMTs) used for the detection of the photons. Additionally, the sensitivity is reduced due to a significant source of background caused by non-resonant laser photons that scatter from the walls of the vacuum chamber and are detected by the PMTs. In total, this limits the use of the technique to the study of isotopes with yields on the order of $> 10^6$ atoms/s. However, with the recent installation of an ion cooler/buncher in front of the

HRS mass separator at ISOLDE, it is possible to correlate the photon detection with the passage of the atom (ion) bunch in front of the detectors. As a typical bunch length is of the order of 10 μs, and the typical bunching time is of the order of 100 ms, the photon background counts can be reduced by a factor 10^4, now allowing experiments of beams of typically 10^4 ions/s. In optimum conditions this can be extended down to yields of 300 particles/s [50].

On the other hand, laser spectroscopy in a hot cavity or a gas cell provides access to the study of isotopes with production rates as low as a few particles per second [51, 52, 53, 54], due to the higher detection efficiency of ion detection. This overcomes the solid angle constraints faced when working with photon detection, since the ions can be guided by beam optics elements and in principle 100% of the ions can reach the detection region. The scattered laser light also does not contribute to the background rate when working with ions. So if non-resonantly produced ions can be avoided, such experiments can provide nearly background-free conditions and therefore give a further enhancement in the signal-to-noise ratio (and thus sensitivity). As mentioned above, the drawback of performing laser spectroscopy in a hot cavity or a gas cell is the limited resolution of the hyperfine spectral lines that can be obtained. The typical linewidths range from 1 to 4 GHz, but developments are ongoing to reduce these widths further by performing the resonant ionization not in the gas-cell but in the colder gas jet [55, 56] or with two-photon spectroscopy [12].

Combining the high-resolution inherent with performing laser spectroscopy on an accelerated ion beam with the high detection efficiency and the possibility of creating background-free conditions using ion detection forms the basis of the Collinear Resonance Ionization Spectroscopy (CRIS) technique. The development of this technique is one of the key motivations for this PhD work. The CRIS technique and experimental setup at ISOLDE will be extensively described in Chapter 3, while the first physics results obtained from using the technique on the neutron rich francium isotopes will be discussed in Chapter 5.

Chapter 2

Nuclear moments and charge radii

This chapter will begin by explaining the hyperfine structure of the atomic energy levels, the study of which allows the extraction of the nuclear magnetic dipole and electric quadrupole moments, which are then explained in the subsequent sections. The following section describes the origin of the optical isotope shift from the field and mass shifts and the connection of the isotope shift with the nuclear mean-square charge radius. The final section explains how the field and mass shift constants needed for extracting the mean-square charge radius from the isotope shift can be determined by using the King plot method.

2.1 Hyperfine structure

Laser spectroscopy is a very powerful technique due to the fact that it is able to extract nuclear structure information in a nuclear-model-independent way by studying the atomic structure. The atomic fine structure energy levels of a single electron are defined by the quantum numbers n, l, j, where n is the principal electron quantum number, l is the electron angular momentum quantum number and j represents the total angular momentum of the electron which is a result of the coupling between l and the intrinsic spin of the electron s. The electron cloud for multi-electron configurations is labelled by similar quantum numbers L (total orbital momentum), J (total spin) and S (total intrinsic spin), which are composed of the single-electron quanta.

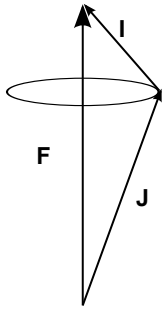

Figure 2.1: Coupling of the atomic angular momentum $\boldsymbol{J}$ and nuclear spin $\boldsymbol{I}$ vectors to the new total angular momentum $\boldsymbol{F}$.

The electromagnetic interaction between the nucleus and the orbiting electrons couples the total angular momentum vector of an atomic level $\boldsymbol{J}$ with the nuclear spin vector $\boldsymbol{I}$, giving rise to a new total angular momentum $\boldsymbol{F}$

$$\boldsymbol{F} = \boldsymbol{J} + \boldsymbol{I}. \tag{2.1}$$

The values of the $\boldsymbol{F}$ projections range from $|I - J| < F < |I + J|$ corresponding to the hyperfine structure energy levels. The hyperfine energy levels can be calculated by adding the contributions from the interaction of the nucleus with the orbiting electrons to the energy W_J of the unperturbed atomic multiplet energy level [57]

$$W_F = W_J + \frac{AC}{2} + B\frac{\frac{3}{4}C(C+1) - I(I+1)J(J+1)}{2I(2I-1)J(2J-1)} \tag{2.2}$$

where

$$C = F(F+1) - I(I+1) - J(J+1)$$

$$A = \frac{\mu_I \overline{H(0)}}{IJ}$$

$$B = eQ\overline{\varphi_{JJ}(0)}.$$

In Eq. (2.2) the second term with $A = \frac{\mu_I \overline{H(0)}}{IJ}$ represents the perturbation on the atomic energy level originating from the magnetic interaction between the nucleus and the orbital electrons. Here $\overline{H(0)}$ is the time-averaged magnetic field produced by the electrons at the site of the nucleus, while μ_I is the

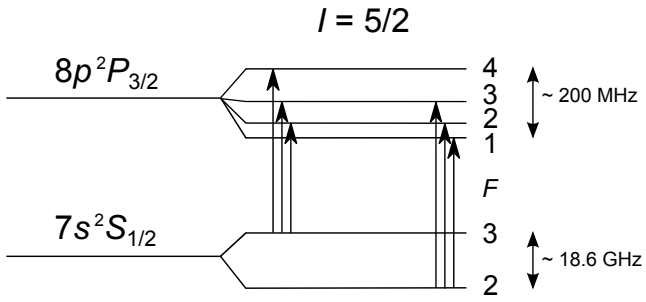

Figure 2.2: Example hyperfine structure splitting of the atomic fine energy levels. The levels presented in the figure are the $7s\ ^2S_{1/2}$ and $8p\ ^2P_{3/2}$ atomic fine structure levels of francium, which split into two and four hyperfine energy levels respectively. The level splittings in the figure are obtained by using Eq. 2.2.

magnetic dipole moment of the nucleus, which will be explained in Sec 2.2. The term A represents the first order contribution of the magnetic multipole moment operator $\mathbf{M}_q^k$, namely the magnetic dipole contribution. It can be analytically proven [58], that only odd-k order magnetic multipole moments are non-zero, meaning that the first higher order magnetic multipole moment would be the octupole magnetic moment. The effect of this moment on the hyperfine splitting can be neglected in most cases, as it is weaker than the magnetic dipole by a factor of 10^{-5} [59]. The third term of Eq. (2.2) with $B = eQ_s\overline{\varphi_{JJ}(0)}$ originates from the electrostatic interaction between the non-spherical nuclear charge distribution and the atomic electrons. Here $\overline{\varphi_{JJ}(0)}$ is the average of the gradient of the electron clouds electric field at the site of the nucleus and Q_s is the spectroscopic electric quadrupole moment, which will be discussed in Sec. 2.3.

An example of the effect of the hyperfine splitting on the atomic levels is given in Fig. 2.2, showing the hyperfine structure of ^{221}Fr. The atomic levels are $7s\ ^2S_{1/2}$ with $J = 1/2$ and $8p\ ^2P_{3/2}$ with $J = 3/2$. Since the nuclear spin of ^{221}Fr is $I = 5/2$, the $7s\ ^2S_{1/2}$ level splits into the $F = 2, 3$ levels while the $8p\ ^2P_{3/2}$ level is split into levels with $F = 1, 2, 3, 4$. In Fig. 2.2 the relative positions of the hyperfine energy levels within a multiplet are drawn to scale compared to the unperturbed atomic fine energy level, but the relative splitting between the two multiplets is not to scale. The splitting of ~ 18.6 GHz for the $7s\ ^2S_{1/2}$ level is much larger than the ~ 200 MHz splitting of the $8p\ ^2P_{3/2}$ hyperfine multiplet. It is clear from this example that the experimental resolution needs to be better than 100 MHz in order to resolve the 6 possible hyperfine transitions (arrows in Fig. 2.2).

2.2 Magnetic dipole moment

The nuclear magnetic moment originates from the magnetic field generated by the proton current of the nucleus and the intrinsic magnetic field of the nucleons generated by their intrinsic spin $s = 1/2$. The magnetic dipole operator that takes these contributions into account can be expressed as [60]:

$$\boldsymbol{\mu} = \sum_{i=1}^{A} g_L^{(i)} \mathbf{L}^{(i)} + \sum_{i=1}^{A} g_S^{(i)} \mathbf{S}^{(i)}, \tag{2.4}$$

$g_L^{(i)}$ and $g_S^{(i)}$ are the nuclear orbital and spin g-factors, while $\mathbf{L}^{(i)}$ and $\mathbf{S}^{(i)}$ represent the angular and spin momentum of the individual (i) nucleons. The free-nucleon orbital and spin g-factors for protons (π) and neutrons (ν) are: $g_l^\pi = 1, g_l^\nu = 0$, $g_s^\pi = +5.587, g_s^\nu = -3.826$ [60]. The magnetic dipole moment μ_I, is obtained by calculating the expectation value of the Z-projection of the magnetic moment operator $\boldsymbol{\mu}$:

$$\mu_I = \langle I, m = I | \boldsymbol{\mu_z} | I, m = I \rangle, \tag{2.5}$$

with μ_I being related to the nuclear spin via the gyromagnetic ratio g by: $\mu_I = gI\mu_N$. Here μ_N is the nuclear magneton, whose value is constant and given by:

$$\mu_N = \frac{e\hbar}{2m_p} = 5.05084 \cdot 10^{-27} J/T, \tag{2.6}$$

where e is the electronic charge, $\hbar = 1.054589 \cdot 10^{-34} J \cdot s$ and m_p is the proton mass. For nuclei near closed-shells (in a single-particle shell model), the magnetic dipole moment is determined by the moment of the unpaired valence nucleon with total angular momentum $\boldsymbol{j}$ and orbital momentum $\boldsymbol{l}$. The magnetic dipole moment can then be expressed in terms of the free-nucleon orbital and spin g-factors and is called the Schmidt-moment [61]:

$$\mu(l + 1/2) = \left[\left(j - \frac{1}{2} \right) g_l + \frac{1}{2} g_s \right] \mu_N, \tag{2.7a}$$

$$\mu(l - 1/2) = \frac{j}{j+1} \left[\left(j + \frac{3}{2} \right) g_l - \frac{1}{2} g_s \right] \mu_N. \tag{2.7b}$$

By calculating these values using the free-nucleon orbital and spin g_l, g_s factors, it is possible to estimate the Schmidt moment values and compare them to experimentally measured magnetic dipole moment values. It turns out that in most nuclei the experimental values differ from the Schmidt values and it becomes necessary to use effective g_s and g_l values to account for the interaction

of the valence nucleon with the rest of the nucleons in the core. In heavy-mass nuclei, the effective g_s-factor values are usually $60-70\%$ of the free-nucleon value, while the orbital g_l factor is modified by less than 10%. Calculating the magnetic moment using the effective g-factor values gives the effective magnetic moments $\mu^{\pi}_{\text{eff}}, \mu^{\nu}_{\text{eff}}$. Comparing these values to the experimentally determined magnetic moment values provides a probe for the shell model orbital occupancy of the unpaired valence nucleon(s).

In the case of an odd-odd nucleus it is necessary to calculate the total magnetic moment from the contributions of the unpaired proton and neutron. Since the magnetic moment operator is a single-body operator, the total magnetic moment can be calculated by decomposing the total wave function into its single-particle contributions and applying several additivity relations to these contributions [61, 62]. The final nuclear magnetic moment for a state described by a weak coupling between the protons and neutrons can be expressed as:

$$\mu_I = \frac{I}{2}\left[\frac{\mu_\pi}{j_\pi} + \frac{\mu_\nu}{j_\nu} + \left(\frac{\mu_\pi}{j_\pi} - \frac{\mu_\nu}{j_\nu}\right)\frac{j_\pi(j_\pi+1) - j_\nu(j_\nu+1)}{I(I+1)}\right], \tag{2.8}$$

where μ_π, μ_ν are the magnetic moments and j_π, j_ν the nuclear orbits occupied by the unpaired proton and neutron.

Finally it is relevant to mention finite-size effects of the nucleus on the magnetic dipole moment. In the previous section the interaction between the orbiting electrons and the nucleus was described by approximating the nucleus to be of point-size. Accounting for the different size of the nucleus between different isotopes leads to the introduction of two effects. The first is the Bohr-Weisskopf(BW) effect [63, 64], which is a consequence of the difference of the nuclear magnetization distribution between isotopes. The second effect originates from the different electric charge distribution between isotopes and is called the Breit-Rosenthal (BR) effect [65], which is usually much smaller than the BW effect [66]. The combined contribution of these two effects is referred to as the hyperfine anomaly. The hyperfine anomaly was measured for the francium isotopes ^{206g,206m,207,209,213,221}Fr at the Francium Trapping Facility at TRIUMPH by Zhang *et al.* [67] and the values were found to be in good agreement with shell model predictions. The effect of the hyperfine anomaly was not considered as part of this PhD work, as the precision with which the new magnetic dipole moment values were extracted was not high enough to require considering such effects. Note that this was mostly due to the large error on the reference magnetic moment for ^{210}Fr, which is about 1%.

2.3 Electric quadrupole moment

The electric quadrupole moment operator can be expressed as [60]

$$\boldsymbol{Q_z} = e\sum_{k=1}^{A} g_L^{(k)}(3z_k^2 - r_k^2) \tag{2.9}$$

where $g_L^{(k)}$ is the orbital g-factor and (x_i, y_i, z_i) are the coordinates of the k-th nucleon and e is the electric charge. Since for free nucleons $g_L^{(\pi)} = 1$ and $g_L^{(\nu)} = 0$ the nuclear charge distribution will only depend on the orbital motion of the protons. Hence $g_L^{(k)}$ is usually replaced with 1 in Eq. (2.9). The experimentally observable spectroscopic quadrupole moment Q_s is defined as the expectation value of the quadrupole moment operator $\boldsymbol{Q_z}$ in the nuclear state with $m = I$, which can be written as a function of the reduced matrix element using the Wigner-Eckart theorem:

$$Q_s(I) = \langle I, m = I|\boldsymbol{Q_z}|I, m = I\rangle = \sqrt{\frac{I(2I-1)}{(2I+1)(2I+3)(I+1)}}(I\|Q\|I). \tag{2.10}$$

It is clear from Eq. (2.10) that when the nuclear spin $I = 0$ or $I = 1/2$, the spectroscopic quadrupole moment will vanish. This means that even though a nucleus with such a spin may possess an intrinsic quadrupole deformation (so a non-zero reduced matrix element), the quadrupole moment cannot be measured experimentally.

The quadrupole moment can also be expressed in terms of the spherical harmonics

$$\boldsymbol{Q_z} = \sqrt{\frac{16\pi}{5}}\sum_{i=1}^{A} e_i r_i^2 Y_2^0(\theta_i, \phi_i), \tag{2.11}$$

where $Y_2^0(\theta_i, \phi_i)$ is the zero-order second spherical harmonic. The quadrupole operator in the form of Eq. (2.11) can be applied to a nuclear state with its spin determined by a single nucleon in orbital j, and with $m = I$. By using then the Wigner-Eckart theorem with the full expression for the second spherical harmonic [62] on this result, an expression can be obtained for the single-particle quadrupole moment of an unpaired nucleon with angular momentum j:

$$Q_{\text{s.p.}} = -e_j\frac{2j-1}{2j+2}\langle r_j^2\rangle, \tag{2.12}$$

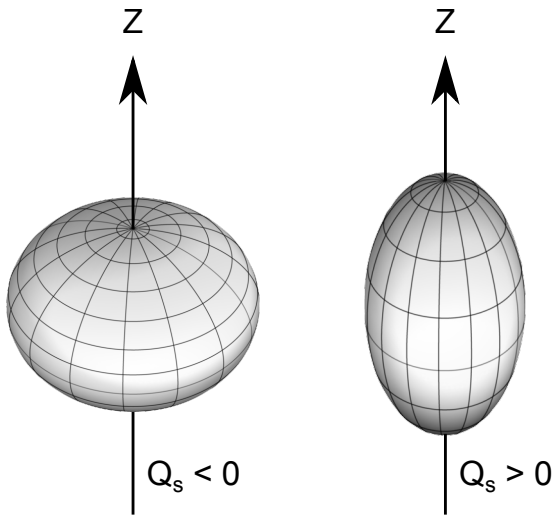

Figure 2.3: The different spectroscopic charge distributions originating from a single-particle quadrupole moment. In the case of $Q_s < 0$ an oblate distribution relative to the Z axis arises, while for $Q_s > 0$ the distribution is prolate.

where e_j represents the effective charge of the nucleon in orbital j, while $\langle r_j^2 \rangle$ is the mean-square charge radius for a nucleon in orbital j, which will be defined in Sec. 2.4.1. From Eq. (2.12) it is clear that a particle moving outside a closed shell will exhibit a negative quadrupole moment, generating an oblate charge distribution, as shown in Fig. 2.3. This is due to the fact that in the case of a $j = m$ state the particle density is localized in the equatorial plane. The greatest overlap of the core nucleons with the valence particle will then be in the equatorial plane, causing the oblate shape. Conversely, a shell with one hole will have a positive quadrupole moment, leading to a prolate charge distribution, as seen in Fig. 2.3.

2.4 Isotope Shift

While the magnetic dipole and electric quadrupole moments are nuclear observables that can be extracted from the hyperfine splitting of a single isotope, provided the electronic hyperfine fields can be quantified, the isotope shift is an observable determined from the differences between hyperfine spectra of two neighboring isotopes. For a given atomic transition, such as the transition between the $7s\ ^2S_{1/2}$ and $8p\ ^2P_{3/2}$ atomic levels in francium, the transition frequency between these fine structure levels ν^A in isotope A will be different than the transition frequency $\nu^{A^{\text{ref}}}$ of isotope A^{ref}. This difference is referred to as the isotope shift [68]:

$$\delta\nu_{IS}^{A,A^{\text{ref}}} = \nu^{A^{\text{ref}}} - \nu^{A}. \tag{2.13}$$

In general the isotope shift originates from two effects: the field shift $\delta\nu_{FS}^{A,A^{\text{ref}}}$ originating from the difference in charge distribution between two isotopes (or isomers) and the mass shift $\delta\nu_{MS}^{A,A^{\text{ref}}}$ originating from the difference in total nuclear mass between the two isotopes (or isomers). The total isotope shift can then be expressed as:

$$\delta\nu_{IS}^{A,A^{\text{ref}}} = \delta\nu_{FS}^{A,A^{\text{ref}}} + \delta\nu_{MS}^{A,A^{\text{ref}}} \tag{2.14}$$

2.4.1 Field Shift

To a first approximation, the nuclear charge distribution can be described as a uniform sphere with radius R_0:

$$R_0 = 1.2\ A^{1/3}\ \text{fm}, \tag{2.15}$$

where A is the atomic mass number. While this can serve as a good first approximation, it is in general not possible to accurately describe the nuclear charge distribution with a single radius, but several size parameters and spatial moments of certain distribution functions need to be taken into account [68]. An experimental observable which can be used to describe the general size of the charge distribution is the mean-square charge radius:

$$\langle r^2 \rangle = \frac{\int_0^R \rho_N(\boldsymbol{r}) r^2 \mathrm{d}\boldsymbol{r}}{\int_0^R \rho_N(\boldsymbol{r}) \mathrm{d}\boldsymbol{r}}, \tag{2.16}$$

where ρ_N is the nuclear charge density distribution and the denominator $\int_0^R \rho_N(\boldsymbol{r})\mathrm{d}\boldsymbol{r}$ represents the total nuclear charge Ze. The field shift contribution to the isotope shift originates from the difference in the size of the charge distribution between two isotopes. Using the approximation that the s electrons contribute most to the field shift effect (as these electrons have a high probability to occur inside the nuclear volume) and neglecting the screening effect of the other electrons, the field shift of an optical transition can be expressed as:

$$\delta\nu_{FS}^{A,A^{\mathrm{ref}}} = \pi\Delta|\psi(0)|^2 \frac{a_0^3}{Z} f(Z) \delta\langle r^2 \rangle^{A,A^{\mathrm{ref}}}, \tag{2.17}$$

where a_0 is the Bohr radius, $\Delta|\psi(0)|^2$ is the total non-relativistic change of the electron density at the site of the nucleus during an atomic transition, $f(Z)$ is a function that increases with Z and includes relativistic corrections to the change of electron density $\Delta|\psi(0)|^2$ [69] and $\delta\langle r^2 \rangle^{A,A^{\mathrm{ref}}}$ is the relative change in the mean-square charge radius between the two isotopes with masses A and A^{ref}. Optical transitions of the type $ns - n'p$ are most often used to study isotope shifts, since the electron density of s electrons at the nucleus is much larger than the density of p electrons, justifying the single-electron approximation used to derive Eq. (2.17).

2.4.2 Mass Shift

The mass shift contribution to the total isotope shift originates from the different center of mass motion of the nucleus between nuclei of different mass. The total mass shift can be expressed as:

$$\delta\nu_{MS}^{A,A^{\mathrm{ref}}} = \frac{A^{\mathrm{ref}} - A}{AA^{\mathrm{ref}}} (K_{NMS} + K_{SMS}), \tag{2.18}$$

where K_{NMS} is the normal mass shift and K_{SMS} the specific mass shift. As can be concluded from the $\frac{A^{\mathrm{ref}}-A}{AA^{\mathrm{ref}}}$ factor in Eq. (2.18), the mass shift has a significant contribution to the isotope shift for lighter-A nuclei. For heavier

nuclei the effect of the mass shift diminishes due to the small $\frac{1}{AA^{\text{ref}}}$ term. The normal mass shift K_{NMS} assumes that there are no correlations between the electrons and is calculated for a two-body system of an electron cloud and a nucleus. The normal mass shift can be calculated for a specific transition by using:

$$K_{NMS} = \frac{\nu_{exp}}{1822.88}\ (\text{GHz}), \tag{2.19}$$

where ν_{exp} is the experimentally studied atomic transition. The normal mass shift is always positive for the heavier isotope. The specific mass shift K_{SMS} on the other hand, can be positive or negative and depends on electron correlations and the specific properties of the atomic level [68]. Accurate calculations for the specific mass shift use an *ab initio* approach and have so far been successfully performed only for light elements with up to three-electrons [70]. For heavy nuclei, many effects within a large model space need to be taken into account such as relativistic, QED and correlation effects [71], limiting the accuracy of the calculations. The most common approach for determining the specific mass shift in heavy nuclei is by a comparison of isotopic shifts measured in two different transitions via a King plot [68]. This method will be outlined in Sec. 2.4.4.

2.4.3 Total Isotope Shift

By substituting Eq. (2.18) and Eq. (2.17) into Eq. (2.14), along with replacing $\pi\Delta|\psi(0)|^2\frac{a_0^3}{Z}f(Z)$ with F, the field shift constant and $K_{SMS}+K_{NMS}$ with M, the mass shift constant, the total isotope shift can be expressed as:

$$\delta\nu_{IS}^{A,A^{\text{ref}}} = M\frac{A^{\text{ref}}-A}{AA^{\text{ref}}} + F\delta\langle r^2\rangle^{A,A^{\text{ref}}}. \tag{2.20}$$

By writing the isotope shift this way it is clear that both the field and mass shift contributions are separated into an atomic part: F and M and a nuclear part: $\delta\langle r^2\rangle^{A,A^{\text{ref}}}$ and $\frac{A^{\text{ref}}-A}{AA^{\text{ref}}}$. By measuring the experimental isotope shift and calculating the atomic contributions or obtaining them via a King plot, the nuclear mean-square charge radius can be determined.

2.4.4 The King Plot Method

In some cases the field and mass shift factors F and M in Eq. (2.20) may not be known for a given transition. However, if these values are already known for another transition of the same element (from calculations or from other techniques), these known values can be used to estimate the field and mass shift factors for the transition of interest. This can be done using the King plot method [72]. In this method, the isotope shifts of two atomic transitions, $\delta\nu_1^{A,A^{\mathrm{ref}}}$ and $\delta\nu_2^{A,A^{\mathrm{ref}}}$, are both multiplied by the same mass factor $\mu_{A,A^{\mathrm{ref}}}$ in Eq. (2.20), with

$$\mu_{A,A^{\mathrm{ref}}} = \frac{AA^{\mathrm{ref}}}{A - A^{\mathrm{ref}}}. \tag{2.21}$$

By multiplying the isotope shifts with this factor, the nuclear mass dependence is removed for these "modified" isotope shifts which can now be written as:

$$\mu_{A,A^{\mathrm{ref}}}\delta\nu_1^{A,A^{\mathrm{ref}}} = M_1 + \mu_{A,A^{\mathrm{ref}}}F_1\delta\langle r^2\rangle^{A,A^{\mathrm{ref}}} \tag{2.22a}$$

$$\mu_{A,A^{\mathrm{ref}}}\delta\nu_2^{A,A^{\mathrm{ref}}} = M_2 + \mu_{A,A^{\mathrm{ref}}}F_2\delta\langle r^2\rangle^{A,A^{\mathrm{ref}}}. \tag{2.22b}$$

By calculating $\mu_{A,A^{\mathrm{ref}}}\delta\langle r^2\rangle^{A,A^{\mathrm{ref}}}$ from Eq. (2.22a) and substituting it into Eq. (2.22b), the expression relating the modified isotope shifts for the two transitions is obtained:

$$\mu_{A,A^{\mathrm{ref}}}\delta\nu_2^{A,A^{\mathrm{ref}}} = \frac{F_2}{F_1}\mu_{A,A^{\mathrm{ref}}}\delta\nu_1^{A,A^{\mathrm{ref}}} + M_2 - \frac{F_2}{F_1}M_1. \tag{2.23}$$

This represents a linear dependence between the modified isotope shifts of the two transitions with a gradient defined by the ratio of the field factors $\frac{F_2}{F_1}$ and an intercept of $M_2 - \frac{F_2}{F_1}M_1$. Thus, by knowing the isotope shift, field and mass shift values for transition 1, and measuring the isotope shift in transition 2, it is possible to extract the field and mass shift values of transition 2 by plotting the modified isotope shifts for both transitions with respect to each other and performing a linear fit using Eq. (2.23).

Chapter 3

Experimental setup and technical developments

This chapter starts by describing the process of radioactive ion beam production at ISOLDE. The next section briefly introduces some important concepts from laser spectroscopy, with the following section describing the ionization scheme of francium. The subsequent section describes the CRIS experimental beamline, with the different configurations that were used in the low- and high-resolution experimental campaigns. The final section of this Chapter gives an overview of the technical development work performed on the CRIS off-line ion source as part of this PhD work.

3.1 Radioactive ion beam production at ISOLDE

The Isotope Separator On-Line DEvice (ISOLDE) facility is located at CERN (Geneva, Switzerland). This facility was first established in 1967 and has since produced more than 600 isotopes of almost 70 different elements [73]. The production of this vast range of elements is done by using the Isotope Separation On-Line (ISOL) method. ISOLDE is one of the experimental facilities at CERN such as the Antiproton Decelerator (AD) [74], CERN Neutrinos to Gran Sasso [75], nTOF (neutron time-of-flight facility) [76], Compact Linear Collider [77] and others, with most notably the LHC (Large Hadron Collider) [78]. All these facilities use protons from CERN's large accelerator complex [79] to perform experiments.

The general layout of the ISOLDE facility is given in Fig. 3.1. ISOLDE receives protons from the Proton Synchrotron Booster [80] which are accelerated to 1.4 GeV (1 in Fig. 3.1). These protons impinge on a thick target (2 in Fig. 3.1) which can be one of over 25 different target materials [81], with the most commonly used one being uranium carbide. The use of a high-Z material enables the production of a large variety of radioactive species by spallation, fission and fragmentation reactions. The ISOLDE target is usually held at a high temperature ~ 2000 °C in order to facilitate the diffusion of the reaction products out of the target. Since francium is an alkaline element with a low ionization potential of 4.07 eV [82], it easily surface-ionizes in the hot target and is then extracted by an extractor electrode towards the mass separator. The concept of surface ionization which is also the basis of the CRIS off-line ion source, developed as part of this PhD work, will be explained in Sect. 3.5.1 of this chapter.

3.1.1 Mass separation

The ions formed in the target are extracted at an energy of $30-60$ keV and sent into the mass separator. There are two available mass separators at ISOLDE: the HRS high-resolution mass separator (4 in Fig. 3.1) and the GPS general purpose mass separator. The main advantage of the HRS separator is the high mass-resolving power $\frac{M}{\Delta M} \sim 5000$ [81], attained by using several electrostatic beam focusing elements in conjunction with a 90° and a 60° dipole magnet [83].

The GPS mass separator has a lower resolving power on the order of ~ 1000 [81]. One limitation to the resolving power originates from ion collisions with gas molecules during transport, which change the direction of the ions resulting in ions of neighboring masses being in the focal plane of the separator. This induces a minimum contamination of neighboring masses on the order of 10^{-5} in the mass range of $A = 200$ [84]. The main advantage of the GPS mass separator however, is the capability of simultaneously providing beams of different masses to the central ISOLDE beamline and the parasitic GHM and GLM beamlines. The masses that can be supplied to the side beamlines have to be in the range of $\pm 15\%$ of the mass in the central beamline. The selection of the masses is done by using electrostatic cylindrical deflection plates that can be moved in the focal plane of the GPS central double focusing 70° magnet [85].

3.1.2 Ion beam bunching using ISCOOL

For the experimental studies on francium performed as part of this PhD work, the ion beam was mass-separated using the HRS separator. The ion beam exiting

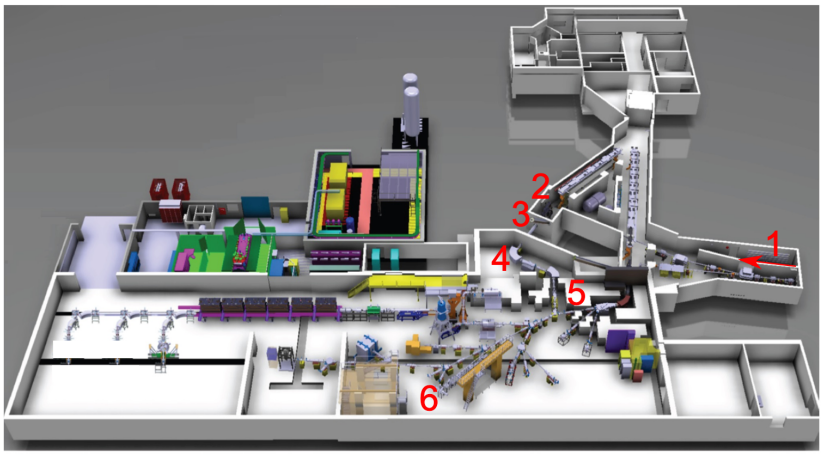

Figure 3.1: The general layout of the ISOLDE experimental hall: 1. 1.4 GeV proton beam from the PS booster, 2. HRS target, 3. RILIS laser ion source, 4. HRS separator, 5. ISCOOL cooler buncher, 6 CRIS beamline.

the separator is continuous, which is not optimal for measurements with a fixed periodic cycle, such as the pulse repetition rate of 30-100 Hz of the lasers used for the CRIS experiment, which will be explained in Sect. 3.4.1 and Sect. 3.4.2. Indeed, one of the first experiments to attempt resonant ionization spectroscopy in a collinear geometry [86], suffered from low experimental efficiency due to the duty cycle losses related to the use of a pulsed laser system exciting the continuous ion beam. By bunching and trapping the ions, it is possible to synchronize the laser firing with the release of the ion bunch, increasing the total experimental efficiency by several orders of magnitude. The ISCOOL buncher was installed in ISOLDE for the purpose of bunching the ion beam [87].

ISCOOL is a radio-frequency linearly segmented Paul trap. The entry point into the trap are injection electrodes that gradually decrease in potential with respect to the high potential of the HRS, while the central structure of ISCOOL is held at -100 V with respect to the HRS. The ions in the beam are confined in the transverse plane with respect to the beam axis by applying an RF-voltage (radio-frequency) of $V_{rf}\cos(\omega t)$ to a pair of parallel metal rods out of four total rods with the other pair supplied with an opposite voltage. The ions are guided in the longitudinal plane along the beam axis by means of a 0.2 V/cm electric field gradient generated by 25 segmented DC electrodes, positioned around the four RF rods [13]. The trap is filled with helium gas at a pressure of around 0.1 mbar which serves to slow down the ions via collisions. The ions

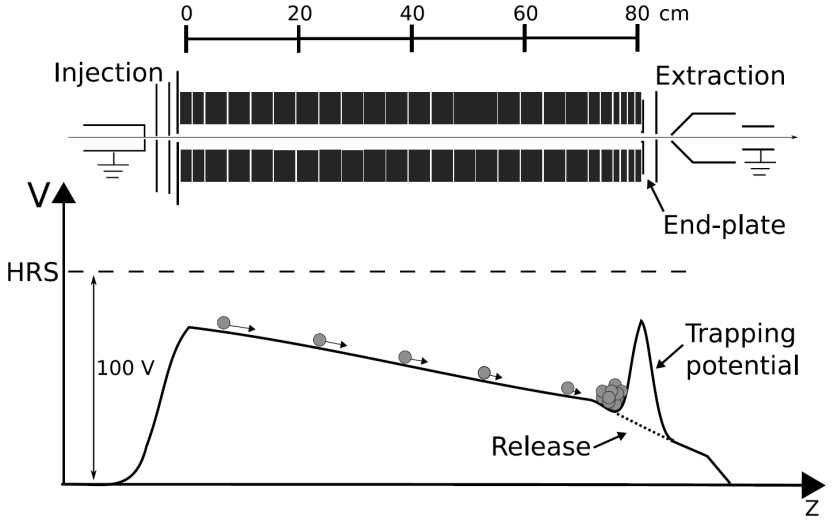

Figure 3.2: The shape of the trapping potential inside ISCOOL and electrode structure schematic, taken from [13]. The entire trap is held at a voltage of 100 V below the HRS high voltage. The ions are guided into the trap by injection electrodes, then pushed along the trap by a down-slopping potential gradient, trapped by the trapping potential applied to the end-plate and cooled in the radial plane by a RF-field and are finally released out of the trap by lowering the trapping potential.

are subsequently stopped by a trapping potential (~ 50 V), as can be seen in Fig. 3.2. The ions are then accumulated for a set period of time depending on each experiment. Care needs to be taken as not to accumulate the ions for too long, as there are significant space-charge effects which will reduce the quality of the ion bunching already when there are more than 10^6 ions in the trap [13]. Lowering the trapping potential releases the ion bunch which is then extracted via the ISCOOL extraction electrodes, accelerated to $30 - 60$ keV and sent through the central beam line towards the different experimental setups. If bunching is not required, ISCOOL can also run in "continuous mode" in which case the ion beam will not be bunched upon leaving the trap.

3.2 Basics of laser spectroscopy

3.2.1 Photon absorption

The basic principle behind laser spectroscopy in general, is the resonant excitation of an atomic electron due to the absorption of a laser photon. The probability that a laser photon of frequency ω exciting an atomic transition of frequency ω_0 will be absorbed is given by [88]

$$\sigma(\omega) = \frac{g_2}{g_1} \times \frac{\pi^2 c^2}{\omega_0^2} A_{21} g_{\mathrm{H}}(\omega) \tag{3.1}$$

where g_2, g_1 are the degeneracy factors of the atomic states involved in the transition, $c = 299\,792\,458\ \frac{\mathrm{m}}{\mathrm{s}}$ is the speed of light in vacuum, A_{21} is the Einstein coefficient for spontaneous emission and the factor g_{H} shows how the absorption cross section has a Lorentzian dependence on the photon frequency via

$$g_{\mathrm{H}}(\omega) = \frac{1}{2\pi} \frac{\Gamma}{(\omega - \omega_0)^2 + \Gamma^2/4}, \tag{3.2}$$

where Γ is the transition linewidth.

3.2.2 Transition linewidth

An important consideration when working with high-resolution laser spectroscopy is the natural linewidth of the studied atomic transition. Due to Heisenberg's uncertainty principle, the uncertainty on the transition energy ΔE is related to the lifetime τ of the spontaneous decay from the upper to the lower state involved in the transition, by the relation $\Delta E \cdot \tau \approx \hbar$. The natural linewidth of the transition or full width at half-maximum (FWHM) Γ can then be defined by

$$\Gamma = \frac{\Delta E}{h} = \frac{1}{2\pi\tau} = \frac{\Gamma_0}{2\pi}, \tag{3.3}$$

where Γ_0 is the total decay rate of the atomic state defined as $\Gamma_0 = \frac{1}{\tau}$ with τ the mean lifetime of the state. For the $7s\ ^2S_{1/2}$ to $8p\ ^2P_{3/2}$ atomic transition in francium with a mean lifetime of $\tau = 83.5 \pm 1.5$ ns [89], this translates to a natural linewidth of $\Delta\nu = 1.91(3)$ MHz.

3.2.3 Power broadening

The resonant interaction of the laser photons with the atom will either cause the atom in the ground state to absorb a photon, thus exciting the atom or it will cause an already excited atom to decay back to the ground state via stimulated emission. The stimulated emission process changes the lifetime of the excited atomic state and therefore introduces a broadening in the transition linewidth. This linewidth can be estimated from the formula for the absorption coefficient $\kappa(\omega, I)$ [88]:

$$\kappa(\omega, I) = N\sigma_0 \frac{\Gamma^2/4}{(\omega - \omega_0)^2 + \frac{1}{4}\Gamma^2(1 + I/I_{\text{sat}})}, \tag{3.4}$$

where N is the total number of electrons in the atomic ground and excited states, σ_0 the absorption cross-section on resonance when $\omega = \omega_0$, ω_0 the angular frequency of resonant photons and I_{sat} is the saturation laser intensity, where the rate of photon absorption equals the rate of stimulated emission on resonance. Equation 3.4 describes the absorption coefficient with a Lorenzian distribution with a full width at half-maximum of

$$\Gamma_{\text{P}} = \Gamma\sqrt{1 + \frac{I}{I_{\text{sat}}}}. \tag{3.5}$$

Here the linewidth is labeled as Γ_{P} indicating that it originates from power broadening. From Eq. 3.5 it is clear that Γ_{P} will increase with respect to the natural linewidth Γ as the intensity of the laser light increases relative to the saturation intensity I_{sat}. The saturation intensity on resonance can be estimated from [88]

$$I_{\text{sat}} = \frac{\pi}{3}\frac{hc}{\lambda^3\tau}. \tag{3.6}$$

The power broadening effect can in general range from a few MHz to a few GHz. For the $7s\ ^2S_{1/2}$ to $8p\ ^2P_{3/2}$ atomic transition studied in francium, the lifetime of the transition is relatively long, which means that Γ in Eq. 3.5 will be small. Thus even if the laser intensity is larger than the saturation intensity, the total power broadening effect will still be small due to Γ.

3.3 Experimental considerations for studying francium

3.3.1 Ionization scheme

In order to plan an experiment to study the nuclear properties of the rare francium isotopes, an appropriate ionization scheme needs to be selected. In a typical ionization scheme for performing Collinear Resonance Ionization Spectroscopy, there need to be at least two laser systems: an excitation laser and ionization laser. The excitation laser is the one that probes the atomic hyperfine structure providing information about the nuclear properties as described in Chapter 2. The laser is set at a frequency corresponding to the transition frequency between the atomic ground state and an excited state. The atoms interacting with the laser light will get excited and if the ionizing laser pulse is fired before these atoms de-excite down to the ground state, the atoms will gain enough energy for one of their electrons to cross the ionization potential, ionizing the atom. The hyperfine structure is then studied by changing the laser frequency of the excitation laser step and counting the number of ions produced, with the largest number of ions being produced on the resonance frequency for a given (hyper)fine transition.

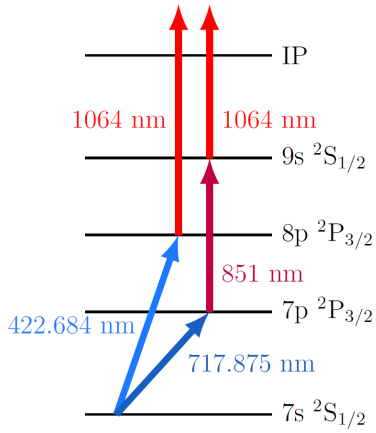

Figure 3.3: Two possible francium ionization schemes. The scheme that utilizes the $7s\ ^2S_{1/2}$ to $8p\ ^2P_{3/2}$ 422.684 nm transition was used in the experiments of this PhD work. The energy level spacings are not to scale.

Figure 3.3 shows the two ionization schemes of francium that were considered for the IS471 experiment [90, 91]. The first possible scheme would use a

422.684 nm first laser step to excite the atom from the ground $7s\ ^2S_{1/2}$ state to the excited $8p\ ^2P_{3/2}$ state. The ionizing step would then be a 1064 nm laser exciting the atomic electron from the $8p\ ^2P_{3/2}$ state into the continuum. The second possible scheme would excite the atom with a 717.875 nm laser step from the ground state into the $7p\ ^2P_{3/2}$ excited state. The hyperfine splitting of this state is about 3 times larger than that of the $8p\ ^2P_{3/2}$ state, but in this ionization scheme a second excitation step using a 851 nm laser would be needed to excite the electron to the $9s\ ^2S_{1/2}$ state. Only then could the atom be ionized via interaction with a 1064 nm laser step. Since this scheme required three laser steps which were not available experimentally, the two-step scheme using the $7s\ ^2S_{1/2}$ to $8p\ ^2P_{3/2}$ atomic transition as the excitation step was used. It can be additionally noted that in the original IS471 experimental proposal [90], another two-step scheme was considered starting from the $7s\ ^2S_{1/2}$ to $7p\ ^2P_{3/2}$ excitation step, but employing a 355 nm laser as the ionization step. This scheme was finally not used due to the higher probability of two-photon ionization that could occur due to the higher photon energy of the 355 nm photons, which would add to the potential non-resonant experimental background.

Table 3.1: Production yields for the francium isotopes studied during this PhD work. The yields denoted with *a* were taken from Lynch *et al.,* [3], while the rest of the yields are from the ISOLDE yield database [19]. The yields from the database are based on the production rate using the 600 MeV protons from the Synchrocyclotron. The yields from using the 1.4 GeV protons from the Proton Synchrotron Booster with a UC_x target are expected to be equally large or larger than the yields reported here.

Isotope	Yield	Target	Ionization
^{202}Fr	1×10^2 [92]	UC_x	Surface
^{203}Fr	1×10^3 [a]	UC_x	Surface
^{204}Fr	1×10^4 [a]	UC_x	Surface
^{205}Fr	2×10^5 [a]	UC_x	Surface
^{206}Fr	3×10^6 [a]	UC_x	Surface
^{207}Fr	3.6×10^6	UC_x	Surface
^{211}Fr	1.5×10^8	UC_x	Surface
^{214}Fr	9.4×10^2	UC_x	Surface
^{218}Fr	4.3×10^3	UC_x	Surface
^{219}Fr	8.9×10^3	UC_x	Surface
^{220}Fr	3.8×10^7	UC_x	Surface
^{221}Fr	8.9×10^8	UC_x	Surface
^{229}Fr	3.8×10^4	UC_x	Surface

[a] Taken from [3]

3.3.2 Production yields

An important step in determining which isotopes can potentially be studied experimentally is their production yield. The further the isotopes are from the stability line and/or the shorter their lifetime, the lower their production yields will be. As mentioned in Chapter 1, the yields typically necessary for performing collinear fluorescence spectroscopy are on the order of 10^4 atoms/s (and before ISCOOL was available it was even 10^6 atoms/s). In-source resonance ionization spectroscopy can perform measurements on yields down to a few particles per second, but it is limited in terms of resolving the hyperfine structure when it is smaller than 1 GHz. Also, this technique cannot be applied on francium isotopes, because of the high surface-ionization efficiency of alkaline elements.

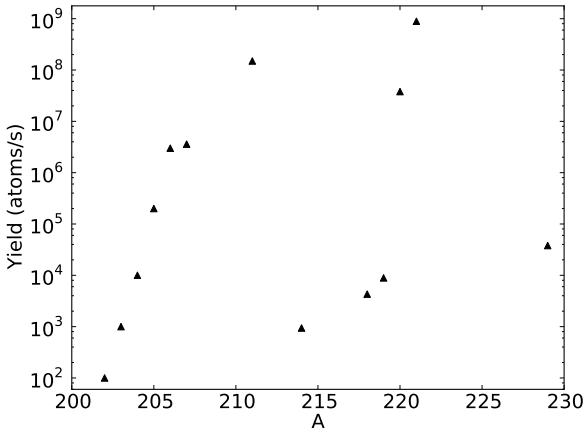

Figure 3.4: Graphical representation of the yields given in Table 3.1. The y-axis is given in a logarithmic scale.

After a succesfull commissioning experiment in august 2012, the CRIS technique has demonstrated the capability of measuring the hyperfine structure of isotopes produced at a rate as low as 100 atoms/s in October 2012 [2]. This allowed studies to be performed on a wide range of francium isotopes and isomers: ^{202g,m,203,204g,m1,m2,205,206g,m1,m2}Fr (where g denotes the ground state and $m, m1, m2$ isomeric states), which were the topic of the PhD thesis of Kara Lynch [4] and ^{218m,219,229,231}Fr which are the topic of this PhD work. The yields for these francium isotopes are given in Table 3.1 and Fig. 3.4 and they are taken from the ISOLDE database [19] for a UC_x target and from our own experiment as reported by Lynch *et al.* [3]. The yields in the ISOLDE database represent the production rate from the collisions of the protons from

the now decommissioned CERN Synchrocyclotron [93] with the UC_x target. Since the Synchrocyclotron accelerated protons to an energy of 600 MeV, the current yields for these isotopes can be expected to be larger than those from the ISOLDE database as we now use the 1.4 GeV protons from the Proton Synchrotron Booster.

3.4 Experimental setup

The experimental results which will be presented in Chapter 4, were obtained during two experimental campaigns. The first campaign took place in 2012 during which the hyperfine structure of the francium isotopes $^{202-206,218m,219,229,231}$Fr was measured for the first time with laser spectroscopy, but with a limited resolution of the optical peaks. After a two year offline period due to the shut down of the CERN accelerators and thus also the ISOLDE facility, a second experiment was performed in 2014 using a more narrowband laser system which enabled high-resolution hyperfine structure measurements to be performed for the first time for the isotopes ^{206,219}Fr. In the following sections, the experimental setup will be explained separately for the two different configurations, namely low-resolution from 2012 and high-resolution from 2014.

3.4.1 Low-resolution laser system

The layout for the laser system used in the 2012 experimental campaign is given in Fig. 3.5. The laser used for exciting the $7s\ ^2S_{1/2}$ to $8p\ ^2P_{3/2}$ atomic transition was the RILIS Ti:Sa laser [94]. Titanium-doped sapphire (Ti:Sa) lasers are solid state lasers in which a sapphire crystal serving as the gain medium is doped with Ti^{3+} ions which have a very large gain bandwidth. The gain medium is the material through which stimulated emission of light can develop by multiple passage of light, while the gain bandwidth is the range of frequencies for which the properties of the medium will allow for stimulated emission to occur. Sapphire is used as the gain medium due to its good thermal properties, which allow for the generation of high laser powers without introducing damage to the medium. As a consequence of the large gain bandwidth of the Ti^{3+} ions, the Ti:Sa lasers can generate wavelengths in a wide range: from ≈ 650 nm to 1100 nm.

In order to obtain the conditions necessary for stimulated emission of light to occur in the Ti:Sa gain medium, a pump laser is necessary. In the RILIS system the pumping laser was a DM60-532 frequency doubled Nd:YAG laser with a nominal output power of 60 W at a repetition rate of 10 kHz [94]. This laser is labeled as "Pump" in Fig. 3.5. In this type of laser, the doping material are neodymium ions (Nd^{3+}) and the gain medium is an yttrium aluminum garnet crystal ($Y_3Al_5O_{12}$). Nd:YAG lasers generally produce light with a 1064 nm wavelength. After frequency doubling to 532 nm, the light from this laser pumps the Ti:Sa crystal in the resonator cavity creating a population inversion between the ground and excited atomic states in the medium. The de-excitation of the excited states generates photons which trigger further excitations with the

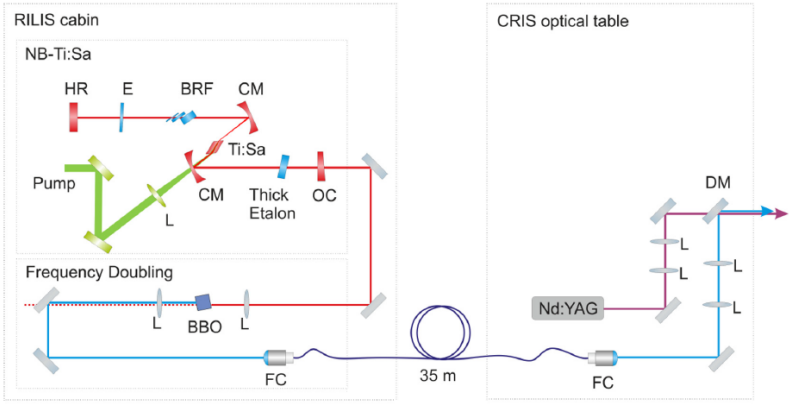

Figure 3.5: The laser system used in the 2012 experimental campaign. The RILIS cabin is shown containing the laser table on which the excitation step Ti:Sa laser and the pumping Nd:YAG laser (labeled "Pump") were mounted. The figure also shows the 35 m optical fiber cable and the CRIS optical table. The optical elements shown in the figure are: HR - high-reflection mirror, E - thin etalon, BRF - birefringent filter, CM - convex mirror, L - lens, OC - output coupler, BBO - frequency doubling crystal, FC - fiber couple, DM deflection mirror.

emitted photons passing repeatedly through the medium due to reflections from the convex mirrors (CM in Fig. 3.5), generating stimulated emission of light. By optimizing the positions of the thick etalon and birefringent filter (BRF) the desired wavelength can be separated out. In order to reach the 422.7 nm wavelength necessary for exciting the $7s\ ^2S_{1/2}$ to $8p\ ^2P_{3/2}$ atomic transition in francium, the etalon position was chosen so that the output of the Ti:Sa laser was 845.4 nm light. This served as the fundamental light which was then frequency doubled using a Beta Barium Borate crystal (BBO in Fig. 3.5), providing the 422.7 nm light. BBO is a birefringent crystal meaning that the refraction direction of light depends on its polarization and direction of propagation along the crystal. Such nonlinear optics materials are used for frequency doubling via second harmonic generation of the fundamental laser light. Second harmonic generation is a process in which nonlinear electromagnetic oscillations of the crystal medium, originating from the passage of the high intensity fundamental wave, generate an electromagnetic wave in the same phase and direction as the fundamental but with doubled frequency. For more information on this process and laser optics in general, the reader is referred to the literature [95, 88, 96].

The output 422.7 nm light from the BBO crystal was subsequently sent through a 35 m long optical fiber cable from the RILIS cabin to the CRIS experimental setup. Here the fiber was mounted in the laser cabin and sent into the CRIS beamline, which will be described in detail in Sect. 3.4.3. This light was overlapped with 1064 nm light coming from the 30 Hz CRIS Nd:YAG laser (Model: Quanta-Ray LAB 130). The 1064 nm laser light was used to excite the francium atoms from the $8p\ ^2P_{3/2}$ state into the continuum. In order to irradiate the francium atomic bunch at the same time, the CRIS 30 Hz Nd:YAG and the RILIS 10 kHz Ti:Sa system had to be synchronized. This was done by using the RILIS Ti:Sa laser firing signal as the master clock for the rest of the experimental triggers. The whole synchronization process of the CRIS beamline and laser system will be explained in more detail in Sect. 3.4.5.

As for the synchronization of the CRIS Nd:YAG, it was done by delaying the firing of the flash lamp with respect to the RILIS laser firing signal. In this laser system, the flash lamp serves to induce population inversion in the laser gain medium. At a fixed 190 μs after the flash lamp, the laser Q-switch is activated. Q-switching is used to generate narrow laser pulses of high intensity. This is done by keeping the energy losses inside the resonator cavity large (low Q-factor) until a desired moment in which the losses are drastically reduced (high Q-factor) leading to a fast build up of energy and the release of a short high power laser pulse. This is most often achieved by using a Pockels cell in combination with a light polarizer. The Pockels cell rotates the polarization of light if an electric field is applied to it, while leaving the polarization unchanged in the absence of an electric field. Using a polarizer to only pass light of a specific polarization through the resonator cavity by making the optical losses large for the wrong polarization, the system can be arranged as to only let the light pass through when the Pockels cell is switched on. This leads to the generation of short laser pulses, which were 20 ns wide in the case of the CRIS Nd:YAG laser.

3.4.2 High-resolution laser system

The experimental work on francium was continued in the 2014 campaign, during which a new laser system was used. There were two laser systems allowing for two modes of operation: 1) low-resolution using the RILIS laser system as in 2012 and 2) high-resolution using the new system. The difference between the two modes stemmed from the laser used for the 422.7 nm excitation step, as both used the newly acquired LPY-50-100 PIV Litron YAG laser for the 1064 nm ionizing step. This new Nd:YAG laser system possesses two laser heads which can individually operate at 100 Hz repetition rate. By adequately adjusting the offset between their firing, a frequency of 200 Hz could be achieved for the

ionization step, which lead to a factor of 6.67 improvement in the ionization efficiency as compared to the 30 Hz ionization step laser used in the 2012 experimental campaign.

The laser system used for the excitation step in the high-resolution regime was a Matisse TS continuous wave Ti:Sa laser. This laser system has a spectral linewidth of < 60kHz, allowing the upper state $8p\ ^2P_{3/2}$ hyperfine splitting to be resolved, as will be seen from the experimental results. While the use of a continuous laser system helped improve the experimental resolution, a drawback of using continuous laser light is the loss of statistics due to optical pumping. If the atomic beam continuously interacted with the excitation laser step during several lifetimes of the excited atomic state, spontaneous emission would cause the atoms to potentially de-excite to a state other than the currently probed hyperfine level of the ground state. These atoms would not be re-excited by the laser light since they would start from a different ground state hyperfine level and thus require a different excitation frequency. This would result in a much lower population of atoms in the excited state and thus less ions produced after interaction with the 1064 nm ionizing laser step. In order to avoid such losses in efficiency, the laser light of the continuous wave Matisse TS laser was chopped using a Pockels cell. This resulted in an efficiency for RIS that is similar to that obtained using the broad-band pulsed RILIS laser. The procedure by which this was done is outlined in detail in Article II, Appendix A.

3.4.3 CRIS beamline

After the radioactive ion beam of interest has been produced by impinging the 1.4 GeV protons on the ISOLDE target, mass separated using the HRS and finally bunched using ISCOOL, the bunched radioactive ion beam is sent to the CRIS beamline, illustrated in Fig. 3.6. For offline measurements, instead of the radioactive beam coming from ISOLDE, a stable ion beam can be used from the CRIS offline ion source. A new design of this ion source was developed as part of this PhD work, which will be discussed extensively in Sect. 3.5.

Whichever ion beam is used, it is sent via a 34° bend into the straight section of the CRIS beamline. At this point the beam enters the charge exchange cell (CEC). The main section of the CEC consists of a large cylindrical housing unit which houses a 10 mm in diameter central metal pipe, which is filled with potassium. The cylindrical housing is heated by heating cables which heat up the central part of the metal pipe until the potassium is vaporized. The potassium vapor diffuses out towards the outer edges of the metal pipe, which are cooled by oil circulation. This results in a circulation of the potassium vapor from the central part of the tube towards the colder edges where it condenses

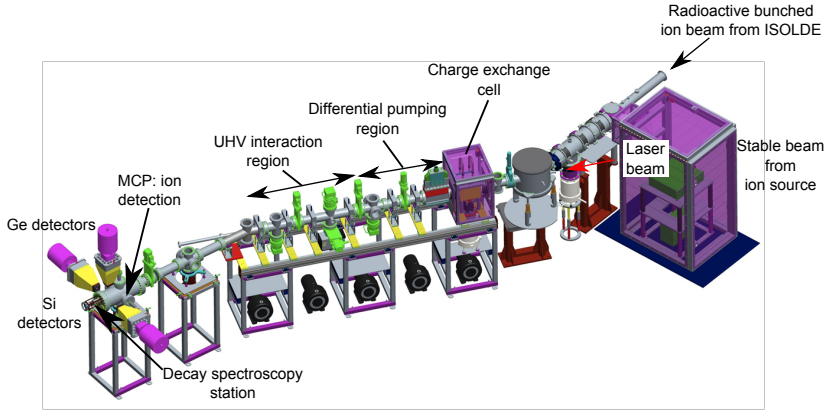

Figure 3.6: A 3D drawing of the CRIS beamline at ISOLDE, CERN. The different sections and their functions are explained in the text.

and moves back to the central section. The hot potassium vapor interacts with the radioactive ion beam neutralizing it via collisional charge exchange. In the case of francium the reaction can be written as

$$\mathrm{Fr}^{+} + \mathrm{K} \rightarrow \mathrm{Fr} + \mathrm{K}^{+} - \Delta E, \tag{3.7}$$

where Fr^{+} represents the francium ions in the beam and K the neutral potassium atoms in the vapor and ΔE is the transfer of energy in the reaction which is less than 1 eV in the case of resonant charge exchange to the ground state of francium. The charge exchange cell is usually operated at 150°C, with an estimated neutralization efficiency of 50%. The ions that are not neutralized while passing through the CEC are deflected out of the beam path by a deflection plate just after the CEC to which a positive voltage is applied.

Within the region of the charge exchange cell the pressure can rise up to values of 1×10^{-6} mbar due to the potassium vapor. Since the main source of background in resonant laser ionization are ions resulting from non-resonant collisional ionization, it was necessary to install a differential pumping region between the charge exchange cell and the ultra-high vacuum (UHV) interaction region. The differential pumping section allows for a pressure differential of $\sim 10^{-3}$ mbar between the two sections, enabling the pressure in the interaction region to reach values below 10^{-9} mbar.

At the time the neutralized atom beam reaches the UHV interaction region, it is overlapped in time and space with the excitation and ionization laser beams

coming from the CRIS laser table. The procedure for synchronizing the ion arrival time in the UHV section with the laser firing will be discussed in more detail in Sect. 3.4.5. Once the atoms are resonantly ionized via interaction with the two laser pulses, they continue along their path and are deflected towards the detection region. Any atoms that have not been ionized will continue straight into a beam dump. This is one of the strengths of this method: it allows to select ultra-pure beams of one particular isotope or isomer, as discussed by Lynch *et al.* [3].

In the detection region, the ions can either be sent to a two-stage Hamamatsu F4655-12 micro channel plate (MCP) where they are counted as a function of laser frequency, or they can be sent to the decay spectroscopy station (DSS) [97, 98, 3] where their radioactive decay products are detected after implantation in a thin carbon foil. The DSS will be discussed in more detail in the following section, and has been described in Rajabali *et al.*[98]. In the case of ion detection, the ion beam is focused and sent onto a copper dynode plate, which is biased with a negative voltage. The ions impinging on the plate will produce secondary electrons which will be deflected by the negative voltage onto the MCP. The MCP has two plates which are supplied with an increasingly positive voltage in order to attract the secondary electrons from the dynode and guide them onto the MCP anode where they are detected as a drop in voltage. The total MCP system is usually biased with a voltage of 2100 V which is divided across the individual plates.

3.4.4 Decay spectroscopy station

Instead of being sent to the MCP, the ion beam can sometimes be sent to the decay spectroscopy station (DSS), which is based on the KU Leuven "windmill" design [99, 100]. In order to be compatible with the UHV in the preceding section of the CRIS beamline, the cables and detectors used in the DSS are UHV compatible [98]. The DSS consists of a rotating wheel which houses 8 carbon foils and one Faraday cup. The carbon foils have a thickness of 20(1) μg/cm^2 and are used for the implantation of radioactive ions. The carbon foil thickness is such that decay products such as α-particles and fission fragments can leave the foil. The Faraday cup is a metal plate which is 0.5 mm thick and 10 mm in diameter and which is used to determine the amount of beam that falls on it. It is used for verifying and optimizing the transmission through the beam line. The impinging ion beam kicks of electrons from the plate generating a measurable current which is proportional to the number of ions in the beam.

In order to detect the α-particles emitted by the nuclear decay of the implanted activity, two Canberra Passivated Implanted Planar Silicon (PIPS) detectors, which are used for the detection of charged particles such as α-particles

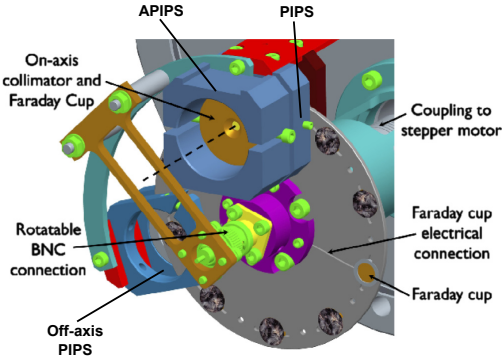

Figure 3.7: Drawing of the DSS showing the rotating wheel, Faraday cup, clamps for the PIPS detectors, the coupling to the stepper motor and rotatable BNC connection. Image taken from [1].

and β-decay electrons, are placed around the carbon foils. One detector is placed directly behind the foil and the other detector is an annular PIPS(APIS) detector which has a 4 mm aperture for allowing the beam to pass through it. The detector location relative to the wheel can be seen in Fig. 3.7. The APIPS detector is protected by a metal plate that blocks the beam from directly falling on the detector. This plate can also be used as a Faraday cup by connecting it to an ampere-meter. A stepper motor (Model: 17HS-240E, 2.3 A/phase) is used to step-wise rotate the wheel allowing for different carbon foils to be implanted or for the Faraday cup on the wheel to be placed in the position of the beam path. In order to measure the radioactive decay rate over time and hence the lifetime of a particular isotope or isomer, the implanted carbon foil can be moved out of the beam path and placed in front of the off-axis PIPS detectors.

In order to detect the γ-rays originating from the radioactive decay of the implanted radiation, up to three High Purity Germanium detectors (HPGe) can be placed around the detection chamber. During the 2012 experimental campaign, two such detectors were used: a 70 % HPGe detector (Model: GC7020) and an E $-$ ΔE germanium detector (Model: GR3019/GL1512 telescope). Unfortunately, after analyzing the measured γ-spectrum after the experiment, it was found that the thickness of the detection chamber walls was too thick, resulting in very poor quality spectra. With this in mind a design for a new DSS chamber has been made [4], which will be implemented after it has been sufficiently tested offline. For more details on the characteristics of the PIPS and HPGe detectors and the DSS in general, the reader is referred the article of Lynch *et al.* [3] and the PhD thesis of Kara M. Lynch [4].

3.4.5 Equipment synchronization

A very important aspect of the experimental setup at CRIS is the synchronization of the firing of the lasers with ion arrival in the interaction region, along with the synchronization of the received signals with the data acquisition system (DAQ). This section will describe the two different synchronization schemes used in the low-resolution experimental campaign of 2012 and in the high-resolution campaign in 2014.

Low-resolution experimental campaign 2012

The synchronization scheme used during the experimental campaign of 2012 is illustrated in Fig. 3.8. The main trigger that served as the master clock for all subsequent triggers and signals was the signal from the RILIS 10 kHz pumping Nd:YAG laser (line (a) in Fig. 3.8). This was done using a Quantum Composers 8 channel pulse generator (Model: QC9258). Since the maximal firing rate of the CRIS Nd:YAG laser was 33 Hz, it was necessary to find a way of synchronizing its firing with that of the RILIS pump laser. This was done by modifying the rate of firing to 31.25 Hz, so that 1 pulse of the CRIS Nd:YAG laser would fire for every 320 pulses of the RILIS laser, with the result that the two systems would remain in synchronization.

The flash lamp of the CRIS Nd:YAG laser b) is the first to receive the signal delayed by 85.21 μs from the RILIS signal. The flash lamp creates the population inversion conditions in the gain medium of the laser cavity and 190 μs after this the Q-switch of the laser c) is triggered which enables the conditions for lasing. Delayed by 80.15 μs after the flash lamp trigger is the ISCOOL release trigger d). The delay for this trigger is introduced in order to have the ion bunch arriving in the interaction region section of the CRIS beamline at the moment that the Nd:YAG laser is ready to fire. This delay had to be changed by $\sim 1-2$ μs for every isotope, due to the difference in time of flight because of the different nuclear mass.

After the beam is ionized in the interaction region, it takes 11 μs for it to reach the MCP. In order for the MCP signals to be recorded only during the expected ion arrival time, a trigger signal delayed by 100 μs after the ISCOOL release, with a window of 10 μs, was sent to a LeCroy oscilloscope e) (Model: WavePro 725Zi 2 GHz bandwidth, 12 bit ADC, 20 GS/s). The narrow measurement window was used in order to minimize the number of background dark counts originating from the MCP. The MCP dark count rate is on the order of 1 count/s, which translates to 3×10^{-4}count/s, for a 10 μs window opened every 32 ms [1]. The total number of ion counts during a bunch

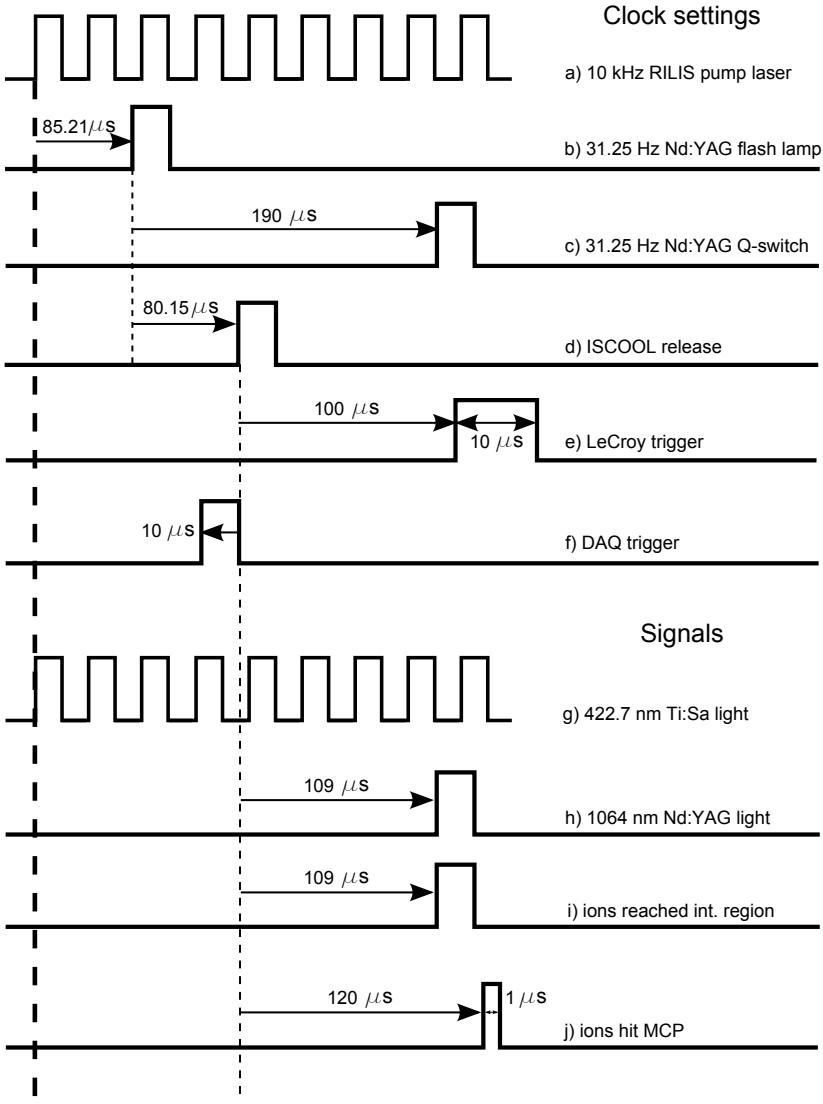

Figure 3.8: A schematic overview of the different triggers and signals used during the CRIS 2012 experimental campaign. The triggers sent to the different devices using the Quantum Composers were: a) the master trigger that triggered the quantum composers unit, b) the flash lamp signal for the CRIS Nd:YAG laser, c) internally delayed CRIS Nd:YAG Q-switch, d) signal lowering the ISCOOL trapping potential, e) trigger for the LeCroy acquisition window, f) trigger for the data acquisition. Timing of the most relevant signals: g) RILIS Ti:Sa light, h) firing of the CRIS Nd:YAG laser, i) the ions reach the interaction region, j) the 1μs wide ion bunch is detected by the MCP.

recorded by the LeCroy oscilloscope was saved by the data acquisition system f), which was triggered just before the ISCOOL release signal in order to give the computer sufficient time to save the data before the arrival of the next bunch.

The bottom part of Fig. 3.8 shows the signal arrival times of the laser light (g,h) in the interaction region and the ion arrival time on the MCP j). The total ion time of flight from ISCOOL to the MCP was 120 μs on average. The laser firing signals were measured with a photo diode, which was important in order to monitor and correct the small systematic shifts that occurred between the two pulses due to the non-negligible inherent jitter in the RILIS and CRIS Nd:YAG laser systems.

High-resolution experimental campaign 2014

During the experimental campaign of 2014 the equipment synchronization was updated in order to incorporate the new laser systems, namely the twin headed 100 Hz Litron Nd:YAG laser and the Matisse TS continuous wave (CW) Ti:Sa laser. The synchronization system described in this section could operate either in the low-resolution regime by using the RILIS pulsed Ti:Sa laser for the excitation step, or Ti:Sa laser system. This capability provided several benefits: 1) by first scanning a broader frequency range using the low-resolution system, the locations of the hyperfine structure peaks could be found and subsequently used for scanning with the high-resolution system; 2) by scanning across the same structure with both laser systems with all other experimental conditions being the same, the total experimental efficiency between the two regimes could be compared; 3) with the high-resolution system previously unresolved hyperfine lines (e.g. from isomers in the beam or due to a small hyperfine splitting in one of the atomic states) could now all be resolved.

The synchronization logic is given in Fig. 3.9. Two Quantum Composers pulse generators were used: 1) on the laser table for controlling the firing of the CRIS Nd:YAG lasers and 2) on the DAQ table, for controlling the triggers for ISOLDE, DAQ, DSS and Pockels cell. As in the 2012 campaign, the RILIS 10 kHz pumping laser trigger was used as the master trigger (a). This trigger fired the flash lamps of both heads of the CRIS Litron Nd:YAG laser for 1 pulse out of 100 (b,d), in order to maintain the synchronization of this 100 Hz laser with the RILIS master trigger. After an internal delay of 100 μs, the Q-switches of these lasers fired (c,e). A copy of the flash lamp trigger (f) was used as the trigger for the DAQ table Quantum Composers unit.

Due to technical constraints, during the experimental run it was decided to delay the release of ISCOOL by 9.990 ms (g), in order for the release to effectively be -10μs before the firing of the CRIS Nd:YAG flash lamp. In

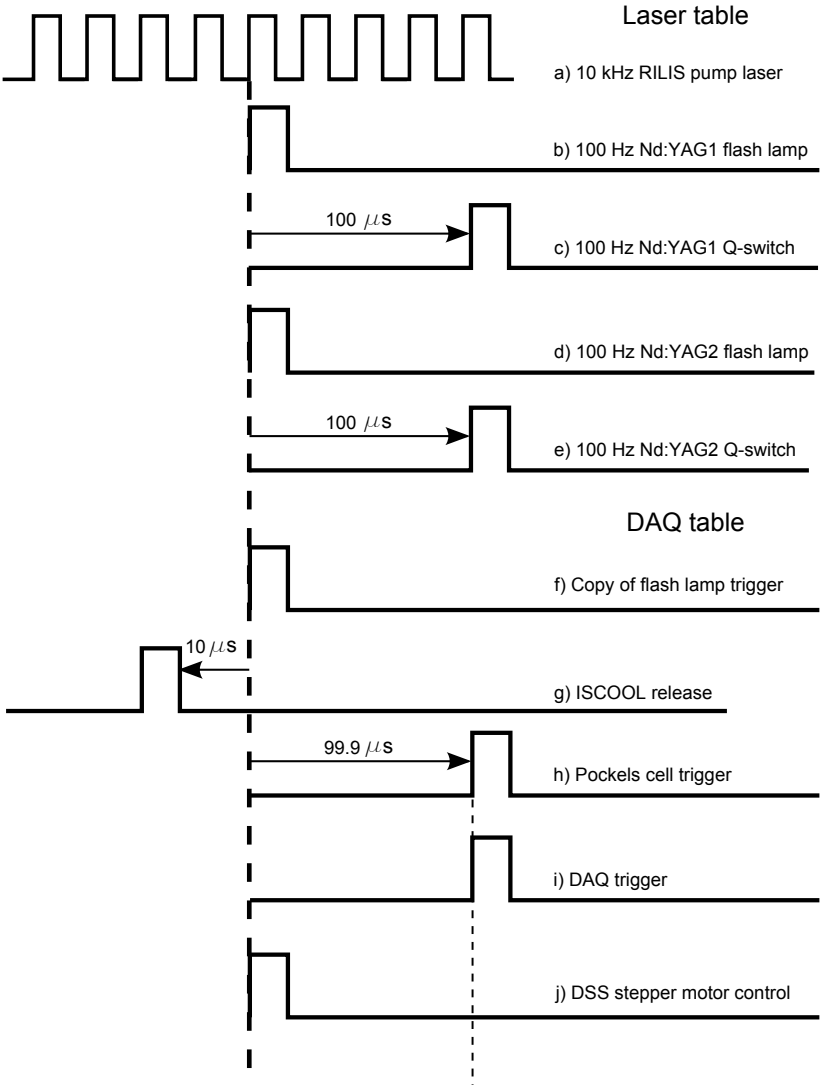

Figure 3.9: Synchronization logic for the 2014 experimental campaign. Laser table: a) 10 KHz master trigger from RILIS, b), d) flash lamp triggers for the CRIS Litron Nd:YAG laser heads, c), e) Q-switches for the Litron laser heads. DAQ table: f) copy of the Nd:YAG flash lamp trigger, g) ISCOOL release trigger, h) Pockels cell active trigger, i) data acquisition trigger and j) DSS motor stepper control trigger.

this way it was possible to have the ions arriving in the interaction region at the moment the Nd:YAG Q-switch fires. Triggered at 100 ns before the Nd:YAG Q-switch was the Pockels cell (h). This trigger was sent to a fast square wave pulser (Model: Behlke FSWP91-01), which could rapidly switch between applying a 0 V or 2.4 kV voltage to the Pockels cell. While the 2.4 kV were applied, the polarization of the CW Ti:Sa laser light was rotated by $\pi/2$. Since there was a polarizing beam splitter cube positioned after the Pockels cell, transmitting only light of a certain polarization, the combination with the Pockels cell meant that chopped pulses of CW Ti:Sa laser light could be created while 2.4 kV were applied to the Pockels cell. The pulse length was 100 ns and the optimal condition for firing the Nd:YAG pulse was on the falling edge of this signal. The optimization of the time delay/overlap between both laser pulses and the ion arrival in the interaction region is discussed in detail in Article II, Appendix A. At the same time, as the Pockels cell fires, a signal is sent to the data acquisition system for recording. This was a new system compared to the campaign in 2012 and will be explained in more detail in the next section. The final trigger in Fig. 3.9 was sent to the stepper motor of the DSS, in order to control the implantation and measuring sequences for the decay spectroscopy measurements.

3.4.6 Data acquisition

LabVIEW system

The data acquisition system used in the low-resolution experimental campaign of 2012 was made using the NI LabVIEW software package [101]. A screenshot of the DAQ user interface is given in Fig. 3.10, while a scheme depicting the data collection and saving process is shown in Fig. 3.11. As mentioned in the previous section, the main trigger from RILIS serves as the master clock for the whole trigger chain. The ISCOOL release trigger is set so that the neutralized atom bunch arrives in the interaction region at the moment the CRIS Nd:YAG laser fires. The produced ions reach the copper dynode and emit secondary electrons which are detected by the MCP as a drop in voltage. Only the MCP signals detected during the LeCroy measurement window are saved, as can be seen from Fig. 3.11.

The DAQ system communicated with the LeCroy oscilloscope via a National Instruments PXI data acquisition board (Model: NI PXI-6225), through a USB connection with the CRIS computer hosting the data acquisition system. At the time the data acquisition system saves the ion counts coming from the oscilloscope, the current wavenumber of the RILIS 422 nm laser and the current time, it also saves the current values of the various experimental parameters

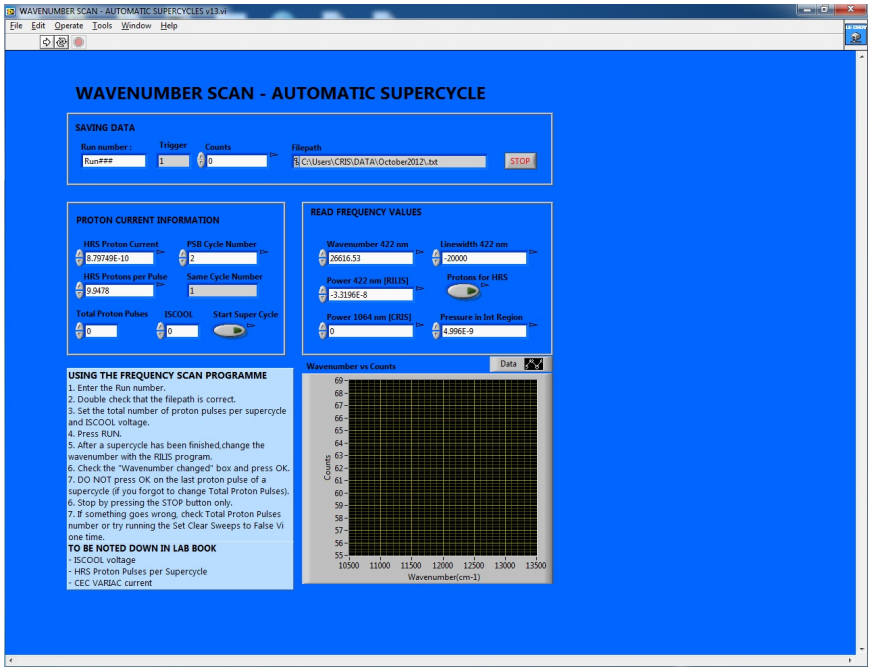

Figure 3.10: A screenshot of the graphical user interface for the data acquisition system used in 2012.

which are given by the RILIS LabVIEW shared variables and the CRIS shared variables. The shared variables published by RILIS were: 1) 422 nm laser power from the RILIS cabin, providing a relative power measurement to monitor any large changes in power during a particular scan; 2) HRS proton current giving the total current of protons impinging on the HRS target; 3) HRS protons per pulse, showing the total number of protons per proton pulse; 4) Protons for HRS, a boolean variable indicating if the current PSB proton pulse is sent to the HRS target; 5) the linewidth of the fundamental 844 nm RILIS laser light before frequency doubling to 422 nm. The shared variables from the CRIS side were: 1) pressure in the interaction region and 2) the power of the CRIS 1064 nm Nd:YAG laser pulses. All of these parameters were continually written to a buffer and finally saved to a .txt file at the DAQ trigger (f in Fig. 3.8 and DAQ trigger in Fig. 3.11). Since this trigger is set to occur before the ISCOOL release trigger, it gives the computer the most time to save the data from the previous ion bunch before starting to record the data from the new bunch. Each bunch is associated with a trigger number in the .txt file for straightforward identification.

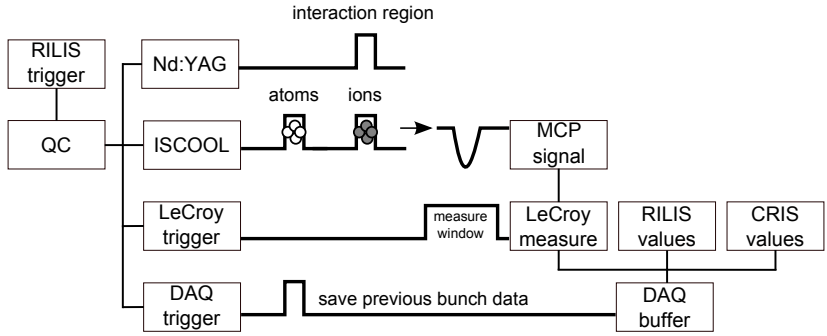

Figure 3.11: Schematic representation of the trigger timing and data saving process used in 2012. QC refers to the Quantum Composers pulse generator, ISCOOL refers to the signal for triggering the ISCOOL release, Nd:YAG refers to the flash lamp and Q-switch signals for the CRIS 1064 nm Nd:YAG laser and the RILIS values and CRIS values squares refer to the shared variables published by RILIS and CRIS, respectively.

The scanning of the 422 nm RILIS Ti:Sa laser was performed by using the RILIS Equipment Acquisition and Control Tool (REACT) [102]. This system also served to stabilize the laser frequency. The REACT tool could change the laser frequency by using a pair of motors which moved the inter-cavity thin and thick ethalons of the RILIS Ti:Sa laser to a different angle, thus allowing the specified frequency mode to exit the laser cavity. In order to synchronize the frequency change with the rest of the signals, the LabView DAQ could operate in three modes: 1) set time per frequency step, 2) one super cycle per frequency step, 3) set number of proton pulses per frequency step. In mode 1) the DAQ would continuously record data for a set amount of time specified by the user, upon which data recording would halt until the user changed the frequency with the REACT tool. The user would then instruct the DAQ to continue and the process would be repeated after a new time step has passed. Modes 2) and 3) operated on the same principle, with the step in mode 2) being a proton supercycle and in mode 3) the DAQ would keep recording for a specified number of pulses which had protons sent to the HRS. During the run mostly modes 1) and 2) were used to collect data.

Python system

During the 2014 experimental campaign a new data acquisition system based on Python was used. The transition from LabVIEW to Python was done in order to optimize the speed of the system, to avoid problems with updating the

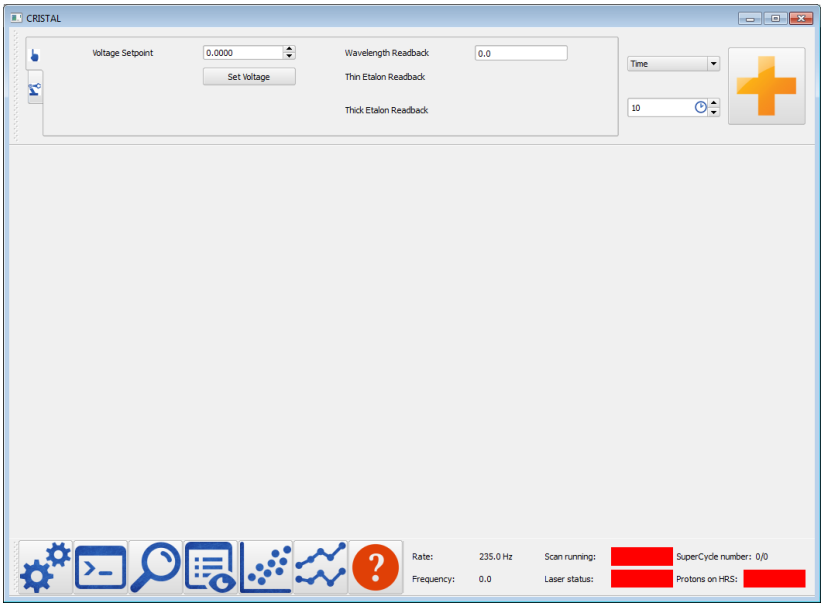

Figure 3.12: Screenshot of the python data acquisition system CRISTAL, developed by Ruben de Groote [14], which was used in the 2014 campaign. The name CRISTAL is an acronym for CRIS laser Tuning, Acquisition and Logbook. The top section of the window is used to set the laser scanning ranges. The middle part can be filled with different plots of the measured data. The bottom part is used to navigate between the different functionalities such as the logbook, raw data streams and help. Further details are given in the text.

LabVIEW software and having different versions across different computers, and to increase the overall stability of the system. The main hardware component of the new data acquisition system was a National Instruments USB DAQ card (Model: NI-6211).

The data acquisition system recorded the shared variables published by RILIS as the LabVIEW system from 2012, with additional parameters such as the ion rate per second (relevant for optimizations), the wavenumber of the CW Ti:Sa laser, and the status of the pulsed Ti:Sa laser. The system could also be used to directly control the frequency scanning of the pulsed Ti:Sa laser. The user interface for this system is shown in Fig. 3.12. The interface provides several widgets with different capabilities: general settings, python console, digital logbook, plotting the raw data from all monitored parameters and a help file.

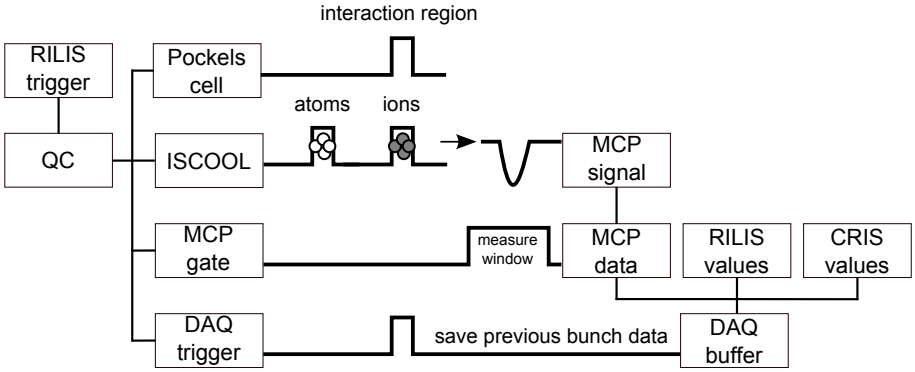

Figure 3.13: Schematic representation of the trigger timing and data saving process used in 2014. The Pockels cell is triggered at the time the neutralized atom bunch arrives in the interaction region. This allows the CW laser light to excite the atoms in the bunch, during a period of 100 ns. MCP signals are accepted only during a 10 μs time window, after the ion bunch arrived on the MCP. These coincidence signals are then sent to the data acquisition system and are saved along with the other recorded experimental parameters from RILIS and CRIS. The values are continually accumulated and appended to a text file at the start of the next Pockels cell trigger.

The data acquisition system could run in two general modes of operation: measurement with scanning the CW Ti:Sa laser for high-resolution measurements and scanning the RILIS pulsed Ti:Sa laser with the REACT software for low-resolution measurements. The scanning of the CW Ti:Sa laser was done by using the Matisse Commander software, which is the inherent control software of the CW Ti:Sa laser. This software would scan the wavelength of the laser over a certain range, while the data acquisition system would continuously record the wavelength.

The logic and timing used for saving the data was very similar to the system used in 2012. This is schematically shown in Fig. 3.13. The major difference was the addition of the Pockels cell, leading to the necessary gating of the MCP signal, which can be seen in the figure. The fast switching of the voltage supplied to the Pockels cell introduced a noise signal in the surrounding signal cables at each Pockels cell trigger. There was also noise present from the firing of the Litron Nd:YAG Q-switches. Since the raw MCP signal also had to be converted to a NIM pulse in order to be read by the DAQ card, these signals were first amplified and then discriminated before being sent through a coincidence unit to only correspond to signals in a 10 μs window around the arrival time of the ions on the MCP. This coincidence signal was then sent to the DAQ. The DAQ

card also collected the analog signals from the photo diodes for measuring the laser powers. At the start of every Pockels cell trigger, the data accumulated during the 10 ms from the previous trigger was saved, along with all of the rest of the monitored experimental parameters from RILIS and CRIS.

3.5 CRIS ion source development

For performing complex laser spectroscopy experiments such as with the CRIS beamline, it is important to have access to stable ion beams for optimizing the beam transport through the beamline, testing charge exchange efficiency, developing ionization schemes for elements to be studied during on-line experiments, optimizing the laser systems, and testing and optimizing the data acquisition system for ion detection. This section will describe the surface ionization process, the design process for the new CRIS ion source and show the most relevant results obtained using the new source.

3.5.1 Surface Ionization Ion Sources

Atoms interacting with the hot surface of a particular material can become positively or negatively ionized by either transferring one of their electrons to the surface material or receiving an electron from it, based on the difference of the work function ϕ of the material, the ionization energy E_I or electron affinity E_a of the atoms and the temperature of the surface. The ionization energy E_I is defined as the minimum energy required to remove an electron (to infinity) from an atom in its ground electronic state. The work function ϕ is the minimum energy needed to remove an electron from the surface of a solid material to a point immediately outside the solid surface. The electronic affinity E_a can be defined as the energy released by a neutral atom after gaining an extra electron to form a negatively charged ion. If the material has a high work function, such as: tungsten ($\phi = 4.53$ eV), rhenium (4.1 eV), iridium (5.4 eV) or zeolite, and the element to be ionized is an alkaline metal or alkaline earth metal, thus having a low ionization energy ($E_I \leq 5\,\text{eV}$), positive ions can be produced. Conversely, if a low work function material such as: tungsten with a Cs monolayer (1.36 eV), barium oxide BaO (1.5 eV) or lanthanum hexaboride LaB_6 (2.70 eV) is used with a halogen ($E_a \geq 1.8\,\text{eV}$), negative ions can be produced. The expression for the ionization efficiency ϵ_{ion} for positive ion production is based on the Langmuir-Saha equation [103] and is given by:

$$\epsilon_{ion} = \frac{n_i^+}{n_i^+ + n_0} = \left[1 + \frac{g_0}{g_i^+} e^{\frac{E_I - \phi}{\text{kT}}}\right]^{-1}. \tag{3.8}$$

Here n_i^+ is the number of positively charged ions, n_0 is the number of neutral atoms, T the surface temperature, and g_i^+, g_0 are the statistical weights of the ions and neutral atoms, being the sum of all $2J + 1$ for a given atomic configuration. For example, the ground state of gallium has an atomic

Table 3.2: Work function ϕ, ionization energy E_i, electron affinity E_a and statistical weights g_0/g_i^+ (taken from [20]), for the materials for which the ionization efficiency ϵ_{ion} was calculated using 3.8 and shown in Fig. 3.14. The ionization efficiencies in Fig. 3.14 were all calculated for the same $\phi = 5.25\,\text{eV}$, while the work function values in this table are given only for reference.

Material	ϕ [eV]	E_i [eV]	E_a [eV]	g_0/g_i^+
Cs	1.81	3.9	0.4	2/1
Rb	2.13	4.2	0.49	2/1
K	2.25	4.3	0.5	2/1
Na	2.28	5.1	0.55	2/1
Ba	2.11	5.2	-0.5	1/2
Li	2.46	5.4	0.6	2/1
La	3.3	5.6	0.5	10/21
Sr	2.74	5.7	-1	1/2
In	—	5.8	0.3	6/1
Ga	4.16	6.0	0.3	6/1
Ca	3.2	6.1	-1.5	1/2

configuration of $3d^{10}4s^24p$ which gives rise to doublet states $^2P_{1/2}$,$^2P_{3/2}$, with $J = 1/2$ and $J = 3/2$ respectively. The statistical weight g_0 of this ground state will then be $g_0 = 2 \cdot 1/2 + 1 + 2 \cdot 3/2 + 1 = 6$, as seen in Table 3.2.

Similarly to (3.8), an equivalent expression for the ionization efficiency for the production of negatively charged ions can be written as

$$\epsilon_{ion} = \frac{n_i^-}{n_i^- + n_0} = \left[1 + \frac{g_0}{g_i^-} e^{\frac{\phi - E_a}{\text{kT}}}\right]^{-1}, \tag{3.9}$$

where n_i^- is the number of negatively charged ions, g_i^- the statistical weight of the negatively charged ions.

To illustrate the dependence of ϵ_{ion} on the ionization energy of the materials needed to be ionized, Eq. 3.8 was used to calculate ϵ_{ion} for various materials from Table 3.2. In the calculation, a fictional material with work function $\phi = 5.25$ eV formed the ionizing surface and the ratio g_0/g_i^+ was taken from Table 3.2.

For the ion source developed as part of this PhD work, tantalum was used as the ionizing surface. Figure 3.15 shows the ionization efficiencies calculated for the materials in Table 3.2, using the work function of tantalum $\phi(\text{Ta}) = 4.25$ eV. It is clear from the two figures that the fictive material with a higher work

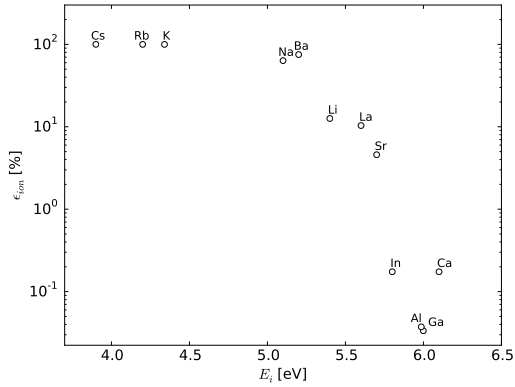

Figure 3.14: Ionization efficiency vs. ionization energy for a fictive material with work function $\phi = 5.25\,\text{eV}$, for the production of positive ions. The ionization efficiency ϵ_{ion} was calculated using Eq. 3.8.

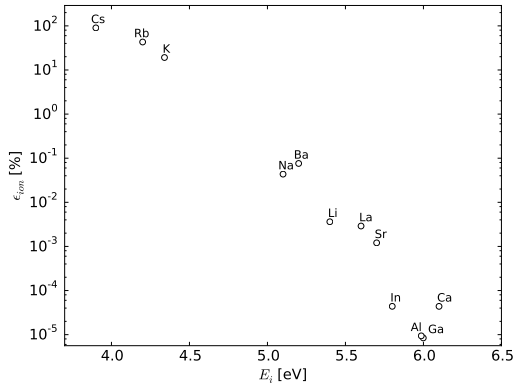

Figure 3.15: Ionization efficiency vs. ionization energy for tantalum which was used as the surface material in the CRIS ion source. Tantalum has a work function $\phi = 4.25\,\text{eV}$. The ionization efficiency for the production of positive ions ϵ_{ion} was calculated using Eq. 3.8.

function would be better suited for surface ionization, if such a material could be found and used as a container. However, tantalum still provides a satisfactory ionization efficiency for potassium which is $\epsilon_{\text{ion}} = 19.17\%$.

3.5.2 CRIS ion source design

Ion production

The ion source used for providing stable alkali ion beams to the CRIS setup is based on the surface ionization principle, which was described in the previous section. A schematic view of the source itself is given in Fig. 3.16. A container made of tantalum is used to house the source material, in this case KCl. Tantalum is used due to its very high melting point: 3290 K. This is important since a high heating current $I_H \sim 40$ A is fed via copper rods to the tantalum container. The heat generated by this current serves to break up the KCl and provide the conditions for surface ionization. The K and Cl atoms drift out of the container into a 1 mm diameter tantalum tube. Due to their low ionization energy $E_i(\mathrm{K}) = 4.34$ eV, the K atoms release one electron and become positively charged by colliding with the tantalum tube walls.

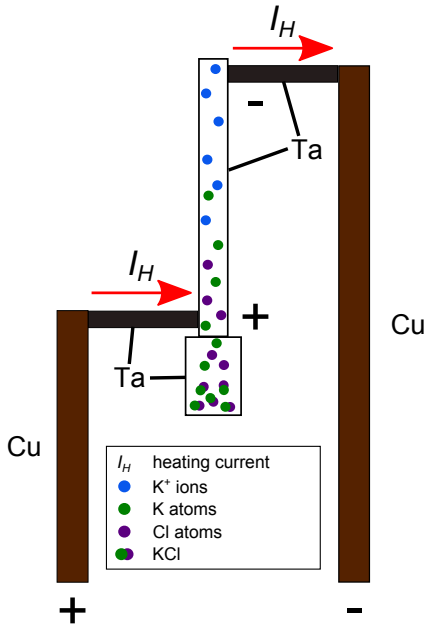

Figure 3.16: Schematic view of the CRIS ion source. The KCl salts break up in the source container and drift into the thin tantalum tube, inside of which K^+ ions are formed via surface ionization. More details can be found in the text.

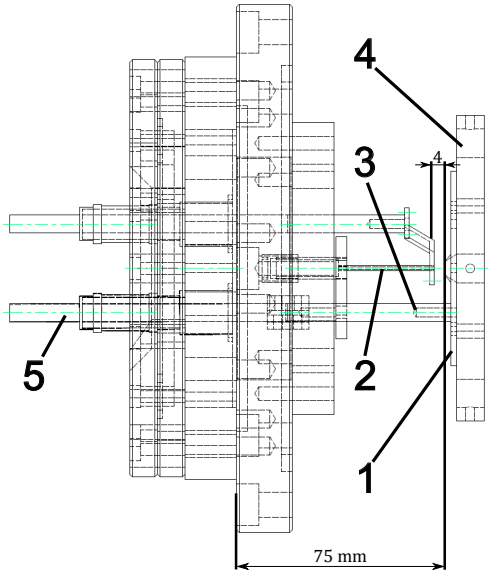

Figure 3.17: Cross-section of the extractor electrode mounted on the ion source flange: 1) extractor electrode, 2) ion source tantalum tube, 3) copper rod for supplying a negative voltage to the extractor electrode, 4) isolating TecaPEEK ring, 5) copper feedthrough. The ion source flange used to mount the source onto the rest of the ion source vacuum chamber was of type ISO-K 100.

After the ions are produced in the tantalum tube, they are accelerated towards the extractor electrode, which is held at a lower voltage than the ion source flange. In the new ion source design, the extractor electrode is mounted directly on the ion source flange in order to improve alignment with the source tube and to enable simple re-filling of the source, since this flange can be removed from the beamline without influencing the other beam optics elements. Figure 3.17 shows a technical drawing of a cross-section of the ion source flange, extractor electrode and mount.

In Fig. 3.17, the extractor electrode is labelled as 1, while the ion source tube is labeled as 2. The electrode is mounted onto a TecaPEEK piece (labelled 4) that isolates it from the stainless steel rods of the beam optics section and from the ion source flange. Voltage is supplied to the extractor electrode via a copper feedthrough (labelled 5), that is connected to a copper rod (labelled 3) with a copper clamp. This assembly can be directly mounted on the ion source vacuum chamber, given in the next section.

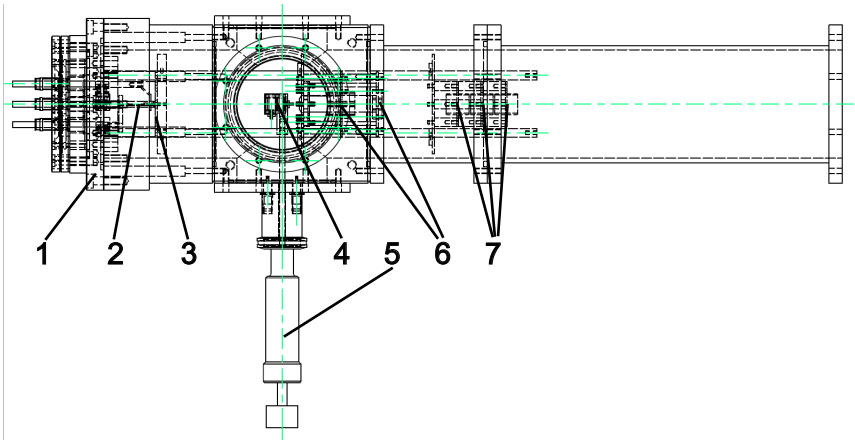

Figure 3.18: Side cross-section view of the ion source vacuum chamber assembly: 1) ion source flange, 2) tantalum tube, 3) extractor electrode, 4) Faraday cup, 5) linear motion feedthrough, 6) horizontal and vertical steering plates, 7) Einzel lenses.

Ion source vacuum chamber assembly

As part of the new ion source design, a new vacuum section was designed to house the ion source, beam optics and provide access to a dedicated turbo pump, as close as possible to the ion source. Having a dedicated turbo pump is particularly important when attempting to keep the ion source at a high voltage, such as the design goal of 30 kV. The previous ion source was at most operated at 3 kV. A technical drawing cross-section of the new ion source vacuum section is given in Fig. 3.18, while a 3D cross-section view is given in Fig. 3.19. The ion source mounting flange, tantalum tube and extractor electrode which were described in the previous section are labeled as 1, 2, 3 in the figures.

A Faraday cup (labeled as 4 in Figs. 3.18, 3.19) is placed after the extractor electrode in order to measure the ion current from the source. The linear motion feedthrough used to move the Faraday cup in and out of the beam path is labelled as 5.

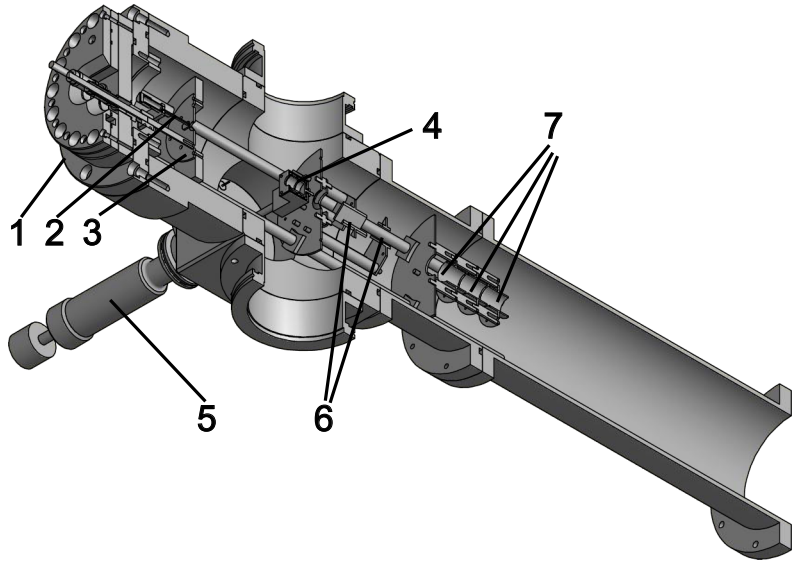

Figure 3.19: 3D cross-section view of the ion source vacuum chamber assembly: 1) ion source flange, 2) tantalum tube, 3) extractor electrode, 4) Faraday cup, 5) linear motion feedthrough, 6) horizontal and vertical steering plates, 7) Einzel lenses.

The next beam optics element shown in Figs. 3.18, 3.19 are the horizontal and vertical beam steerers. They consist of rectangular plates which can be supplied with a voltage in order to correct for any miss-stearing of the beam. This can be caused by a miss-alignment of the tantalum tube with respect to the central axis of the beamline.

Lastly, the beam optics elements labeled as 7 in Figs. 3.18, 3.19, are the Einzel lenses. The Einzel lenses consist of 3 equal cylinders, with the outer cylinders held at ground potential and the central one elevated to a higher potential V_E. The Einzel lenses focus the ion beam without changing its kinetic energy. The end of the long section of the ion source vacuum chamber is attached to the 90 degree bend, which is discussed in the following subsection.

90 degree bend

As can be seen in Fig. 3.6 from Sect. 3.4.3, the ion source section connects to the rest of the CRIS beamline at an angle of 90°. Previously a quadrupole was used to bend the ion beam by 90° into the CRIS beamline, but unfortunately

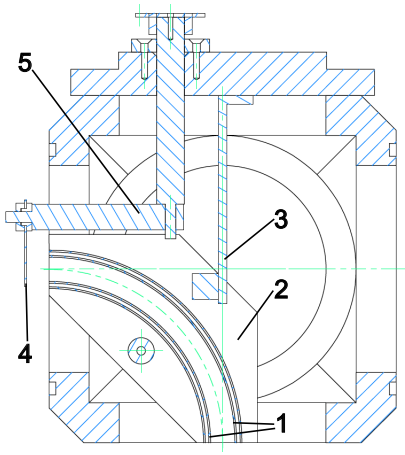

Figure 3.20: Top view cross-section of the 90 degree bend: 1) metal bending plates, 2) isolating TecaPEEK pieces, 3) metal holder, 4) Faraday cup plate, 5) rotating Farady cup holder.

the transmission of the beam through the bend could not always be reliably reproduced, which is why a new more robust system was needed. The design of a new 90 degree bend was made by Ronald Fernando Garcia Ruiz, another PhD student in the group of Gerda Neyens, together with Willy Schoovaerts. A technical drawing of the new 90 degree bend is given in Fig. 3.20, showing the top view of the cross-section of the cube inside of which the bend is mounted.

In Fig. 3.20, the metal plates that bend the ion beam are labelled as 1. These plates are supplied with voltages of equal value but opposite polarity. This creates an electrical field between the two plates that guides the ions around the bend. The elements labelled 2 in Fig. 3.20 are two isolating pieces (top and bottom) that hold the bending plates in place and make sure they keep their shape. The isolating pieces themselves are held with a metal holder (labelled 3), which is mounted onto a flange for inserting into the cube surrounding the 90 degree bend.

In order to measure the amount of ion beam that passes through the bend, a rotating holder was designed which could position a Faraday cup right after the bend, but also remove it out of the beam path after the measurement. The holder is labelled as 5 in Fig. 3.20, while the metal plate serving as the Faraday cup is labelled as 4. When the Faraday cup is not in use it can be rotated out of the central vertical axis, allowing the ion beam to pass into the CRIS beamline.

3.5.3 Ion source results

The design, manufacture, transportation and installation of the ion source at ISOLDE was performed during the CERN long shut-down period, with the first successful tuning of the beam through the CRIS beamline until the MCP achieved in March 2014. As a demonstration of the stability of the ion beam current delivered by the source, Figure 3.22 shows the ion beam current measured over a period of 3.5 h by the FC4 Faraday cup. This cup is located in the CRIS beamline between the 20 degree bend after the ultra high vacuum interaction region and the detection chamber, as can be seen in Fig. 3.21. Figure 3.21 also shows the positions of the other Faraday cups in the CRIS beamline, along with FC90 and FCIS which are the ion source Faraday cups. The exact location of FCIS within the ion source vacuum chamber was shown in Fig 3.19. It was not used as a benchmark for the ion beam transmission tests, since it was noticed during testing that the beam was too large at that point and therefore not collected fully by this Faraday cup. In its place FC90 was used as a benchmark for the transmission tests.

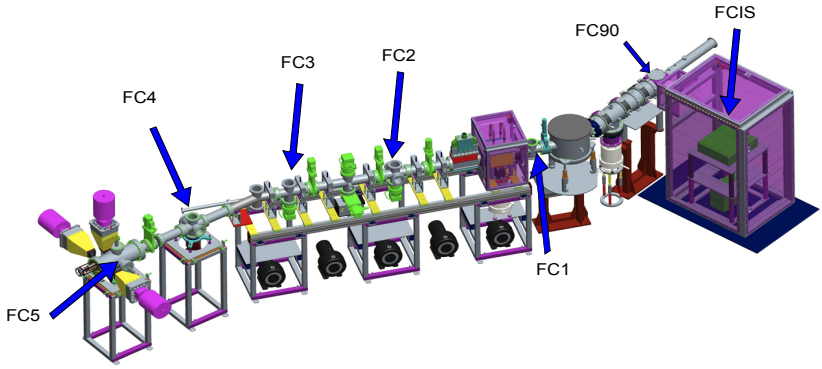

Figure 3.21: A 3D drawing of the CRIS beamline at ISOLDE, CERN, showing the locations of the Faraday cups used to measure the ion beam current. The locations of the Faraday cups during on-line experiments while taking beam from ISOLDE are the same, with the difference that FC0 is placed on the position of FC90 to measure the incoming ISOLDE beam.

As for the demonstrated beam stability, Figure 3.22 shows that the ion beam current gradually dropped from 6 pA down to 2 pA over the 3.5 h period. This highlights the improvements of the new ion source compared to the previous one. The ion beam from the first CRIS ion source could only reach this Faraday cup after many hours of beam tuning. The highest current obtained was on the order of 1 pA which was also severely fluctuating and would drop off to

zero unless it was continuously optimized. Another major issue of the previous source were the changing voltages necessary for a good beam transport, which would be different every time the beam tuning was performed.

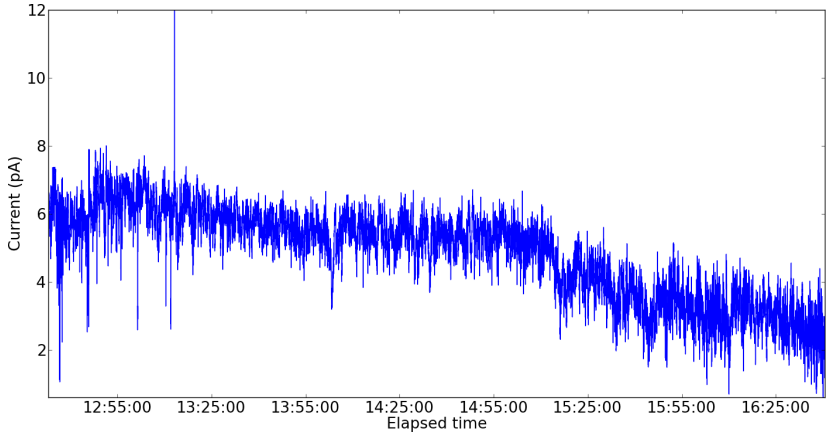

Figure 3.22: Stability of the ion source beam current on the FC4 Faraday cup. The y-axis shows the current given in pA and the x-axis shows the time in hours. For these measurements the source was filled with KCl.

The new ion source design demonstrates several advantages: 1) the voltage settings are reproducible, meaning that applying the same settings from a previous beam tune would produce a similar beam transport; 2) the beam tune is more stable (as seen in Fig. 3.22), meaning that the beam current gradually drops off in a period of several hours; 3) the alignment of the source beam optics are fixed, which contributes to the overall stability and beam transmission; 4) the highest stable operating voltage observed with the new source was 12 kV, compared to the previous source which ran at most up to 3 kV.

However, the source also has certain shortcomings: 1) the ion source beam transport measured from FC90, the Faraday cup after the 90 degree bend, until FC5, being the copper dynode in front of the MCP, is on average 1 % for a 5 kV ion beam; 2) even though the design goal of the source was 30 kV, the highest observed operating voltage was 15 kV before the voltage drops due to sparking; 3) the 90 degree bend needs to be physically removed from the beamline in order to receive beam from ISOLDE.

One possible reason for the low transmission of the beam was the lack of a vertical steering element in the CRIS beamline after the ion source region. If the ion source tube has an initial misalignment in the vertical direction, this can be compensated by the vertical steerer of the ion source, but since there

is no other vertical steerer in the CRIS beamline afterwards, the beam will gradually drift in the vertical direction towards the end of the CRIS beamline, which could account for losses of the beam.

Another likely reason for the low transmission observed is the fact that the beam was operated at a significantly lower voltage than the ISOLDE beam, making it too broad. Issues were encountered while trying to increase the voltage past 15 kV in the form of pressure spikes and sparks in the ion source voltage cage. It is possible to improve on this high voltage limit with the acquired experience of filling the source with a salt of different chemical properties in order to avoid such pressure spikes and by installing better high voltage cables which were purchased from Heinzinger. Due to time constraints and preparations for the experiments on radioactive ion beams, it was decided that for the purposes of the offline tests it was adequate to work with a 5 kV operating voltage, which was found to be the most stable. Extensive offline tests were performed in August 2014 during which the source operated continuously for a period of 7 days with no major problems. The results that will be presented further in this section originate from this testing period. Performing these offline tests was critical in order to prepare the experimental conditions for the subsequent high-resolution work on francium in November 2014.

Neutralization tests

One important test that can be performed using the offline ion source is the test of the neutralization efficiency of the charge exchange cell. This was done by applying a heating current to the charge exchange cell with the ion beam from the source passing through. By detecting the total beam of neutralized atoms and non-neutralized ions at the end of the interaction region using the FC3 Faraday cup, the neutralization efficiency can be calculated. When a positive ion beam impinges on a Faraday cup, it deposits charge on it which can be detected if the cup is electrically connected to an ammeter. The number of ions in the beam is then proportional to the current measured. However, the impact of the high energy beam will also produce secondary electron emission, which will increase the measured current signal. This effect can be reduced by using a suppressed Faraday cup, for which the geometric design is such that all of the secondary electrons will recombine via collisions with the surrounding walls of the cup. Since FC3 is a suppressed Faraday cup, it is thus possible to directly measure the ion current. As for an atom beam, since there will be no net charge delivered to the cup and if the secondary electrons are suppressed, then there will be no measurable current proportional to the number of atoms impinging on the cup. This problem can be circumvented by applying a positive voltage to a ring surrounding the Faraday cup which will then pull out the

secondary electrons and prevent them from recombining. This will produce an amplified signal of the current produced by the atoms. A measurement of the neutralization efficiency then consists of first measuring the real ion current on the cup by leaving the deflector plate after the charge exchange cell at 0 V thus allowing the non-neutralized ions to pass through, and leaving the voltage on the Faraday cup ring at 0 V. Then a positive voltage is applied to this ring which allows for the measurement of the amplified total ion + atom current. The last step is to apply a voltage on the deflector plate in order to kick-off the non-neutralized ions and detect only the amplified atom signal on the cup. Using these three values the total neutralization efficiency can be estimated as will now be demonstrated.

During one such neutralization efficiency measurement in August 2014 on a potassium beam, the charge exchange cell was held at 167.4 C°. With the deflector plate and the FC3 ring at 0 V the real ion current was measured as $I_{\text{ion}}^{\text{real}} = 12$ pA. Then by applying +200 V on the FC3 ring, the amplified ion + atom current was measured to be $I_{\text{atom + ion}}^{\text{amp}} = 32$ pA. Then by applying +300 V on the deflector plate, the measured amplified atom current was $I_{\text{atom}}^{\text{amp}} = 9$ pA. It was estimated that the real atom current was $I_{\text{atom}}^{\text{real}} = I_{\text{atom}}^{\text{amp}}/2 = 4.5$ pA. Thus if the amplified ion current is also estimated to be double the real current then the total amplified current is $I_{\text{ion+atom}}^{\text{amp}} = 2 \cdot I_{\text{ion}}^{\text{real}} + 2 \cdot I_{\text{atom}}^{\text{real}} = 2 \cdot 12 \text{ pA} + 2 \cdot 4.5 \text{ pA} = 33$ pA, in good agreement with the measured total amplified current. The neutralization efficiency can then be calculated as

$$\epsilon_{\text{neutr.}} = \frac{I_{\text{atom}}^{\text{real}}}{I_{\text{ion}}^{\text{real}} + I_{\text{atom}}^{\text{real}}} = \frac{4.5 \text{ pA}}{12 \text{ pA} + 4.5 \text{ pA}} = 27\% \tag{3.10}$$

^{39}K hyperfine structure

During the tests in August 2014 it was possible to measure the hyperfine structure of ^{39}K using the 769.9 nm $4s\ ^2S_{1/2} \rightarrow 4p\ ^2P_{1/2}$ atomic transition. The 769.9 nm transition was excited using a Coherent 899 continuous wave Ti:Sa laser, borrowed from the neighboring COLLAPS experiment, while the ionization step was provided by a 355 nm, 10 Hz Nd:YAG laser, borrowed from RILIS. The main factors that made these measurements possible was the stability of the ion source current and the chopping of the continuous wave laser light using a Pockels cell. During the initial tests with the ion source in May 2014 when the CW was not chopped, no ^{39}K hyperfine structure resonances could be observed. The most likely reason for this was the substantial loss in efficiency due to optical pumping effects with the continuous light. During the tests in August resonances were also not observed until the CW light was

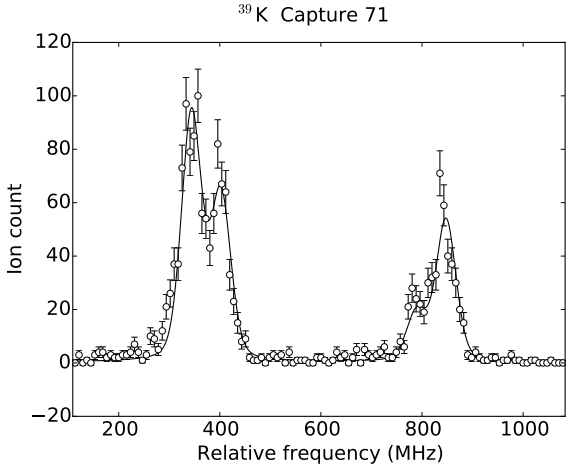

Figure 3.23: Fit of a hyperfine structure spectrum of ^{39}K measured using the new ion source. The data points are the total number of ion counts observed at a given laser frequency. The frequency on the x-axis is given relative to a constant value of 389 286 058.716(62) MHz [15] (the transition frequency) in order to keep the numbers small. The full width at half-maximum obtained from the fit was FWHM = 44(5) MHz

chopped. For a more detailed discussion on the CW chopping and the effects of changing the delay of the excitation and ionization step the reader is referred to Article II in Appendix A. As for the measurements performed in August 2014, Fig. 3.23 shows a representative hyperfine structure spectrum from one such measurement.

The hyperfine structure parameters were extracted from the data using the same procedure as will be described in Chapter 4 Sect. 4.2, as for the high-resolution francium results. A comparison of the experimental results for the ground state $A(^2S_{1/2})$ parameter and upper state $A(^2P_{1/2})$ parameter with literature values taken from Papuga et al., [21], is given in Table 3.3. The value for the ground state splitting differs from the literature value by 5 MHz, while the upper state splitting is in agreement. A possible reason for the discrepancy is the fact that the Highfinesse WSU2 wavemeter, which was used to measure the 769.9 nm laser wavelength while scanning accross the hyperfine structure, was not locked to a reference during the measurements but relied on an internal frequency calibration. This motivated the locking of this wavemeter to an external temperature stabilized HeNe laser during the November 2014 francium campaign.

Table 3.3: Comparison of the experimentally determined hyperfine structure values for the ground state $A(^2S_{1/2})$ and upper state $A(^2P_{1/2})$ parameters with literature values taken from Papuga *et al.*[21].

Parameter	Experiment (MHz)	Literature (MHz)
$A(^2S_{1/2})$	226(3)	231.0(3)
$A(^2P_{1/2})$	27.4(9)	27.8(2)

Another relevant result extracted from fitting the hyperfine structure was the Full width at half-maximum (FWHM) of the peaks FWHM = 44(5) MHz. This was already a significant improvement compared to the 1.5 GHz value obtained for the low-resolution francium data [5], providing confidence to perform high-resolution measurements on francium in November 2014. The main contribution to the FWHM value obtained from these offline measurements was the Doppler spread of the 5kV ion source beam. The estimated Doppler spread for a 5kV beam is 30.6 MHz, while the natural linewidth for this $2.6 \cdot 10^{-8}$ s transition is 6 MHz.

Saturation curve

As was mentioned in Sect. 3.2.3, knowing the saturation power of a particular atomic transition is important in order to know how high a laser power can be used while still avoiding significant power broadening effects. Figure 3.24 gives a saturation curve measured for the 355 nm ionizing step. The curve was made by performing several measurements with varying 355 nm laser powers (given in mJ/pulse), while scanning the excitation 769.9 nm laser step across the left doublet hyperfine structure in Fig. 3.23. The total number of counts within each scan was divided by the total measurement time giving the normalized ion rate value on the y-axis in Fig. 3.24.

By fitting the data in Fig. 3.24 as was done in Article II, Appendix A with

$$I(P) = A\frac{P/P_0}{1 + P/P_0}, \tag{3.11}$$

where A is a scaling parameter, P is the laser power and P_0 the saturation power, the saturation power value of $P_0 = 8 \pm 3$ mJ/pulse is obtained.

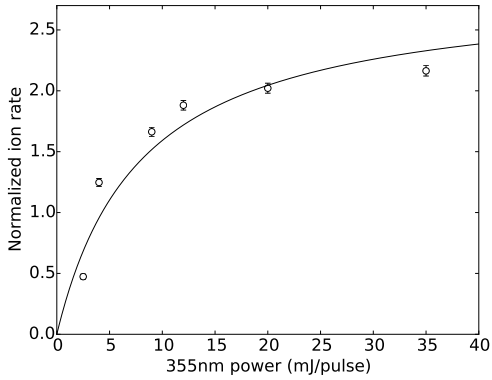

Figure 3.24: Saturation curve for the 355 nm ionizing step. The data points originate from 6 scans over the left doublet of the potassium hyperfine structure from Fig. 3.23. The normalized ion rate is explained in the text.

Chapter 4

Experimental results

This chapter will describe the analysis procedures used on the experimental results from the 2012 low-resolution and 2014 high-resolution experimental campaigns. First the conversion of the data is described, followed by the fitting procedure performed for extracting the hyperfine structure parameters. The data is then compared to reference values from literature and finally the new results for the magnetic dipole moments and changes in mean-square charge radii from the low-resolution results are given. For the high-resolution results the new spectroscopic quadrupole moment value of ^{219}Fr is presented.

4.1 Low-resolution results

4.1.1 Raw data conversion

The data acquisition system used in the 2012 experimental campaign was described in Sect. 3.4.6. This system saved the data in a .txt format, with the first line displaying all of the recorded variables and their respective positions within each line: "[Trigger #] [Time] [Date] [RILIS Wavenumber] [RILIS Power] [1064 nm Power] [Pressure] [HRS Proton Current] [PSB Cycle Number] [HRS Protons per Pulse] [Start Supercycle] [Protons for HRS] [RILIS Linewidth] [LeCroy Data]". The data used for extracting the hyperfine structure parameters were [RILIS Wavenumber] – providing information about the excitation step laser frequency in the lab frame and [LeCroy Data] – providing the number of ion counts detected at the respective laser frequency.

The procedure for changing the laser frequency and the synchronization with the rest of the measured experimental values was explained previously in Chapter 3, Section 3.4.6. During a measurement on a set frequency, the DAQ program saved data every 32 ms, after the CRIS Nd:YAG flash lamp trigger, as was described in Sect. 3.4.5. This meant that the counts would keep piling up for each laser frequency, but only the total number of counts per each laser frequency was important. Only the final count number was extracted by looking for the line in which the time difference was larger than a set value, corresponding to the down time while the laser frequency was being changed with the RILIS REACT software. The number of counts from the last line before the large time difference were always taken as the total number of counts for that wavenumber. This also accounted for the fact that the scope sometimes accumulated counts while resetting, before starting to accumulate counts for the new laser frequency.

The extracted laser wavenumber $\tilde{\nu}_L$, read in units of cm^{-1}, was first converted to a frequency ν_L by:

$$\nu_L = 100 \cdot 2 \cdot c\,\tilde{\nu}_L, \tag{4.1}$$

where c is the speed of light given in m/s, the factor 100 comes from the unit conversion from cm^{-1} to m^{-1} and the factor 2 comes from the fact that the wavenumber in the data file corresponds to the fundamental output of the RILIS Ti:Sa laser before being frequency doubled. This leaves the frequency in Eq. 4.1 in units of $\mathrm{s}^{-1} = \mathrm{Hz}$. This laser frequency is then converted to the frequency seen in the rest frame of the atomic beam by applying formulas (35) and (36) from [104]

$$\nu = \nu_L \frac{1-\beta}{\sqrt{1-\beta^2}} \tag{4.2}$$

$$\beta = \sqrt{1 - \frac{m^2c^4}{(eU+mc^2)^2}} \approx \sqrt{\frac{2eU}{mc^2}}, \tag{4.3}$$

where U is the ISCOOL voltage and $\mathrm{m}c^2 = (\frac{M_{excess}}{u_{eV}} + A)u_{eV}$, where $u_{eV} = 931.494061 \cdot 10^6\mathrm{eV}$ and M_{excess} is the literature value of the mass excess given in eV. The ISCOOL voltage was monitored during the beam time and was stable at 49970 V, with a drift of less than ± 1 V. Due to the relatively large errors on the extracted hyperfine structure parameters and isotope shifts which will be discussed in the following sections, the uncertainty originating from the ISCOOL voltage was not taken into account for this low-resolution data set. This uncertainty will however play a role in the analysis of the high resolution data in Sect. 4.2. As for the frequency obtained from Eq. 4.2, it was converted into MHz and 709258.16(12) GHz (calculated from $\tilde{\nu} = 23658.3058(40)\mathrm{cm}^{-1}$ [105] for this transition) were always subtracted in order to keep the numbers

small. Thus the final values will always be displayed as relative frequencies to that number.

During a measurement on a given frequency the frequency value drifts around the set value. To account for this the frequency value was saved for each trigger and the average value given by $\frac{1}{N}\sum_{i=1}^{N}\nu_i^{\text{drift}}$ was taken as the final frequency value. Rather than taking the statistical error on the frequency distribution, an error of 100 MHz was taken originating from the uncertainty on the wavemeter read-out.

4.1.2 Fitting procedure

Since it was necessary to take into account the error on the frequency as well as the error on the ion counts, the orthogonal distance regression ODRPACK package from Scipy was used [106]. During this experimental campaign, the resolution was mainly limited by the 1.5 GHz linewidth of the RILIS laser, resulting in a fully Gaussian profile of the hyperfine structure peaks. The spectra were thus fitted with a pure Gaussian shape of the form

$$G(\nu) = b + \sum_{i=1}^{N} I_0 I_i \exp\left(-\frac{\left(\nu - \left(\nu_0 - \frac{A_{low}C^i_{low}}{2} + \frac{A_{up}C^i_{up}}{2}\right)\right)^2}{2\left(\frac{HWHM}{\sqrt{2\ln 2}}\right)^2}\right), \tag{4.4}$$

where b is a constant background fit parameter; N is the total number of HFS transitions; I_0 is the fit parameter for the total intensity of a ground state HFS multiplet; I_i is the relative intensity of one of the peaks within a multiplet, calculated from the angular momentum coupling rules, given in Eq. 4.5; ν_0 is the fit parameter for the centroid; A_{low} is the $A(7s\ ^2P_{3/2})$ fit parameter; C^i_{low} is the C constant $C = F(F+1) - I(I+1) - J(J+1)$ calculated for $F = F_i, J = J_{low} = 1/2$; A_{up} is taken as $A(7s\ ^2P_{3/2})A(8p\ ^2P_{3/2})/A(7s\ ^2P_{3/2})$ where $A(8p\ ^2P_{3/2})/A(7s\ ^2P_{3/2}) = 0.00361(2)$ from [105]; C^i_{up} is the C constant calculated for $J_{up} = 3/2$; HWHM is the fit parameter for the half-width at half-maximum.

Each HFS peak was fitted with a Gaussian of the form from Eq. 4.4, with each peak having its own I_i, C^i_{low}, C^i_{up}, while the left and right HFS multiplets had their own I_0 value ($I_0^{L,R}$). The I_i relative peak intensities were fixed via the angular momentum coupling rules [107]:

$$\begin{aligned} I_i &= \sum_{m_{F_j}, m_{F_i}} (2J_{low}+1)(2F_i+1)(2F_j+1) \\ &\quad \times \begin{pmatrix} F_j & 1 & F_i \\ -m_{F_j} & 0 & m_{F_i} \end{pmatrix}^2 \begin{Bmatrix} J_{up} & F_j & I \\ F_i & J_{low} & 1 \end{Bmatrix}^2 \end{aligned} \tag{4.5}$$

where $\begin{pmatrix} F_j & 1 & F_i \\ -m_{F_j} & 0 & m_{F_i} \end{pmatrix}$ is a Wigner 3J symbol and $\begin{Bmatrix} J_{up} & F_j & I \\ F_i & J_{low} & 1 \end{Bmatrix}$ is a Wigner 6J symbol.

4.1.3 Reference isotopes

Since the 2012 experimental campaign marked the first physics run with the CRIS beamline, it was important to perform reference measurements in order to compare the results obtained with this technique to literature. The reference isotopes in this campaign were ^{207,211,220,221}Fr. The extracted experimental values for $A(7s\ ^2S_{1/2})$ for these isotopes were then compared to the known literature values in order to estimate the experimental systematic uncertainty.

The experimental parameters extracted from the fit were the ground state hyperfine parameter $A(7s\ ^2S_{1/2})$ and the centroid value ν_0. The weighted mean μ of these values from the different scans performed was calculated by

$$\mu = \frac{\sum_{i=1}^{N}(x_i\omega_i)}{\sum_{i=1}^{N}(\omega_i)}, \tag{4.6}$$

where x can be $A(7s\ ^2S_{1/2})$ or ν_0 and $\omega_i = \frac{1}{\sigma_i^2}$. The statistical error was defined as

$$\sigma_{\text{stat}} = \frac{1}{\sum_{i=1}^{N}\omega_i}, \tag{4.7}$$

and the weighted sample variance as

$$\sigma^2_{\text{weighted}} = \frac{\sum_{i=1}^{N}\omega_i(x_i-\mu)^2}{\sum_{i=1}^{N}\omega_i}. \tag{4.8}$$

The final uncertainty σ_{max} was then taken as the maximum of the two values σ_{stat} and σ_{weighted}

$$\sigma_{\text{max}} = \max(\sigma_{\text{stat}}, \sigma_{\text{weighted}}). \tag{4.9}$$

The calculated weighted means for the $A(7s\ ^2S_{1/2})$ parameters for ^{207,211,220,221}Fr are compared to the literature values in Table 4.1. It is clear

Table 4.1: Comparison between the experimentally obtained values for $A(7s\ ^2S_{1/2})$ of ^{207,211,220,221}Fr with values reported in literature.

Isotope	$A_{\mathrm{exp}}(7s\ ^2S_{1/2})$(MHz)	$A_{\mathrm{lit}}(7s\ ^2S_{1/2})$(MHz)
^{207}Fr	+8480(20)	+8484(1) [28]
^{211}Fr	+8710(50)	+8713.9(8) [28]
^{220}Fr	-6520(40)	-6549.2(12) [105]
^{221}Fr	+6200(30)	+6209.9(10) [105]

Table 4.2: Centroid values extracted from the fits of the reference isotope hyperfine spectra.

Isotope	ν_0 (GHz)
^{207}Fr	+27.29(5)
^{211}Fr	+22.91(3)
^{220}Fr	+1.49(8)
^{221}Fr	-1.16(7)

that the experimental values for $A(7s\ ^2S_{1/2})$ agree well with literature for these reference isotopes. The final experimental uncertainty which was used in all of the publications based on this work [2, 1, 3, 5], was taken from the 30 MHz scatter for ^{221}Fr, which was the most thoroughly studied reference isotope.

Table 4.2 gives the final weighted mean values with uncertainties for the centroids of the reference isotopes. These centroid values were used to calculate the isotope shift and relative mean-square charge radius in Sect. 4.1.6.

4.1.4 Neutron rich francium isotopes

The fit results for the newly measured neutron rich francium isotopes ^{218m,219,229,231}Fr are given in Table 4.3. These results depend on the assumed nuclear spin I, but there are no firm spin assignments for ^{218m,229,231}Fr. The most reliable literature value for the spin of ^{218m}Fr is a tentative 9^- assignment from [108], which was used in this analysis. For ^{219}Fr, Browne *et al.* [109] assign a value of $9/2^-$ based on favored α decay (HF=3.3) to ^{211}Bi g.s. ($I^\pi = 9/2^-$). There is no experimental information about the spin of ^{229}Fr, but Borge *et al.* [110] assume a spin of $1/2^+$ based on systematics from the other francium isotopes [28]. Fraile *et al.* tentatively assign a spin of $1/2^+$ for ^{231}Fr. This assignment is based on a characteristic β- decay pattern between the 1/2[400] and 1/2[501] configurations observed in the close vicinity of ^{231}Ra.

Table 4.3: Hyperfine parameter $A(7s\ ^2S_{1/2})$ and centroid ν_0 values for the neutron rich francium isotopes.

Isotope	I^π	$A(7s\ ^2S_{1/2})$ (GHz)	ν_0 (GHz)
^{218m}Fr	(8^-) [111]	+3.30(3)	+7.00(2)
	(9^-) [112, 108]	+2.95(3)	+7.09(2)
^{219}Fr	$9/2^-$ [109]	+6.82(3)	+4.44(2)
^{229}Fr	$(1/2^+)$ [110]	+30.08(11)	−19.51(5)
^{231}Fr	$(1/2^+)$ [113]	+30.77(13)	−23.29(5)

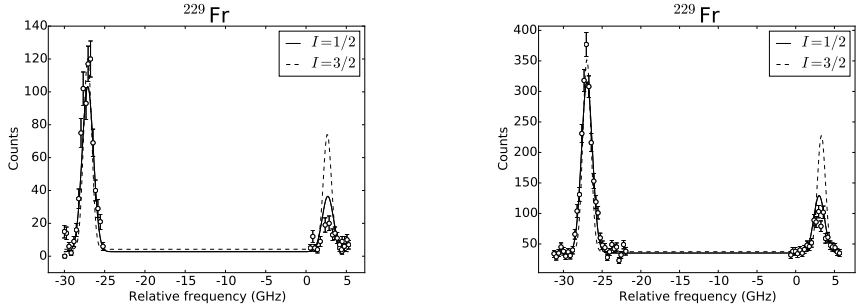

(a) Run 279-280 (b) Run 284

Figure 4.1: Result of using the fitting procedure described in Sect. 4.1.2, while keeping the intensity ratios fixed relative to Eq. 4.5. The solid line is the result of the fit assuming $I^\pi = 1/2^+$ for the ground state of ^{229}Fr while the dashed line is the result of the fit assuming $I^\pi = 3/2^+$.

Fixed intensity ratio fits

A supporting argument given in the discussion of Article I for the tentative assignment of a spin $1/2^+$ for ^{229}Fr comes from fitting the hyperfine spectra with a fixed intensity ratio between the two multiplets and assuming different spins. The intensity ratio was fixed by giving the same intensity parameter I_0 for both HFS multiplets in Eq. 4.4, instead of having two independent ones. In this way the relative intensities between the two multiplets were correlated via Eq. 4.5. The graphs obtained for ^{229}Fr following this procedure for Run 279-280 and Run 284 are shown in Fig. 4.1, while the result for Run 282 was used in Article I, Ch. 5, Sect. 5.2. For these fits it is relevant to bear in mind that as mentioned in Sect. 4.1.2, the fitting procedure also took into account a 100 MHz error on the frequency points.

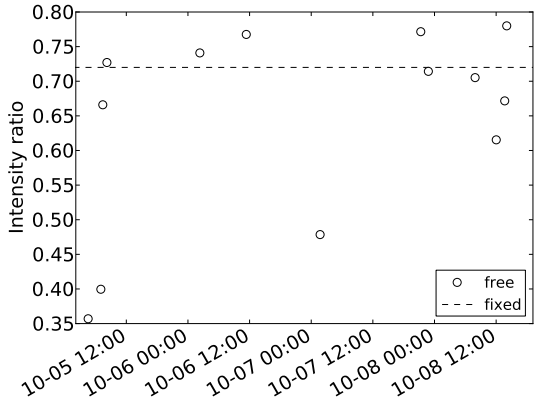

Figure 4.2: Ratio between the two hyperfine structure amplitudes obtained from fits to ^{221}Fr hyperfine spectra. The x axis shows the month-day and time when the spectrum was measured. The white circles were obtained by keeping the ratios between multiplets free, while the black dashed line shows the fixed ratio constrained by Eq. 4.5.

As a reference the same procedure was carried out for ^{221}Fr, assuming only a spin $9/2^-$, as shown in Fig. 4.2. Here the dashed line represents the ratio of the height of the HFS multiplets for a fixed intensity ratio of spin $9/2^-$ and the open circles represent independent intensity ratios obtained from the fitted spectra. The free values scatter around the fixed value implying that the procedure holds some value, but several points lie well below the black circles indicating that the experimental conditions were not constant at all times. Therefore this procedure could not be used to make a firm spin assignment, but rather as a supporting argument for the tentative (1/2) assignment in Article I.

The same procedure did not yield conclusive results when applied to the hyperfine spectrum of ^{231}Fr. For this isotope the statistics were lower due to the lower production yield and a base background rate of ~ 30 counts reduced the signal-to-noise ratio. This background was also present during the scans of ^{230,232}Fr and is thought to originate from radium. The background disappeared when the 1064 nm CRIS Nd:YAG laser was blocked. This led to an assumption that the background originated from radium atoms which were in an excited metastable state after collisional charge exchange in the CRIS charge exchange cell. A possible candidate for such a metastable state is the $^3F_2$ state at 31172 cm^{-1} predicted to have a 3 s lifetime by Dzuba *et al.* [114].

4.1.5 Magnetic dipole moment

The formula used for calculating the magnetic dipole moment μ from the $A(7s\ ^2S_{1/2})$ values given in Table 4.3 was

$$\mu_{exp} = \frac{A_{exp}(7s\ ^2S_{1/2})I_{exp}\mu_{ref}}{A_{ref}(7s\ ^2S_{1/2})I_{ref}}, \tag{4.10}$$

where the reference values were: $A_{ref}(7s\ ^2S_{1/2})(^{210}\mathrm{Fr}) = 7195.1(4)$ MHz [28], $I_{ref}(^{210}\mathrm{Fr}) = 6$ [115] and $\mu_{ref}(^{210}\mathrm{Fr}) = 4.38(5)\ \mu_N$ [116]. The final values are given in Table 4.4.

Table 4.4: Magnetic dipole moments for ^{218m,219,229,231}Fr obtained from the experimental $A(7s\ ^2S_{1/2})$ values.

Isotope	I^π	μ_{expt} (μ_N)
^{218m}Fr	(8^-) [111]	2.68(4)
	(9^-) [112, 108]	+2.70(4)
^{219}Fr	$9/2^-$ [109]	+3.11(4)
^{229}Fr	$(1/2^+)$ [110]	+1.53(2)
^{231}Fr	$(1/2^+)$ [113]	+1.56(2)

4.1.6 Charge radii

In order to extract the changes in nuclear mean-square charge radii from the isotope shift results, the field and mass shift factors from Eq. 2.20 first needed to be determined. These values were calculated for the $(7s\ ^2S_{1/2} - 7p\ ^2P_{3/2}) - \mathrm{D2}$ line in francium by Dzuba *et al.*[22]. Since all of the CRIS measurements were performed in the $(7s\ ^2S_{1/2} - 8p\ ^2P_{3/2}) - \mathrm{D2'}$ line, a King plot was made relating the two transitions. The isotope shifts of ^{213,220,221}Fr relative to ^{212}Fr for the D2' line were taken from Duong *et al.*[105] and compared with the respective values from Coc. *et al.*[28] for the D2 line. Additionally, the isotope shifts for ^{207,211}Fr from CRIS were compared to the ones from [28]. Since the reference isotope in this work was ^{221}Fr, the isotope shifts were calculated relative to this isotope by

$$\delta\nu^{A,221} = \nu_0(A) - \nu_0(^{221}\mathrm{Fr}). \tag{4.11}$$

The minimum uncertainty for all of the reported isotope shifts was quoted as 100 MHz, which was determined from investigating the scatter of the ^{221}Fr centroid values between scans and the long term drift in the centroid frequency

Table 4.5: Isotope shift values for ^{218m,219,229,231}Fr relative to ^{221}Fr.

Isotope	I^π	$\delta\nu^{A,221}$ (GHz)
^{218m}Fr	(9^-) [108]	+8.24(10)
^{219}Fr	$9/2^-$ [109]	+5.59(10)
^{229}Fr	$(1/2^+)$ [110]	−18.36(10)
^{231}Fr	$(1/2^+)$ [113]	−22.14(10)

of ^{221}Fr during the course of the experiment [4, 3]. The isotope shifts obtained for ^{218m,219,229,231}Fr are given in Table 4.5.

In order to compare the CRIS values for ^{207,211}Fr to the ones from Coc. *et al.*[28], these literature values were converted to be relative to ^{221}Fr by

$$\delta\nu_{\text{lit}}^{A,221} = \delta\nu_{\text{lit}}^{A,212} + \delta\nu_{\text{lit}}^{212,221}, \tag{4.12}$$

where $\delta\nu_{\text{lit}}^{212,221} = +23570(2)$ MHz. The mass factor[1] $\mu_{A,A^{ref}} = \frac{AA^{ref}}{A-A^{ref}}$ was multiplied with the isotope shift and the product $\mu_{A,A^{ref}}\delta\nu_{is}^{A,A^{ref}}$ for both the D2 and D2' transition was plotted. The resulting King plot is given in Figure 4.3.

As seen in Sect. 2.4.4, the modified isotope shifts for the two transitions are related by

$$\mu_{A,A^{ref}}\delta\nu_{D2'}^{A,A^{ref}} = \frac{F_{D2'}}{F_{D2}}\mu_{A,A^{ref}}\delta\nu_{D2}^{A,A^{ref}} + (K_{NMS}^{D2'} + K_{SMS}^{D2'}) - \frac{F_{D2'}}{F_{D2}}(K_{NMS}^{D2} + K_{SMS}^{D2}). \tag{4.13}$$

From Fig. 4.3, the ratio $\frac{F_{D2'}}{F_{D2}} = 0.995(3)$ and the value $(K_{NMS}^{D2'} + K_{SMS}^{D2'}) - \frac{F_{D2'}}{F_{D2}}(K_{NMS}^{D2} + K_{SMS}^{D2}) = 799(339)$ GHz u are extracted. The calculated field and mass shift factors from [22] are : $F^{D2} = -20766(208)$ MHz/fm^2, $K_{NMS}^{D2} = 229.0$ GHz u and $K_{SMS}^{D2} = -314(113)$ GHz u. Based on these values, the values obtained from Fig. 4.3 and the formula

$$K_{NMS} = \frac{\nu_{exp}}{1822.888} \tag{4.14}$$

where 709258.16(12) GHz [105] is the transition frequency, the field and mass shift factors for the D2' transition were obtained: $F_{D2'} = -20.67(21)$ GHz/fm^2,

[1]The masses were always calculated taking the mass excess into account. For example A(^{221}Fr)=221.014255 amu

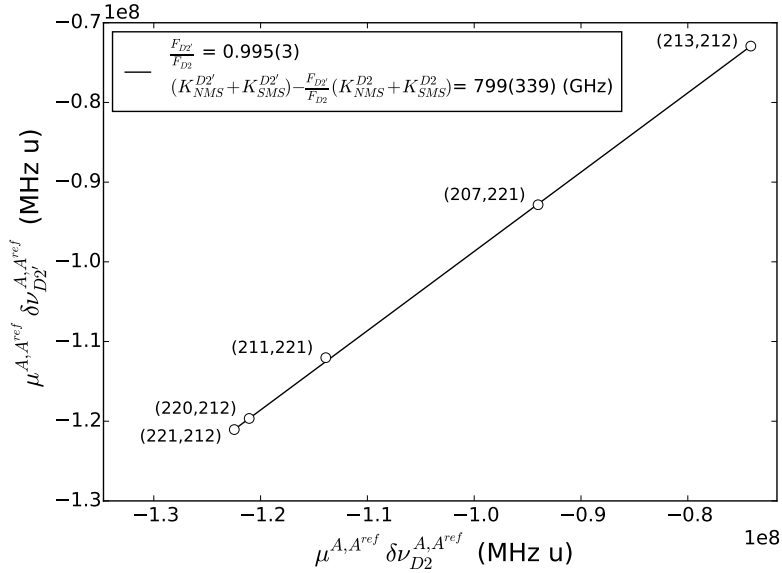

Figure 4.3: King plot for the $(7s\ ^2S_{1/2} - 7p\ ^2P_{3/2}) - \mathrm{D2}$ and $(7s\ ^2S_{1/2} - 8p\ ^2P_{3/2}) - \mathrm{D2'}$ transitions in francium.

$K^{D2'}_{SMS} = 360(330)$ GHz u and $K^{D2'}_{NMS} = 389$ GHz u. Using these values and Eq. 2.20 from Sec. 2.4.3, the change in mean square charge radii can be calculated by

$$\delta\langle r^2\rangle^{A,A^{ref}} = \frac{\delta\nu^{A,A^{ref}} - \frac{A-A^{ref}}{A\cdot A^{ref}}\cdot(K_{NMS}+K_{SMS})}{F}. \tag{4.15}$$

The results for ^{218m,219,229,231}Fr calculated relative to ^{221}Fr are given in Table 4.6. In this table the error originating from the experimental isotope shift uncertainty is quoted in parentheses, while the total error taking into account the uncertainties originating from the theoretical mass and field shift values is given in curly braces. This will be relevant in the discussion of the charge radii in Article I, where a comparison is made to radium which has large theoretical uncertainties for the field and mass shifts.

In order to compare the CRIS mean-square charge radii results to the literature ones from Dzuba *et al.*[22] and the results for radium from Wansbeek *et al.*[117], the francium values were converted to be relative to ^{213}Fr, since this is the isotope with $N = 126$. This was done by first converting the literature

Table 4.6: Changes in mean-square charge radii for ^{218m,219,229,231}Fr relative to the reference ^{221}Fr. The errors in parentheses originate from the experimental 100 MHz uncertainty on the isotope shift, while the errors given in curly braces take into account the theoretical errors of the field and mass shift factors.

Isotope	I^π	$\delta\langle r^2\rangle^{A,221}$ (fm^2)
^{218m}Fr	(9^-) [108]	$-0.401(5)\{6\}$
^{219}Fr	$9/2^-$ [109]	$-0.272(5)\{6\}$
^{229}Fr	$(1/2^+)$ [110]	$+0.894(5)\{11\}$
^{231}Fr	$(1/2^+)$ [113]	$+1.078(5)\{12\}$

Table 4.7: Changes in mean-square charge radii from Dzuba *et al.*[22] and this work, converted to be relative to ^{213}Fr.

A	$\delta\langle r^2\rangle^{A,213}$ [fm^2]	A	$\delta\langle r^2\rangle^{A,213}$ [fm^2]
207	-0.331(3)	221	+1.055(11)
208	-0.319(3)	222	+1.185(13)
209	-0.230(2)	223	+1.265(14)
210	-0.204(2)	224	+1.408(15)
211	-0.122(1)	225	+1.475(16)
212	-0.079(1)	226	+1.576(17)
213	0	227	+1.767(19)
218m	$+0.654(5)\{13\}$	228	+1.850(19)
219	$+0.783(5)\{13\}$	229	$+1.949(5)\{16\}$
220	+0.922(10)	231	$+2.133(5)\{17\}$

values using

$$\delta\langle r^2\rangle_{\text{lit}}^{A,213} = \delta\langle r^2\rangle_{\text{lit}}^{A,212} - \delta\langle r^2\rangle_{\text{lit}}^{213,212}. \tag{4.16}$$

Then using the obtained $\delta\langle r^2\rangle_{\text{lit}}^{221,213} = 1.055(11)$ fm^2 value, the CRIS values from Table 4.6 were converted by

$$\delta\langle r^2\rangle_{\text{CRIS}}^{A,213} = \delta\langle r^2\rangle_{\text{CRIS}}^{A,221} + \delta\langle r^2\rangle_{\text{lit}}^{221,213}. \tag{4.17}$$

The final converted values used in the plots in Article I are given in Table 4.7, where the errors were obtained via standard error propagation.

4.2 High-resolution results

4.2.1 Raw data conversion

The data acquisition system used during the 2014 experimental campaign was explained in Chapter 3, Section 3.4.6. This system saved the data in a .txt file with the information on the time, laser scanning voltage, laser wavenumber and ion counts. The wavenumber from the data files was converted to frequency by following the same procedure outlined in Sect. 4.1.1. Since in this data acquisition system the ion counts were not accumulated for a given frequency but continuously saved for each trigger, the final ion counts per frequency were obtained by binning the data for a chosen range of the laser frequency. The width of the bins was used as the uncertainty on the frequency.

As for the ion counts, for this data set from 2014 it was decided to present the data in ions/s. This was done by calculating a mean of the ions within each frequency bin. The error on this ion rate σ_{rate}, was calculated from the N individual rate errors $\sigma_{\text{i rate}}$ within a frequency bin by

$$\sigma_{\text{rate}} = \frac{\sqrt{\sum_{1}^{N} \sigma_{\text{i rate}}^2}}{N}. \tag{4.18}$$

4.2.2 Fitting procedure

Due to the high-resolution achieved during the 2014 experimental campaign it was necessary to refine the fitting procedure compared to the low-resolution procedure, since there the spectra were fit with a pure Gaussian function. It was thus necessary to take into account the Lorentzian component of the spectral profile. This was done by using a pseudo-Voigt function to fit the data defined as

$$V_P(\nu) = (1-\eta)G(\nu;\sigma) + \eta L(\nu;\Gamma_L) + b, \tag{4.19}$$

where b is a background parameter, η is a parameter defining the fraction of the Gaussian $G(\nu;\sigma)$ and Lorentzian profiles $L(\nu;\Gamma_L)$ in the total pseudo-Voigt function. The parameter σ is related to the Gaussian full width at half-maximum Γ_G by $\sigma = \Gamma_G/2\sqrt{2\log 2}$. In the pseudo-Voigt approach the Lorentzian and Gaussian widths are constrained to be equal: $\Gamma_L = \Gamma_G$.

The Gaussian profile was defined as

$$G(\nu;\sigma) = \sum_{1}^{N} \frac{I_0^i I_i}{\sigma\sqrt{2\pi}} e^{-\frac{(\nu-x)^2}{2\sigma^2}}, \tag{4.20}$$

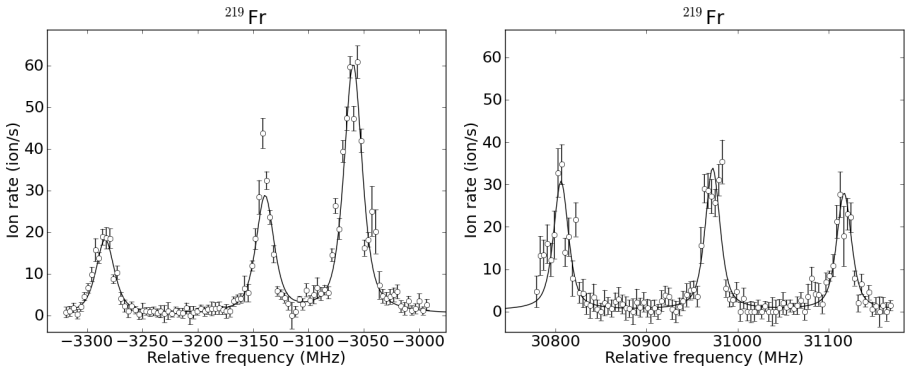

(a) Left multiplet (b) Right multiplet

Figure 4.4: Example hyperfine spectrum of ^{219}Fr measured with high resolution and fitted with the described fitting procedure. It is possible to determine the spectroscopic quadrupole moment since all peaks are resolved.

and the Lorentzian profile was defined as

$$L(\nu;\Gamma_L) = \sum_1^N \frac{I_0^i I_i}{\pi} \frac{\Gamma_L/2}{(\nu - x)^2 + (\Gamma_L/2)^2} \tag{4.21}$$

where

$$x = \nu_0 - \frac{A_{low}C_{low}^i}{2} + \frac{A_{up}C_{up}^i}{2} + B\frac{\frac{3}{4}C(C+1) - I(I+1)J(J+1)}{2I(2I-1)J(2J-1)}. \tag{4.22}$$

The parameters used in Eq. 4.4 and Eq. 4.22 are: I_0^i scaling factor for the intensity of the peak, I_i relative peak intensity calculated from Eq. 4.5, B is the hyperfine parameter related to the quadrupole moment as was seen in Chapter 2 and the rest of the parameters are the same as in Sect. 4.1.2. The B parameter was kept at 0 for the low-resolution fits, as they were not sensitive to it. Figure 4.4 shows an example hyperfine spectrum of ^{219}Fr which was fitted using this procedure.

4.2.3 Comparison with low-resolution results

Figure 4.5 shows a comparison between the low resolution and high resolution data in terms of resolving the upper state $8p\ ^2P_{3/2}$ hyperfine structure in the example of the right hyperfine multiplet of ^{221}Fr. The figure was obtained by

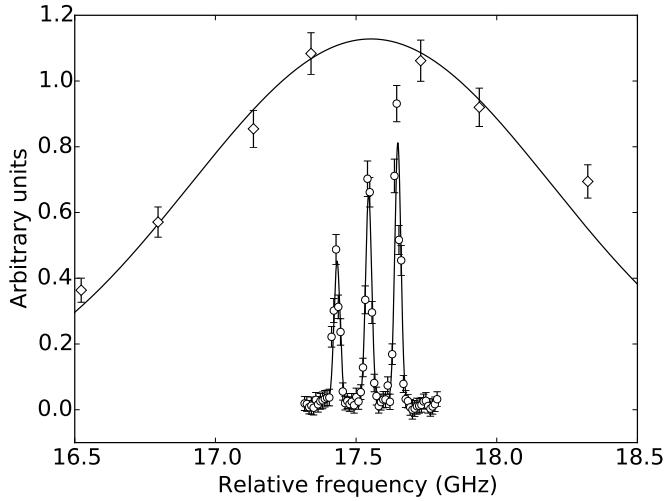

Figure 4.5: Comparison between the resolution of the upper state $8p\ ^2P_{3/2}$ hyperfine structure of ^{221}Fr between the data from 2012 and 2014. The y axis in the plot is given in arbitrary units, since the data was re-scaled so that all points on the plot are clearly visible. The diamond points are the data from 2012, while the circles represent the data from 2014.

taking data for ^{221}Fr from the 2012 and 2014 campaign and fitting the data sets independently from each other and then re-scaling them so that all data points can clearly be seen. Therefore the y axis in the plot is given in arbitrary units and does not represent a comparison in observed rates between the two experiments. The effect of the higher resolving power obtained during the 2014 experimental campaign however, is clearly visible.

As for the values obtained from the high-resolution data set, Table 4.8 gives a comparison between the hyperfine parameters extracted for the reference isotope ^{221}Fr from the high-resolution data and the results from the low-resolution experiment along with literature values. The $A(7s\ ^2S_{1/2})$ parameter compares well to the low-resolution experimental values and literature. The $A(8p\ ^2P_{3/2})$ parameter agrees with literature within the experimental uncertainty of 0.5 MHz. The value of $B(8p\ ^2P_{3/2})$ corresponds to the literature value within the quoted 2 MHz uncertainty. The uncertainties on the experimental values originate from the scatter of the data as was described in Sect. 4.1.3.

Table 4.8: Comparison between the extracted hyperfine parameters for ^{221}Fr compared to the values obtained from the low-resolution data and literature.

Parameter	Exp. 2014	Exp. 2012	Literature
$A(7s\ ^2S_{1/2})$ (MHz)	+6209(1)	+6200(30)	+6209.9(10) [105]
$A(8p\ ^2P_{3/2})$ (MHz)	+22.3(5)	-	+22.4(1) [105]
$B(8p\ ^2P_{3/2})$ (MHz)	−87(2)	-	−85.7(8) [105]

However, since this data was measured with more precision compared to the data from 2012, it is now important to take into account certain systematic effects. One such effect is the uncertainty of the absolute value of the ISCOOL voltage and the drift over time of this voltage. The ISCOOL voltage was written down for each individual scan and used in the extraction of the data, which compensated any changes that would occur from a drift. As for the absolute value of the ISCOOL voltage, it has been observed in COLLAPS experiments to be on the order of 15 V lower than the readout voltage [118]. However, it was recently brought to the attention of the collaboration that the voltage readout on ISCOOL was noticed to be 600 V lower than the absolute value for a voltage of 30 kV during an experiment in June 2015. It is possible that this large shift was present since the restart of ISOLDE after the long shutdown period and therefore needs to be taken into account in the analysis of the high-resolution francium results. At 40 kV this is estimated to correspond to an 800 V shift. In order to estimate the systematic effect this would have on the extracted values, the experimental value of the ISCOOL voltage was offset by +800 V and the fitting procedure described in the previous section was repeated for all of the scans of ^{219,221}Fr. The resulting hyperfine structure parameter values $A(7s\ ^2S_{1/2}), A(8p\ ^2P_{3/2})$ and $B(8p\ ^2P_{3/2})$ did not change within the statistical uncertainties. The value for the isotope shift of $\delta\nu^{A,221}$ (MHz) for ^{219}Fr was however shifted by +20 MHz. Therefore a systematic error of 20 MHz needs to be introduced for the isotope shift value.

Another possible systematic effect is the uncertainty on the frequency readout of the resonant excitation laser step. A drift of ±2 MHz was observed for each frequency by looking at the individual files for ^{221}Fr. The effect of this drift on the extracted experimental values was investigated by using the ODRpack package as described in Sect. 4.1.2 to include this uncertainty in the frequency values in the fit. This procedure showed that the extracted experimental values did not differ outside of the statistical uncertainties. Therefore this effect does not contribute significantly to the total systematic uncertainty.

Table 4.9 compares the values obtained for ^{219}Fr from the high-resolution data to the equivalent values obtained from the low-resolution data. The

Table 4.9: Comparison between the high-resolution and low-resolution results for ^{219}Fr of the values measured in both experiments. For the data set of 2012, the errors given in parentheses for the change in mean-square charge radius originate only from the experimental error of the isotope shift, while the errors given in curly braces are the total errors taking into account the theoretical uncertainties of the field and mass shift factors. For the data set of 2014, the experimental isotope shift error has two components: the first is denoted by $()_{\mathrm{stat}}$ and represents the error obtained for the isotope shift from the fitting procedure, while the second component denoted by $()_{\mathrm{sys}}$ is the systematic error originating from the ISCOOL voltage offset. These errors are individually propagated into the mean-square charge radius error and labeled in the same way. More details on these errors are given in the text.

Data set	$A(7s\ ^2S_{1/2})$ (MHz)	μ (μ_N)	$\delta\nu^{A,221}$ (MHz)	$\delta\langle r^2\rangle^{A,221}$ (fm^2)
2012	+6820(30)	+3.11(4)	+5590(100)	$-0.272(5)\{6\}$
2014	+6851(1)	+3.13(4)	$+5475(1)_{\mathrm{stat}}(20)_{\mathrm{sys}}$	$-0.26638(5)_{\mathrm{stat}}(97)_{\mathrm{sys}}\{300\}$

experimental isotope shift error of the high resolution data contains a statistical and a systematic component, with the statistical error labeled as $()_{\mathrm{stat}}$, which was obtained from the scatter of the fit results as was described in Sect. 4.1.3. The systematic error is labeled as $()_{\mathrm{sys}}$, and it originates from the uncertainty in the ISCOOL voltage as previously described. The statistical and systematic errors of the isotope shift are separately propagated into the error of the mean-square charge radius and labelled in the table.

The agreement is good for the magnetic dipole moment and change in mean-square charge radius relative to ^{221}Fr within the uncertainties reported in Article I [5]. The improvement in precision for the $A(7s\ ^2S_{1/2})$ value does not propagate to the magnetic dipole moment since this uncertainty is dominated by the uncertainty of the reference values used in Eq. 4.10. The improvement of the experimental error originating from the isotope shift of the mean-square charge radius is clear for the high-resolution results, even with the systematic uncertainty originating from ISCOOL. However, the total error of the charge radius is still dominated by the theoretical errors in determining the field and mass shift factors.

4.2.4 Quadrupole moment results

The spectroscopic quadrupole moment, introduced in Chapter 2, Sec. 2.3, can be calculated from the experimental $B(8p\ ^2P_{3/2})$ value by using

$$Q_s^{\mathrm{exp}} = \frac{B_{\mathrm{exp}}(8p\ ^2P_{3/2})}{B_{\mathrm{ref}}(8p\ ^2P_{3/2})Q_s^{\mathrm{ref}}}, \tag{4.23}$$

where the reference values are: $B_{\mathrm{ref}}(8p\ ^2P_{3/2})(^{221}\mathrm{Fr}) = -85.7(8)$ MHz [105], $Q_s^{\mathrm{ref}}(^{221}\mathrm{Fr}) = -1.00(1)$ eb [28]. The spectroscopic quadrupole moment is given in the unit of "eb", which is the elementary electron charge $e = 1.602176565(35) \times 10^{-19}$C multiplied by the "barn" unit $b = 10^{-28}$ m^2. Table 4.10 gives the extracted experimental value for ^{219}Fr along with the hyperfine structure parameters $A(8p\ ^2P_{3/2})$ (MHz) and $B(8p\ ^2P_{3/2})$ (MHz). The result for the spectroscopic quadrupole moment is discussed in detail in Chapter 5 Sec. 5.3, with a brief summary given in Article II, Appendix A.

Table 4.10: Experimental hyperfine structure results obtained from the high-resolution data of ^{219}Fr.

Isotope	$A(8p\ ^2P_{3/2})$ (MHz)	$B(8p\ ^2P_{3/2})$ (MHz)	Q_s^{exp} (eb)
^{219}Fr	+24.7(5)	−104(1)	−1.21(2)

Chapter 5

Discussion

This chapter is divided into two main topics. Firstly, Sect. 5.1 presents the various types of nuclear deformations observed in the francium isotopes, serving as an introduction to the physics discussion of the low-resolution results of Article I, given in Sect. 5.2. The second topic is the discussion of the high-resolution results in Sect. 5.3. The discussion starts by providing an extended description of the Coriolis interaction in nuclei which is subsequently used to provide an interpretation of the spectroscopic quadrupole moment of ^{219}Fr.

5.1 Nuclear shapes

This section will focus on the different types of nuclear deformations: the spherical nuclei around shell closures, the widely present quadrupole deformed nuclear shapes and the more localized octupole deformed shapes. This section serves as a general introduction of the concepts relevant to the physics discussion in Article I, Sect. 5.2.

5.1.1 Spherical shell model

As mentioned in Chapter 1, nuclei possessing a certain number of protons and neutrons $Z, N = 2, 8, 20, 28, 50, 82, 126$, also known as magic numbers, are more stable and generally have a spherical nuclear shape. The need to explain the occurrence of such numbers lead to the development of one of the most widely used nuclear structure models: the shell model. In its most basic form, this

model assumes that the motion of the protons and neutrons within the nucleus is only dependent on a spherically symmetric nuclear potential $V(r)$ in the form of a simple harmonic oscillator, whose energies are defined as [16]:

$$E_{nl} = (2n + l - \frac{1}{2})\hbar\omega, \tag{5.1}$$

where n is the radial quantum number and l the orbital angular momentum quantum number. This first order approximation produces the energy levels on the left hand side of Fig. 5.1.

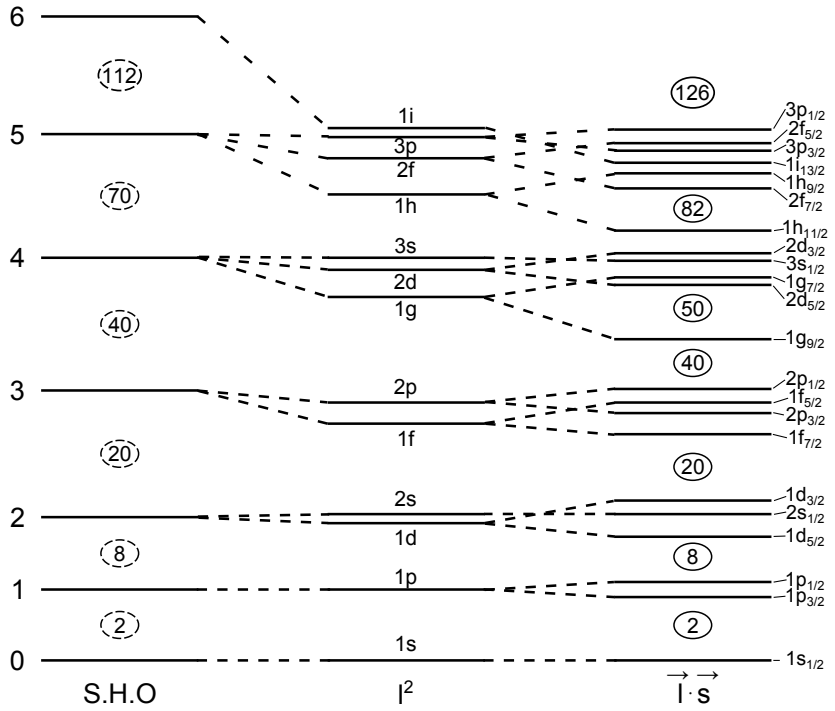

Figure 5.1: Nuclear energy levels predicted by the shell model with different levels of approximation: simple harmonic oscillator S.H.O, modified harmonic oscillator with a l^2 term, realistic shell model potential with both an l^2 term and $\vec{l} \cdot \vec{s}$ coupling. Figure adapted from [16].

The energy levels of the single nucleons obtained in this way will be degenerate since different combinations of n and l can give the same total $2n + l$ in Eq. 5.1. This degeneracy can be partly removed by introducing an l^2 term in the shell model Hamiltonian, corresponding to a more attractive nuclear

potential for nucleons at a larger radius r from the core and with the nuclear potential in the inner core being mostly constant. The addition of this term produces the levels in the middle of Fig. 5.1. The final addition to the model, necessary for reproducing the magic numbers as observed via experiments is the coupling of the orbital angular momentum l with the intrinsic spin s. The addition of this term splits the l levels into $l + s$ and $l - s$ levels, depending on their relative orientation. This produces significant gaps between the energy levels at the correct magic numbers of nucleons, as seen in the right hand side of Fig. 5.1. The great success of this model in reproducing the magic numbers is however limited by the fact that this model is in principle only suitable for isotopes which have a single nucleon or hole with respect to a closed shell. The model is thus suited mostly for spherical nuclei and their immediate neighbours, which are not too deformed. On the other hand, by adding a residual interaction between the valence nucleons, the effects induced by deformation can also be calculated in the shell model, provided a large enough model space can be used [119]. However, the region around lead where the francium isotopes are located would require a very large model space to be able to account all valence particles and such large scale shell model calculations are not currently possible. Therefore, a model starting from a deformed potential is the next best option to reproduce what is happening in nuclei with a large valence space. The following section introduces one such model: the Nilsson model.

5.1.2 Deformed Nilsson model

The model which is most often used for describing nuclei with quadrupole deformed nuclear shapes is the Nilsson model. The model assumes that a single valence nucleon is moving relative to the nucleus which has an either prolate or oblate shape. Thus the central potential is now assumed to be axially deformed, rather than spherical. These shapes were introduced in Chapter 2, Sec. 2.3 with the definition of the quadrupole moment. Figure 5.2 shows a valence nucleon moving relative to a prolate deformed core with an intrinsic deformation axis Z. Depending on the angle of the single particle angular momentum $\mathbf{j}$ with respect to Z, the particle will have a different projection K on this symmetry axis (a in Fig. 5.2). If the projection of K is low compared to $\mathbf{j}$ (b in Fig. 5.2), the vector $\mathbf{j}$ will point almost perpendicular to Z so that the particle will move around the bulk of the nuclear matter and thus have less energy (minimal energy is achieved when there is maximal overlap of nuclear matter). Conversely, if the projection K is high the particle will spend more time away from the bulk of the nuclear matter and have more energy since it will be less bound (c in Fig. 5.2). The difference in energy between the different couplings of the single particle momentum to the deformation axis will increase with increasing nuclear

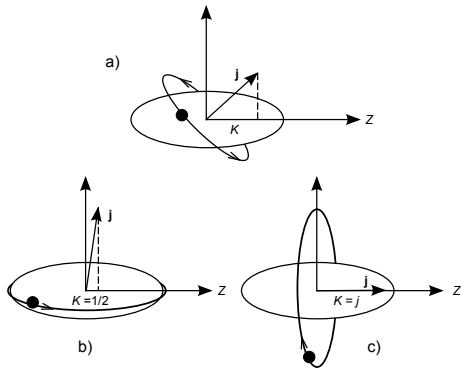

Figure 5.2: Valence nucleon moving outside of a prolate deformed core: a) general case, b) the projection K of the single particle angular momentum **j** is minimal, c) **j** is fully aligned with the deformation axis Z.

deformation. In the case of an oblate deformed nucleus, these effects would be inverted: then maximum overlap (and thus lowest energy) occurs when the single nucleon spin is aligned with the deformation axis.

This approach shows that the energy levels of states with a different K quantum number for a given **j** would be degenerate for a spherical nucleus as described by the shell model, but their degeneracy is lifted in the presence of nuclear deformations. Using this fact, along with the energy level spacings of the spherical shell model levels, together with the constraint that no two levels of the same K and parity may cross, the Nilsson model energy diagram as a function of quadrupole deformation can be constructed [16]. An example of such a diagram is given in Fig. 5.3 for the protons around the $Z = 82$ shell closure.

In general, the Nilsson levels are labeled as $K^{\pi}[Nn_z\Lambda]$, where π is the parity of the level defined as $(-1)^l$, N is the principal quantum number of the major shell, n_z is the number of nodes of the wave function along the deformation axis Z and Λ is the component of the orbital angular momentum along the Z axis. The projection K is related to Λ by $K = \Lambda + \Sigma$, where $\Sigma = \pm 1/2$ is the projection of the intrinsic nucleon spin on Z. As an example the $1/2^+[400]$ level in the bottom of Fig. 5.3 has $N = 4$ meaning that it belongs to the fourth major shell, with the wave function having zero nodes $n_z = 0$ along the Z axis (so originating from an s-orbit, so $l = 0$) and with $\Lambda = 0$ (so $K = \Sigma$). This level will play a role in the discussion of the ground state properties of the neutron-rich francium isotopes, both in Article I, Sect. 5.2 and in Sect. 5.3.

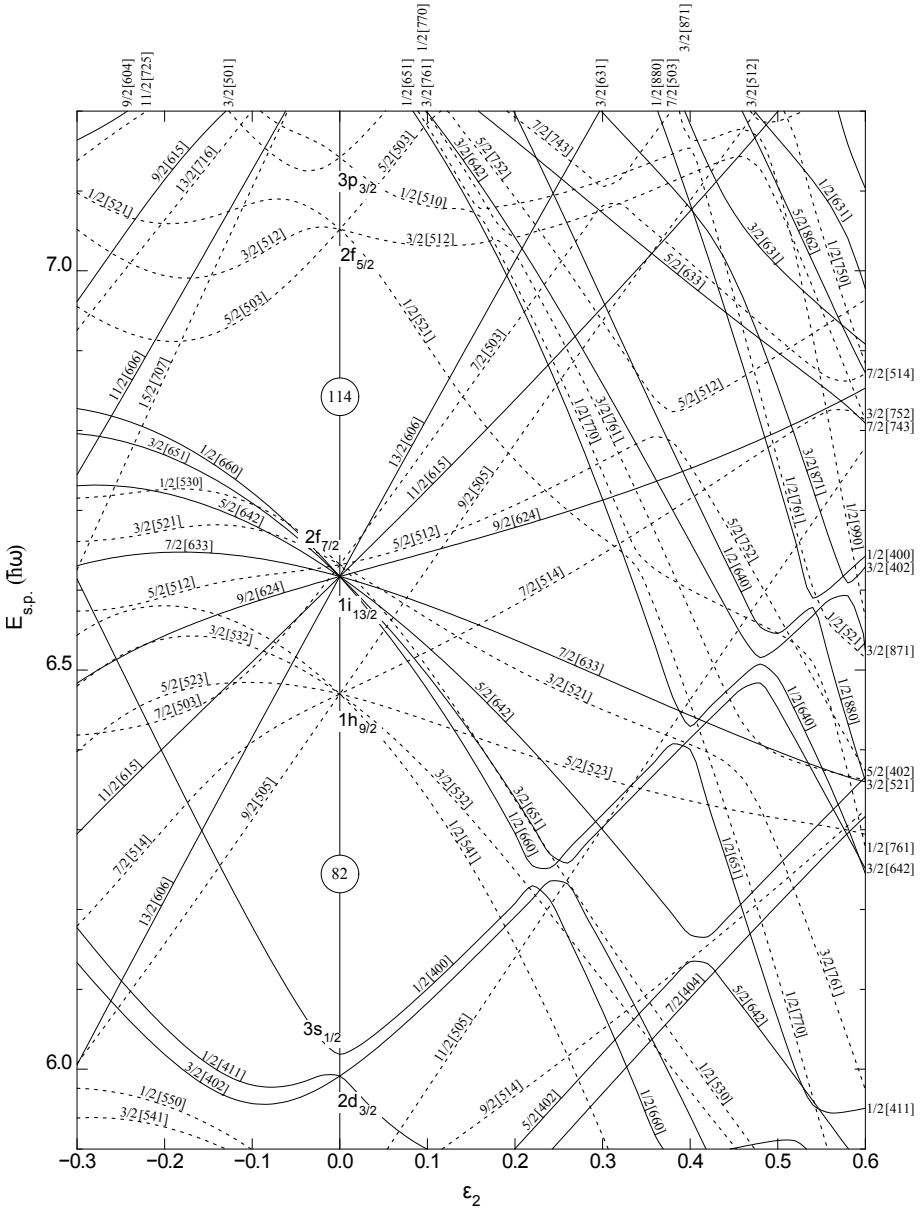

Figure 5.3: Nilsson diagram of single particle energy levels $E_{\text{s.p.}}$ of protons in function of the Nilsson quadrupole deformation parameter ϵ_2, where $\epsilon_2 > 0$ corresponds to prolate deformation and $\epsilon_2 < 0$ to oblate.

5.1.3 Octupole deformations

The reflection-asymmetric shapes arising from an octupole deformation of the nucleus, and the actinide region of the nuclear chart around francium where such shapes appear, have been introduced in Chapter 1. This section provides a description of these shapes, the conditions for their formation, predicted nuclear energy levels from a reflection-asymmetric model and experimental signatures of this particular type of deformation.

Reflection-asymmetric nuclear shapes

A general way of describing the nuclear surface is by a spherical harmonic multipole expansion of the nuclear radius vector $R(\theta, \phi)$ in terms of the deformation parameters $\alpha_{\lambda\mu}$ [17]:

$$R(\theta,\phi) = c(\alpha) R_0 \left[1 + \sum_{\lambda=2}^{\lambda_{\max}} \sum_{\mu=-\lambda}^{+\lambda} \alpha_{\lambda\mu} Y^*_{\lambda\mu}(\theta,\phi) \right], \tag{5.2}$$

where $c(\alpha)$ is determined from the nuclear volume conservation condition and R_0 was defined in Chapter 2, Eq. 2.15. If the nuclear deformation is axially symmetric with respect to the axis of deformation Z, then the deformation parameters with $\mu \neq 0$ vanish, leaving only the deformation parameters $\alpha_{\lambda 0}$, which are usually labeled as β_{λ}. Thus, in the case of axially symmetric deformations, the quadrupole deformation is described by the parameter β_2 and the octupole deformation by the parameter β_3. In the case that the deformation is not axially symmetric, the quadrupole deformation is described by the parameters β_2 and γ, which are related to α_{20}, α_{22} by [120]:

$$\alpha_{20} = \beta_2 \cos\gamma \tag{5.3a}$$

$$\alpha_{22} = \frac{1}{\sqrt{2}} \beta_2 \sin\gamma \tag{5.3b}$$

The octupole deformation in the general case of axially-asymmetric shapes is described by seven deformation parameters: $\alpha_{30} = \beta_3, \alpha_{3-1/1}, \alpha_{3-2/2}, \alpha_{3-3/3}$.

Conditions for a vibrational or stable reflection-asymmetric shape

One of the most characteristic features of the theoretical models describing reflection-asymmetric nuclear shapes is the inclusion of mixing between nuclear states of different parity. This mixing is caused by the parity-breaking odd-multipolarity octupole interaction. The strength of this interaction can be designated with the coupling constant κ_3, which is related to the matrix element of the octupole operator $\langle j||Q_3||j'\rangle$ and corresponding octupole vibrational excitations of the system $E_{\rm oct}$ by the relation given by Butler and Nazarewicz [17]:

$$\sum_{j,j'} \frac{\langle j||Q_3||j'\rangle^2 (u_j v_{j'} + u_{j'} v_j)^2 (E_j + E_{j'})}{(E_j + E_{j'})^2 - E_{\rm oct}^2} = \frac{7}{\kappa_3}, \tag{5.4}$$

where $E_j, E_{j'}$ are particle-hole energies and u_j, v_j are BCS (Bardeen, Cooper, Schrieffer) occupation coefficients [120]. In the BCS model, the nuclear ground state wave function is described in terms of particle-hole pair states (j,j') and the coefficients u_j^2 and v_j^2 represent the probabilities that such states will be occupied.

Equation 5.4 can be used to calculate the octupole vibrational energies $E_{\rm oct}$ for a given coupling constant κ_3, which then go into the calculation of the total nuclear energy as a function of the octupole deformation parameter β_3, giving the plots in Fig. 5.4, which were adapted from [17]. If κ_3 is small (a in Fig. 5.4), then the octupole vibration levels $E_{\rm oct}$ for $\beta_3 \neq 0$ will always be above the ground state, producing a minimum of the total energy at $\beta_3 = 0$. If the octupole coupling increases to the critical point $\kappa_{3,\rm crit}$ defined by

$$\kappa_{3,\rm crit} = 7 \left[\sum_{j,j'} \frac{\langle j||Q_3||j'\rangle^2 (u_j v_{j'} + u_{j'} v_j)^2}{E_j + E_{j'}} \right]^{-1}, \tag{5.5}$$

then the energy of the octupole vibration will become degenerate with the ground state $E_{\rm oct} = 0$ (b in Fig. 5.4). If κ_3 is increased further, the system will develop a stable octupole deformation with two distinct minima at $\pm\bar{\beta}_3$, separated by a potential barrier V_B (c in Fig. 5.4). In the case of $\kappa_3 \gg \kappa_{3\rm crit}$, a rigid static octupole deformation would develop, but this has so far not been observed.

Equation 5.5 shows that a necessary condition for the developement of low energy octupole collective states is the presence of energy orbitals which can be coupled through the octupole interaction near the Fermi level. The

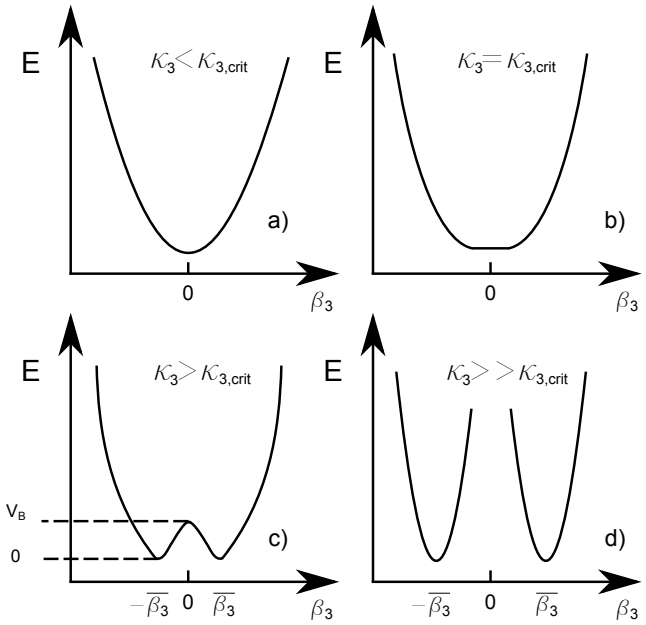

Figure 5.4: Total nuclear energy as a function of the octupole deformation β_3, for different values of κ_3, adapted from [17]. Case a) represents octupole vibrations when $\kappa_3 < \kappa_{3,\mathrm{crit}}$. In the case b) when $\kappa_3 = \kappa_{3,\mathrm{crit}}$, the octupole vibrational level is degenerate with the ground state. When $\kappa_3 > \kappa_{3,\mathrm{crit}}$ as in c), a stable octupole deformation develops in two minima at $\pm\bar{\beta}_3$, while in the case d) where $\kappa_3 \gg \kappa_{3,\mathrm{crit}}$, a completely rigid stable octupole deformation would develop.

octupole operator, defined by [17] $Q_3^+ = \sum_{jj'} \langle j|f_3(r)Y_{30}(\theta,\phi)|j'\rangle c_j^+ c_{j'}$ with $f_3(r)$ a radial form factor [121] and $c_j^+ c_{j'}$ coefficients related to the spherical shell model potential [17], is proportional to the Y_{30} term. This term will most strongly couple orbitals which differ by 3 units of l and j and which are of opposite parity. Thus the coupling will be strongest between a "normal" parity orbital from the current oscillator shell with an intruder "unique" parity orbital from the next major shell. These coupled orbitals are near the proton or neutron particle numbers 34 $(2p_{3/2} - 1g_{9/2})$, 56 $(2d_{5/2} - 1h_{11/2})$, 88 $(2f_{7/2} - 1i_{13/2})$ and 134 $(2g_{9/2} - 1j_{15/2})$, which are shown in Fig. 5.5.

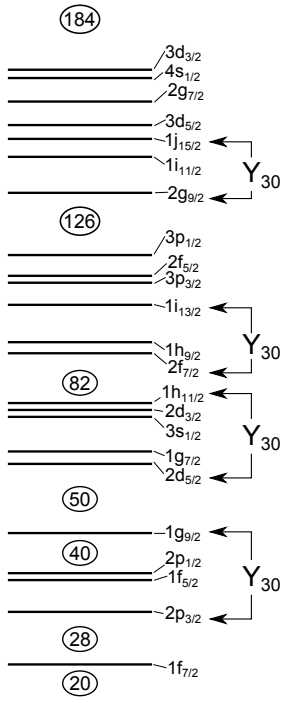

Figure 5.5: Figure showing the orbitals which are coupled by the octupole Y_{30} term, adapted from [17].

Reflection-asymmetric rotor model

A theoretical model used to describe odd-A nuclei possessing reflection-asymmetric shapes was developed by Leander and Chen [8] and used to reproduce the experimentally measured properties of the nuclei in the $A \sim 219 - 229$ mass region, including ^{221,223,225,227}Fr. The model assumes that the valence particle moves around a rotating core with an axially symmetric but reflection-asymmetric shape, characterized by the standard multipole expansion coefficients for the charge radius: $\beta_2, \beta_3, \beta_4, \beta_5, \beta_6$. As a consequence of the reflection-asymmetric shape of the nuclear potential, the model assumes that the resulting single particle orbits have mixed parity.

Figure 5.6 shows the single particle states obtained using this model. The left panel shows the pure parity states for a prolate deformation with $\beta_2 = 0 - 0.18$ and no octupole deformation, while the right hand side shows the parity mixed orbitals for $\beta_3 = 0 - 0.1$ for a constant $\beta_2 = 0.18$. Using this level scheme, the

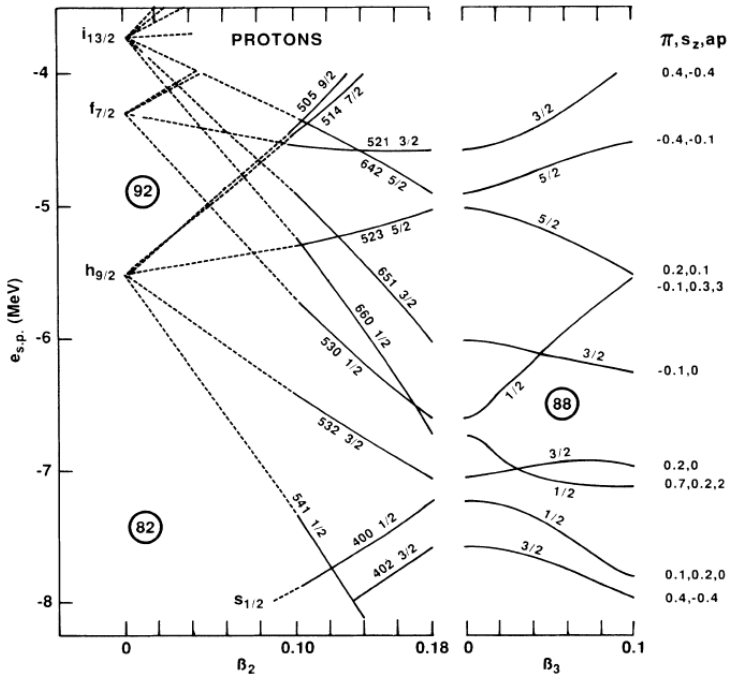

Figure 5.6: Single particle energy levels used in the reflection-asymmetric rotor model of Leander and Chen [8]. The left panel shows the energy levels of good parity with prolate deformation $\beta_2 = 0 - 0.18$ with the octupole deformation parameter $\beta_3 = 0$. The right panel shows the parity mixed levels which arise if the deformation parameter is varied as $\beta_3 = 0 - 0.1$ and the quadrupole deformation is held constant at $\beta_2 = 0.18$.

ground state spins, magnetic dipole moments and spectroscopic quadrupole moments of ^{221,223,225,227}Fr were qualitatively well reproduced by basing the calculations on the $1/2 - 0.7, 0.2, 2$ and $3/2 - 0.2, 0$ levels for $Z = 87$ with $\beta_3 \neq 0$ in Fig. 5.6. For more details the reader is referred to the paper of Leander and Chen [8].

Experimental signs of reflection asymmetry from charge radii

There exist several experimental signs of reflection-asymmetric nuclear shapes such as: the presence of rotational bands with same K but opposite parity which lie close in energy, the existence of alternating opposite parity states in rotational bands which are connected by enhanced E_1 transition rates, and others [17, 10].

This section focuses on the connection between results obtained from charge radii measurements and the presence of reflection-asymmetric shapes. An effect which is regularly observed in mean square charge radii values along an isotopic chain is the odd-even staggering of these values between isotopes with odd and even N. The odd-even staggering effect can be quantified using the factor $D(N; \delta \left\langle r^2 \right\rangle^{N,N_{\mathrm{ref}}})$[28]:

$$D(N;\delta\langle r^2\rangle^{N,N_{\mathrm{ref}}}) = (-1)^N \left[\delta\langle r^2\rangle^{N,N_{\mathrm{ref}}} - \frac{\delta\langle r^2\rangle^{(N-1),N_{\mathrm{ref}}} + \delta\langle r^2\rangle^{(N+1),N_{\mathrm{ref}}}}{2}\right]. \quad (5.6)$$

When calculating $D(N; \delta \left\langle r^2 \right\rangle^{N,N_{\mathrm{ref}}})$ for an isotopic series, it follows that the mean square charge radius $\left\langle r^2 \right\rangle$ for isotopes with odd N is smaller than the average of the even-N neighbours, for most of the studied isotopic chains in the nuclear chart [46, 17]. One explanation for this difference is that even nuclei experience larger quadrupole vibrational deformations due to pairing effects which are reduced in odd nuclei by blocking [46], leading to smaller values of $\left\langle r^2 \right\rangle$ for odd-N isotopes.

The connection between this odd-even staggering effect in the charge radii and reflection-asymmetric shapes, lies in the observed inversion of this staggering in the radium, radon and francium isotopes in the region around $N = 135$ [31, 30, 29]. Here the $\left\langle r^2 \right\rangle$ of odd-N isotopes is larger than the average of their even-N neighbours (Figure 61. in [46]). One possible explanation for this reversal is that the octupole deformation is larger in odd-N isotopes [122], since the unpaired particle polarizes the quadrupole-octupole deformed core towards a more stable octupole deformation [31]. The result is an increased $\left\langle r^2 \right\rangle$ in odd-N nuclei compared to their even-N neighbours. The claim for a larger octupole deformation in odd-N isotopes is supported by the fact that the energy splitting of parity doublets has been experimentally observed to be smaller in such isotopes compared to their even-N neighbours [17].

Since francium has an odd number of protons ($Z = 87$), the francium isotopes with odd N will have an odd neutron and odd proton as valence particles. The presence of two odd particles is predicted to further polarize the nucleus towards reflection-asymmetric deformation, leading to even smaller parity doublet splittings [11] as were measured for ^{224}Ac [123] (with $Z = 89$). This agrees with the increase of $\left\langle r^2 \right\rangle$ for the odd-odd francium isotopes compared to their odd-even neighbours in the region of reflection-asymmetric shapes. The following section presents Article I which shows the new mean-square charge

radii results obtained as part of this PhD work for ^{218m,219,229,231}Fr, as well as their nuclear g factors, and their interpretation in light of the previous discussion.

5.2 Article I

This article presents the results of the spin, magnetic dipole moments (and related g factors) and changes in mean-square charge radii of the ^{218m,219,229,231}Fr isotopes. The spins of the odd-A francium isotopes were known before and have been confirmed in this work. The spin of the ^{218m}Fr isomeric state is not yet known, and could also in this work not be determined. The g factor value of ^{219}Fr is very similar to the values of the more deformed ^{221,223,225}Fr isotopes and points to an occupation of the $\pi 1h_{9/2}$ orbital by the unpaired valence proton(s). The g-factor values of the ^{229,231}Fr agree with the occupation of the intruder $\pi 3s^{-1}_{1/2}$ orbital, also observed to be the ground state in ^{227}Fr. The discussion of the charge radii odd-even staggering value determined for ^{220}Fr agrees with this isotope being in a transitional region where octupole correlations are still present but diminishing, while the value for ^{228}Fr indicates that this isotope lies outside the region of reflection asymmetry.

The article was entirely written by me, after I made the full analysis. The half-life of ^{218m}Fr was originally determined from the analysis by Kara Lynch, and was confirmed later by my own analysis. During the submission process I modified the article based on comments and suggestions from the collaboration and the referees.

Physical Review C 90, 014317 (2014)

Laser spectroscopy of francium isotopes at the borders of the region of reflection asymmetry

I. Budinčević,[1,*] J. Billowes,[2] M. L. Bissell,[1] T. E. Cocolios,[2] R. P. de Groote,[1] S. De Schepper,[1] V. N. Fedosseev,[3] K. T. Flanagan,[2] S. Franchoo,[4] R. F. Garcia Ruiz,[1] H. Heylen,[1] K. M. Lynch,[1,2,5] B. A. Marsh,[3] G. Neyens,[1] T. J. Procter,[2,†] R. E. Rossel,[3,6] S. Rothe,[3] I. Strashnov,[2] H. H. Stroke,[7] and K. D. A. Wendt[6]

[1]*KU Leuven, Instituut voor Kern- en Stralingsfysica, B-3001 Leuven, Belgium*

[2]*School of Physics and Astronomy, The University of Manchester, Manchester M13 9PL, UK*

[3]*Engineering Department, CERN, CH-1211 Geneva 23, Switzerland*

[4]*Institut de Physique Nucléaire d'Orsay, F-91406 Orsay, France*

[5]*Physics Department, CERN, CH-1211 Geneva 23, Switzerland*

[6]*Institut für Physik, Johannes Gutenberg-Universität, D-55128 Mainz, Germany*

[7]*Department of Physics, New York University, New York, New York 10003, USA*

(Dated: September 4, 2015)

Abstract

The magnetic dipole moments and changes in mean-square charge radii of the neutron-rich ^{218m,219,229,231}Fr isotopes were measured with the newly-installed Collinear Resonance Ionization Spectroscopy (CRIS) beam line at ISOLDE, CERN, probing the $7s\ ^2S_{1/2}$ to $8p\ ^2P_{3/2}$ atomic transition. The $\delta\langle r^2\rangle^{A,221}$ values for ^{218m,219}Fr and ^{229,231}Fr follow the observed increasing slope of the charge radii beyond $N = 126$. The charge radii odd-even staggering in this neutron-rich region is discussed, showing that ^{220}Fr has a weakly inverted odd-even staggering while ^{228}Fr has normal staggering. This suggests that both isotopes reside at the borders of a region of inverted staggering, which has been associated with reflection-asymmetric shapes. The $g(^{219}\text{Fr}) = +0.69(1)$ value supports a $\pi 1h_{9/2}$ shell model configuration for the ground state. The $g(^{229,231}\text{Fr})$ values support the tentative $I^\pi(^{229,231}\text{Fr}) = (1/2^+)$ spin, and point to a $\pi s_{1/2}^{-1}$ intruder ground state configuration.

PACS numbers: 21.10.Ky, 21.10.Hw, 21.10.Pc, 27.80.+w, 27.90.+b

* ivan.budincevic@fys.kuleuven.be

† Present address: TRIUMF, Vancouver, British Columbia V6T 2A3, Canada.

I. INTRODUCTION

Nuclei possessing reflection-asymmetric shapes have attracted much theoretical and experimental attention ([1] and references therein), even reaching the wider scientific community [2]. These nuclei are located in a narrow region of the nuclear chart centered approximately around $^{225}_{89}$Ac [3]. The neutron-rich $^{220-228}_{87}$Fr isotopes located in this vicinity have already been studied with laser spectroscopy [4, 5] and decay spectroscopy [6–17], but there has been no clear agreement on the presence of stable octupole deformations in these nuclei. For example the ground-state spin-parities of the odd-odd $^{220-228}$Fr isotopes, measured by collinear laser spectroscopy and magnetic resonance [4], were reproduced by Sheline et al. [18] using a folded Yukawa octupole deformed model [19] with an octupole deformation parameter value $\epsilon_3 = +0.08$. However, Ekström et al. [20] reproduced the experimental spin values and qualitatively reproduced the magnetic dipole and spectroscopic quadrupole moment values for ^{224,226,228}Fr, using the core-quasiparticle model [21], including only quadrupole and hexadecapole deformations. Many of the $A \geq 213$ francium isotopes exhibit certain experimental signs of reflection-asymmetric nuclear shapes [1], such as the presence of parity doublet decay bands connected by enhanced E1 transitions, as in $^{217-223,225,227}$Fr[8, 10–12, 14–16, 22]. Another effect that has been related to the presence of reflection-asymmetric shapes is the inversion of the mean-square charge radius odd-even staggering order, as seen in the francium, radium and radon isotopes around $N = 136$ [23–25]. This effect has been described by Otten [26], interpreting it as corroborating the calculations by Leander and Sheline [19], which suggest that octupole deformations should be more pronounced in odd than in even nuclei. Otten also notes that the calculations by Talmi [27] imply a regular odd-even staggering for even multipole deformations and inverted odd-even staggering for odd multipole deformations.

In this article, we report on experimental results from collinear laser spectroscopy performed for the first time on the isotopes ^{218m,219,229,231}Fr, at the borders of the region of reflection asymmetry, using the new Collinear Resonance Ionization Spectroscopy (CRIS) beamline [28, 29]. Measurements of the neutron-deficient isotopes of francium, down to ^{202}Fr, were performed during the same experiment and have recently been published [28, 30]. In the previous collinear laser spectroscopy study [4], the ^{218m,219}Fr isotopes could not be stud-

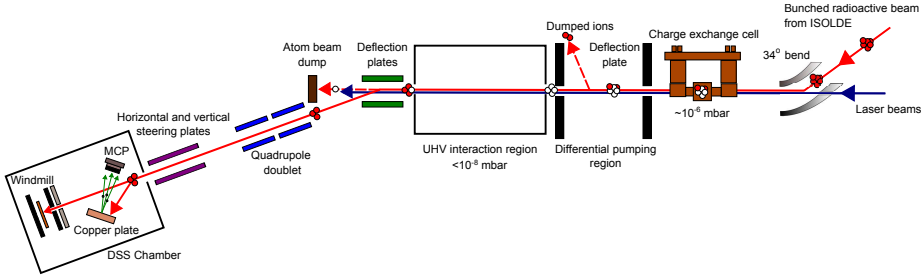

FIG. 1. (Color on-line) Schematic drawing of the CRIS beam line.

ied due to their low production yield and short half-lives $t_{1/2}(^{218m}\mathrm{Fr}) = 22.0(5)$ ms [31], $t_{1/2}(^{219}\mathrm{Fr}) = 20(2)$ ms [32].

II. EXPERIMENTAL SETUP

The francium isotopes of interest were produced at the ISOLDE facility in CERN, by impinging 1.4 GeV protons on a thick UC_x target. These collisions produced the radioactive atoms of interest via spallation. The atoms diffused out of the target to a thin transfer tube, heated to $\sim$ 2400°C to facilitate diffusion. Surface-ionized francium ions were then accelerated to 50 keV and mass separated by the HRS high resolution mass separator, before being sent to the ISCOOL gas-filled segmented linear Paul trap [33, 34]. The ability to bunch the beam overcomes losses associated with the duty cycle of the pulsed lasers, which previously reduced the effectiveness of the method [35]. Using ISCOOL the ions can be bunched and the time of their release from the trap synchronized with the laser-system duty cycle, thus increasing the experimental efficiency by several orders of magnitude (a production-to-detection efficiency of 1% was measured for ^{202}Fr [28]). The ion bunches leaving ISCOOL were reaccelerated to 50 keV and deflected to the CRIS beam line, schematically shown in Fig. 1.

The ion bunch was passed through a charge exchange cell filled with potassium vapour held at 150 °C. During the experimental run, the potassium vapor produced a background pressure of 10^{-6} mbar in the charge exchange cell region, while neutralizing the ion bunches via collisional charge exchange with a neutralization efficiency of 50 %. Deflection plates

were placed after the charge exchange cell for deflection of non-neutralized ions. After the charge exchange cell, the atomic bunch passed through a differential pumping section before arriving at the interaction region where it interacts with the laser light. The ionization scheme used the $7s\ ^2S_{1/2} - 8p\ ^2P_{3/2}$ transition at 23658.306 cm^{-1}(422.7 nm) to measure the hyperfine structure and a 1064-nm nonresonant step to excite the atoms beyond the ionization threshold. The 422.7-nm transition was excited by frequency-doubled laser light from the RILIS 10 kHz Ti:Sa laser [36], transported to the CRIS beam line via a 35-m optical fibre. The laser had a tunable frequency range of $\pm$100 GHz for scanning over the hyperfine structure, with a frequency stability of $<$ 100MHz and a linewidth of around 1.5 GHz. The 1064 nm laser light was produced by a 30 Hz Nd:YAG laser (Spectra-Physics Quanta-ray) situated near the CRIS beam line. The two laser pulses and the ion bunch from ISCOOL were synchronized to overlap in the interaction region. This was done using a Quantum Composers digital delay generator (Model: QC9258), with the 422.7-nm laser pulse serving as the master trigger. The pressure within the interaction region was kept below 8×10^{-9} mbar to keep the background (originating from collisional ionization) to a minimum. The experimentally observed collisional reionization efficiency was on the order of 0.001 %. After resonance ionization of the atomic bunch, the ions were deflected to a biased copper plate ($-$600 V), where secondary electrons were emitted upon the ion impact and guided via an electrostatic-field gradient to a micro-channel plate (MCP) detector [37]. A LeCroy WavePro 725 Zi 2.5 GHz bandwidth oscilloscope was used to detect the ion signal with a time window around the ion arrival time of 10 μs. During the experiment α-decay energy spectra were collected in separate measurements by implanting the ions in a carbon foil mounted in the decay spectroscopy station (DSS), around which a dedicated α-decay spectroscopy setup [30, 37, 38] detects emitted α-particles.

III. RESULTS

Information about the magnetic dipole moment and changes in mean-square charge radii was obtained from the hyperfine spectra. From initial fitting of the hyperfine structure peaks with Voigt profiles, it was established that the resonance line shapes were fully dominated by a Gaussian profile, originating from the linewidth of the 422.7 nm RILIS Ti:Sa laser.

The hyperfine structure resonance spectra were fit with a χ^2-minimization routine, with the same full width at half-maximum for all peaks, free intensity ratios and their positions related by the hyperfine splitting energy

$$E_F = \frac{1}{2}A(F(F+1) - I(I+1) - J(J+1)), \tag{1}$$

where $|I-J| \leq F \leq I+J$. The A value is related to the magnetic dipole moment by $A = \mu_I B_e(0)/IJ$, where $B_e(0)$ is the magnetic field of the atomic electrons at the site of the nucleus. Due to the linewidth of 1.5 GHz in this initial experimental campaign only being able to resolve the lower-state splitting, the data did not provide any information on the nuclear spin. Therefore the spin I has been taken from literature assignments based on decay-spectroscopy data [7, 17, 31, 39, 40], and the related A values extracted from the data. The upper state splitting $A(8p\ ^2P_{3/2})$ was not resolved, as illustrated for ^{221}Fr in Fig. 2. The ratio $A(8p\ ^2P_{3/2})/A(7s\ ^2S_{1/2}) = +0.0036$ for ^{221}Fr [5], was kept constant for all isotopes, neglecting the hyperfine anomaly staggering which is less than 1 % of this ratio [41]. The magnetic dipole moments of ^{218m,219,229,231}Fr were evaluated relative to ^{210}Fr: $A_{\rm ref}(7s\ ^2S_{1/2})(^{210}{\rm Fr}) = +7195.1(4)$ MHz [4], $I^{\pi}_{\rm ref}(^{210}{\rm Fr}) = 6^+$ [42] , and $\mu_{\rm ref}(^{210}{\rm Fr}) = +4.38(5)\ \mu_N$ [43], using the formula

$$\mu_{\rm exp} = \frac{A_{\rm exp}(7s\ ^2S_{1/2})I_{\rm exp}\mu_{\rm ref}}{A_{\rm ref}(7s\ ^2S_{1/2})I_{\rm ref}}. \tag{2}$$

The results for $A(7s\ ^2S_{1/2})$ and μ for the spins proposed in the literature are given in Table I. In Fig. 3, the fitted hyperfine spectra are shown for the newly measured ^{218m,219,229,231}Fr isotopes, as well as for the reference isotopes ^{220,221}Fr. A minimum error of 30 MHz for $A(7s\ ^2S_{1/2})$ originates from the scatter observed in 18 hyperfine spectra measured throughout the experimental run for the reference isotope ^{221}Fr, as shown in Fig. 4. For the full discussion on this error, the reader is referred to Ref. [29, 44]. The largest contribution to the error on the extracted magnetic moments is introduced by the error on the reference magnetic moment of ^{210}Fr.

The isotope shifts $\delta\nu^{A,A^{\rm ref}}$ were determined from the fitted centre-of-gravity of the hyperfine spectra relative to ^{221}Fr. For the isotope shift, a minimum error of 100 MHz was established based on the long-term drift and short-term fluctuations of the centroid fre-

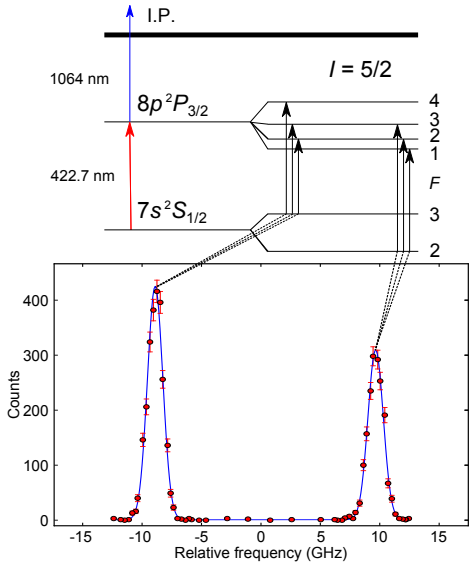

FIG. 2. (Color on-line) Example hyperfine spectrum of ^{221}Fr. The $8p\ ^2P_{3/2}$ splitting is unresolved and the $7s\ ^2S_{1/2}$ splitting is extracted from the distance between the two peaks according to equation 1.

quency of ^{221}Fr (a full discussion on this error is available in Ref. [44]). The change in nuclear mean-square charge radii can be extracted from the isotope shifts, via

$$\delta\langle r^2\rangle^{A,A^{\rm ref}} = \frac{\delta\nu^{A,A^{\rm ref}} - \frac{A-A^{\rm ref}}{A\cdot A^{\rm ref}}\cdot(K_{NMS}+K_{SMS})}{F}, \tag{3}$$

where F is the field shift, K_{NMS} the normal mass shift and K_{SMS} the specific mass shift constant [45]. The atomic masses A and $A^{\rm ref}$ are taken from [46]. The field and mass shift constants depend on the optical transition and in the case of francium have to be calculated theoretically, as in Ref. [45] for the francium D_2 line (7s $^2S_{1/2}$-7p $^2P_{3/2}$). These constants for the D_2' line (7s $^2S_{1/2}$-8p $^2P_{3/2}$), studied in this experiment, could then be determined relative to the calculated values via a King plot [47]. The details of this analysis can be found in [30]. The values extracted using the King-plot method and the formula $K_{NMS} = \nu_{\rm exp}/1822.888$ [45] were $F_{D2'} = -20670(210)$ MHz/fm^2, $K_{SMS}^{D2'} = 360(330)$ GHz u, and $K_{NMS}^{D2'} = 389$ GHz u. Substituting these values into Eq. 3 yielded the $\delta\langle r^2\rangle^{A,221}$ values

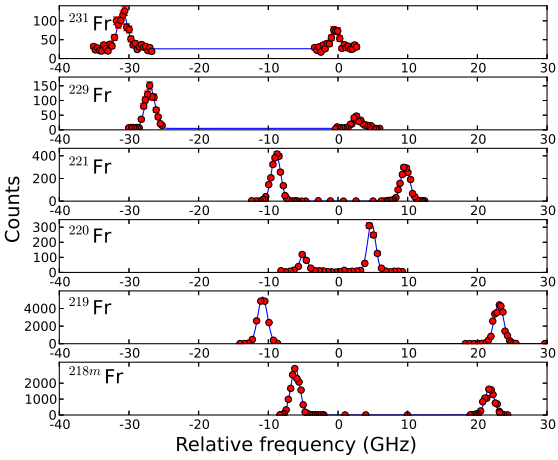

FIG. 3. (Color on-line) Fitted hyperfine spectra for the newly measured ^{218m,219,229,231}Fr isotopes and reference isotopes ^{220,221}Fr .

given in Table II along with their isotope shifts and assumed spins. The charge radii of ^{229,231}Fr were calculated assuming spins of 1/2 (see Section IV B). For ^{218m}Fr a spin of 9 is preferred, based on an in-beam spectroscopy study feeding levels in ^{218}Fr that decay to this low lying isomer [10], which is suggested to be the fully aligned member of the $\pi(h_{9/2}) \otimes \nu(g_{9/2})$ multiplet. However, determining the charge radius using the other spin

TABLE I. Extracted hyperfine parameters $A(7s\ ^2S_{1/2})$ and magnetic dipole moments μ, along with spins from literature.

Isotope	I^π	$A(7s\ ^2S_{1/2})$ (GHz)	$\mu_{\rm exp}(\mu_N)$
^{218m}Fr	(8^-) [39]	+3.30(3)	+2.68(4)
	(9^-) [10, 31]	+2.95(3)	+2.70(4)
^{219}Fr	$9/2^-$ [7]	+6.82(3)	+3.11(4)
^{229}Fr	$(1/2^+)$ [40]	+30.08(11)	+1.53(2)
^{231}Fr	$(1/2^+)$ [17]	+30.77(13)	+1.56(2)

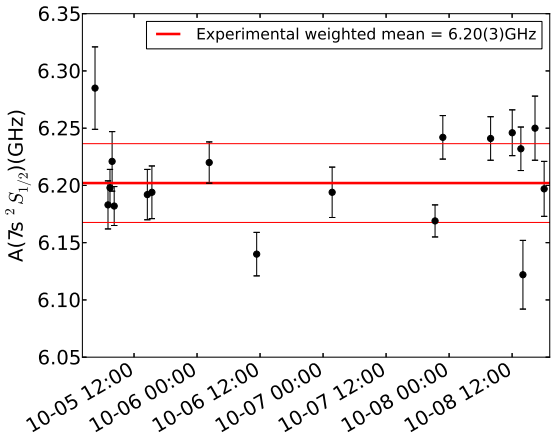

FIG. 4. (Color on-line) Plot showing the scatter of the $A(7s\ ^2S_{1/2})$ values extracted from 18 hyperfine spectra of the reference ^{221}Fr isotope taken throughout the experiment.

option of 8 [39], does not lead to a significantly different value within error bars. The errors given in Table II for $\delta\langle r^2\rangle^{A,221}$ are the uncertainties originating from the experimental isotope shift given in parentheses and the total error taking into account the theoretical errors for the field and mass shift values [45], given in curly braces.

TABLE II. Extracted isotope shifts $\delta\nu^{A,221}$ and changes in mean-square charge radii $\delta\langle r^2\rangle^{A,221}$, along with spins from literature. For $\delta\langle r^2\rangle^{A,221}$, the values in parentheses are the experimental uncertainties in determining the isotope shifts, while the values given in curly braces represent the total error taking into account the theoretical errors for the field and mass shift values [45].

Isotope	I^π	$\delta\nu^{A,221}$ (GHz)	$\delta\langle r^2\rangle^{A,221}$ (fm^2)
^{218m}Fr	(9^-) [39]	+8.24(10)	-0.401(5){6}
^{219}Fr	$9/2^-$ [7]	+5.59(10)	-0.272(5){6}
^{229}Fr	$(1/2^+)$ [40]	-18.36(10)	+0.894(5){11}
^{231}Fr	$(1/2^+)$ [17]	-22.14(10)	+1.078(5){12}

IV. DISCUSSION

A. Determination of the state in ^{218m}Fr

For ^{218}Fr it is important to determine whether the measured hyperfine spectrum originates from the isomeric state or from the ground state. The isomeric state has a lifetime of 22.0(5) ms [31], while the ground state has a lifetime of 1.0(6) ms [48]. Since the ion trapping time in ISCOOL was 32 ms in this experimental run, almost all of the ^{218}Fr ground state ions decayed before reaching the laser-ion interaction region. However, the release of the ion bunch from ISCOOL was not synchronized with the proton pulse. This means it is still possible that some ^{218}Fr ground state ions reached the trap if a proton pulse arrived within 5 ms of the trap release trigger.

Figure 5 shows the α-decay energy spectrum measured with the DSS upon implanting the non-neutralized component of the ^{218}Fr beam into a carbon foil, with a collection time of 5 minutes. The most intense α-decay branches observed by Ewan et al. and Sheline et al. [31, 39] (Table 1 and 2 in [31] and Fig. 4a,4b and 4d in [39]) are observed here: 7240 keV, 7616 keV, 7657 keV, 7681 keV, and 7952 keV originating from ^{218m}Fr and 8782 keV originating from ^{214m}At. The vertical arrow in Fig. 5 marks the location of the most intense α-decay branch of the ^{218}Fr ground state 7866 keV($I^{\alpha} = 92\%$) [39].

A dedicated half-life measurement was not made in this experimental run for ^{218}Fr, however the α-decay event timestamp information could be used to estimate the half-life. The individual timestamps were used to create a saturation/decay curve for the full ^{218}Fr beam, shown in Fig. 6. The spectrum was obtained by setting the time of the proton impact on the ISOLDE target as t_0 and plotting the time taken for an α-particle to be detected. A $6500 - 9500$ keV energy gate was applied to the spectrum to only include α-particles originating from ^{218m}Fr and ^{214m}At. Since the half-life of ^{214m}At is 760(15) ns [31], its decay can be considered virtually instantaneous, and thus the time of detection of a ^{214m}At α-particle solely depends on the half-life of its parent ^{218m}Fr. Fitting the decaying part of the curve in Fig. 6, yielded the half-life value: $t_{1/2}(^{218m}\text{Fr}) = 21(2)$ ms. The value $\chi^2_{\text{red}} = 1.59$ from the fit was used to scale up the final uncertainty. The extracted half-life value is in agreement with literature [31], confirming that the measured hyperfine spectrum belongs to the isomeric state ^{218m}Fr.

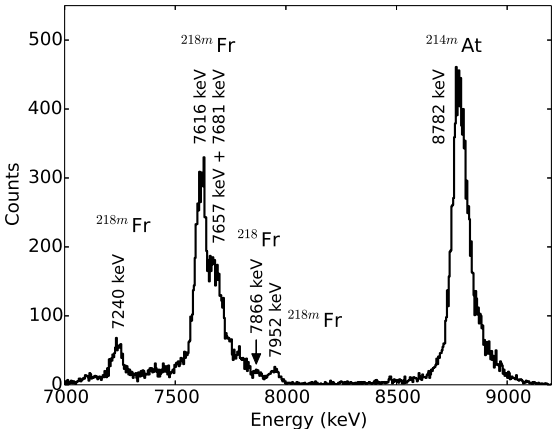

FIG. 5. α-particle energy spectrum of ^{218m}Fr. The most intense α-decay branches of ^{218m}Fr and ^{214m}At observed by Ewan et al. and Sheline et al. [31, 39] are labelled. The vertical arrow indicates the energy of the most intense branch of the ground state ^{218}Fr [39].

B. Magnetic dipole moments

The extracted experimental magnetic dipole moments and g-factors are shown in Fig. 7. The ground-state spin of the odd-A francium isotopes changes with increasing neutron number from $I(^{219}\mathrm{Fr}) = 9/2$ [7] to $I(^{227}\mathrm{Fr}) = 1/2$ [4]. This is reflected in the magnetic dipole moment values in Fig. 7 (upper panel), while the g-factors (lower panel) remain constant near an effective single particle value. The effective-proton single-particle g-factors for the $\pi 1h_{9/2}$ and $\pi 3s_{1/2}$ orbits are shown, calculated with $g_s^{\mathrm{eff}} = 0.6\ g_s^{\mathrm{free}}$ (typical for this region [20]) and $g_l = g_l^{\mathrm{free}}$. These effective values are consistent with numerically calculated single particle magnetic dipole moment values of odd-mass nuclei around ^{208}Pb, taking into account mesonic and renormalization corrections as well as core polarization effects [49]. Our experimental $g(^{219}\mathrm{Fr}) = +0.69(1)$ value indicates that the ^{219}Fr ground-state wave-function is dominated by an unpaired proton in the $\pi 1h_{9/2}$ orbital, as is the case for the odd-A francium isotopes up to ^{225}Fr. The g-factors of these neutron-rich isotopes are systematically lower than those of the neutron-deficient ^{207,209,211,213}Fr isotopes. The latter isotopes, near magic $N = 126$, have a nearly spherical ground state [20], while the neutron-rich isotopes are known to have a deformation larger than $\epsilon_2 > 0.15$ [20] (where ϵ_2 is the Nillson model

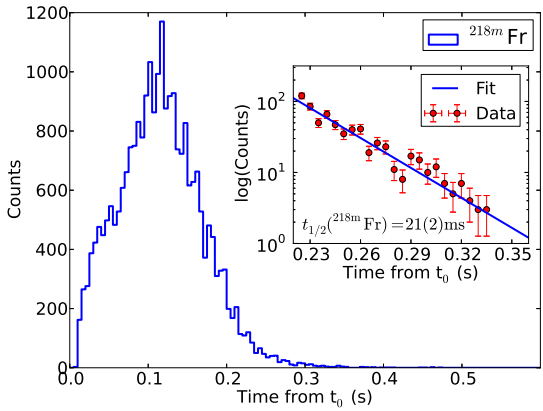

FIG. 6. (Color on-line) Saturation/decay curve of the full ^{218}Fr beam. The x axis shows the time stamp of the detected α-particles after the proton impact on target t_0. The inset shows the fit of the half-life on the exponential of the decay curve.

quadrupole deformation parameter) and exhibit parity doublet bands [11] associated with octupole deformations. These deformations have however only little impact on the g-factors because the Nilsson levels are straight lines (they do not mix with other shell model levels).

From ^{227}Fr onwards the structure of the ground state changes. The spin of ^{227}Fr was measured to be $I = 1/2$ using the RF-resonance technique in combination with collinear laser spectroscopy [4]. The g-factor of this state, extracted from the measured magnetic moment $\mu(^{227}\mathrm{Fr}) = 1.50(3)\ \mu_N$ [4], is in good agreement with the effective g-factor for a proton hole in the $\pi 3s_{1/2}$ orbit (Fig. 7). This suggests that the ground-state wave-function of ^{227}Fr is dominated by a proton-intruder configuration. Based on core-quasiparticle calculations including only quadrupole and hexadecapole deformations [20], the ground states of both ^{227}Fr and ^{228}Fr are found to be dominated by a proton hole in the $\pi 3s_{1/2}$ orbital (1/2[400] orbit). The spin and magnetic dipole moment for ^{227}Fr could also be reproduced by the reflection-asymmetric rotor model [50], with 1/2[400] as the dominant component of the wave-function, assuming that the octupole deformation parameter is $\beta_3 = 0$ (where β_3 is the octupole deformation parameter expressed in the spherical harmonics expansion). The main factor determining the level ordering in the reflection-asymmetric rotor model is the quadrupole deformation parameter, which increases for francium with increasing neutron

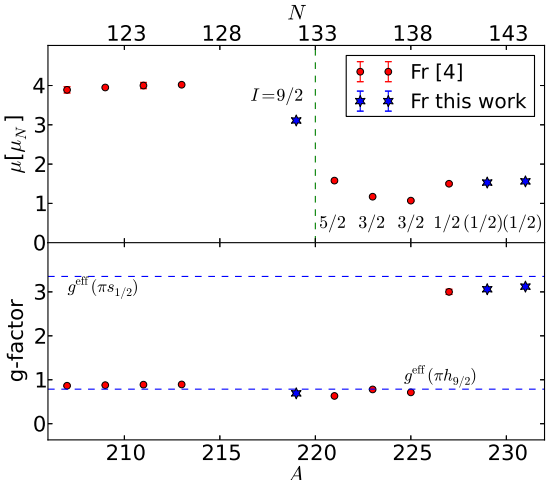

FIG. 7. (Color on-line) Magnetic dipole moments (upper panel) along with nuclear spins, and g-factors (lower panel) for ^{219,229,231}Fr, together with literature values for the neighbouring odd-even francium isotopes from Ref. [4]. The $g^{\rm eff}(s_{1/2})$ values were calculated using $g_s^{\rm eff} = 0.6\ g_s^{\rm free}$ and $g_l = g_l^{\rm free}$. The vertical dashed line (upper panel) emphasizes where the spin changes from $I = 9/2$ to the sequence 5/2, 3/2, 3/2, 1/2, (1/2), (1/2).

number [24]. The trend of increasing values of the quadrupole moment and β_2-deformation parameter with increasing neutron number has also been observed in the thorium ($Z = 90$) and uranium ($Z = 92$) isotopes [51]. The ground-state spin of ^{229}Fr was also tentatively assigned to be $I = (1/2)$ [40], arguing that it should be the same as for ^{227}Fr unless the quadrupole deformation of ^{229}Fr would be significantly smaller than ^{227}Fr and the octupole deformation significantly larger, both being unlikely. The spin of ^{231}Fr is tentatively assigned as (1/2) based on a characteristic $\beta-$decay pattern between the 1/2[400] and 1/2[501] Nilsson configurations observed in the vicinity of ^{231}Ra [17].

Our experimental $g(^{229}\text{Fr}) = +3.06(4)$ and $g(^{231}\text{Fr}) = +3.12(4)$ values (Fig. 7) are indeed consistent with a proton hole in the $\pi 3s_{1/2}$ orbital (the 1/2[400] orbit), as was proposed in [20] for ^{227,228}Fr. The ^{227,229,231}Fr g-factors also agree with the g-factors of the odd Tl isotopes, which have a hole in the $\pi 3s_{1/2}$ orbit (illustrated in Fig. 8). On the neutron-rich side ($N > 140$), the $\pi 3s_{1/2}$ 1/2[400] intruder state has been assigned to the ground states of

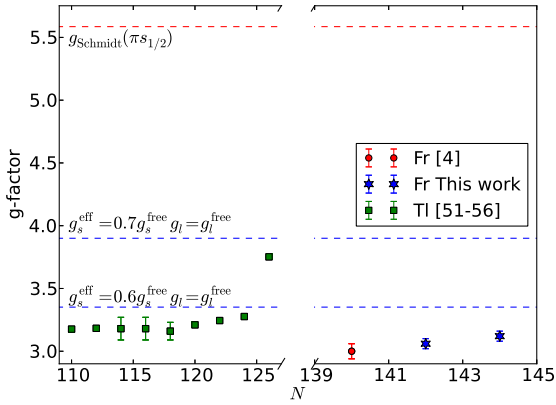

FIG. 8. (Color on-line) Comparison of ^{227,229,231}Fr and odd-A $^{191-207}$Tl g-factors. The data for francium were taken from Ref. [4] and this work, while the thallium data is from Refs. [52–57]. The $g^{\mathrm{eff}}(s_{1/2})$ values were calculated using $g_s^{\mathrm{eff}} = 0.6\ g_s^{\mathrm{free}}, g_l = g_l^{\mathrm{free}}$ and $g_s^{\mathrm{eff}} = 0.7\ g_s^{\mathrm{free}}, g_l = g_l^{\mathrm{free}}$.

^{231}Ac and ^{237}Pa [58]. Assuming the same behaviour for the increase of quadrupole moment and quadrupole deformation parameter with increasing mass as previously mentioned for thorium and uranium, the authors in Ref. [58] comment that as a hole state, the 1/2 [400] excitation energy decreases with increasing ϵ_2 and with increasing mass, for the actinium ($Z = 89$) and protoactinium ($Z = 91$) isotopes (Fig. 3 in [58]). It is reasonable to assume a similar behaviour of this level in francium, whereby it would follow that this level remains the ground state as more neutrons are added to ^{227}Fr. The tentative (1/2) spin assignment for ^{229}Fr fits with the intensity ratios of the HFS peaks in our experimental spectra, as shown in Fig. 9. Due to angular momentum coupling considerations, the intensity ratio between the two groups of transitions from the $7s\ ^2S_{1/2}$ ground state to the $8p\ ^2P_{3/2}$ excited state differs noticeably in the case of $I = 1/2$ and $I > 1/2$. A better agreement between the fit and experimental data is observed for $I = 1/2$ for ^{229}Fr. For ^{231}Fr however, this procedure did not lead to conclusive results, due to an increased experimental background (most likely originating from radium) and lower statistics observed in the ^{231}Fr hyperfine spectrum.

For ^{218m}Fr, there is no firm spin assignment. Debray et al. [10] tentatively assigned the spin value $I = (9^-)$ to ^{218m}Fr, based on an in-beam spectroscopy study feeding levels in ^{218}Fr that decay to this low lying isomer. This state is suggested to be the fully aligned member

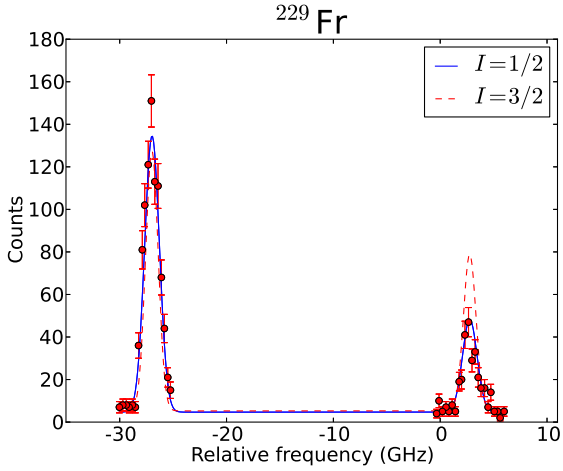

FIG. 9. (Color on-line) Fits to experimental data assuming the values $I = (1/2)$ and $I = (3/2)$ for ^{229}Fr. The better agreement with experiment for $I = (1/2)$ is evident.

of the $\pi(h_{9/2}) \otimes \nu(g_{9/2})$ multiplet. The second possible tentative spin-parity assignment is (8^-), based on α-decay feeding of several states of the $\pi(h_{9/2}) \otimes \nu(g_{9/2})$ multiplet in ^{214}At [39]. With these tentative spins the hyperfine parameters are extracted from the data, and related magnetic moments are determined (Table I). A further discussion on the structure of the isomeric state based on these moments is not possible, because calculated effective and empirical g-factor values for different possible configurations of this odd-odd isomer do not favor one or the other configuration. A firm spin assignment will provide a first step to better understanding the structure of this isomeric state.

C. Mean-square charge radii

In order to compare our ^{218m,219,229,231}Fr mean-square charge radii values with the ones from Dzuba et al. for $^{220-228}$Fr [45], we converted our $\delta\langle r^2\rangle^{A,221}$ values and the Dzuba $\delta\langle r^2\rangle^{A,212}$ values to be with respect to ^{213}Fr($N = 126$). The obtained $\delta\langle r^2\rangle^{N,126}$ values for francium can then be compared to the ones for radium [59], defined relative to $^{214}_{88}$Ra($N = 126$). The comparison is shown in Fig. 10. The neutron-rich radium isotopes have long been

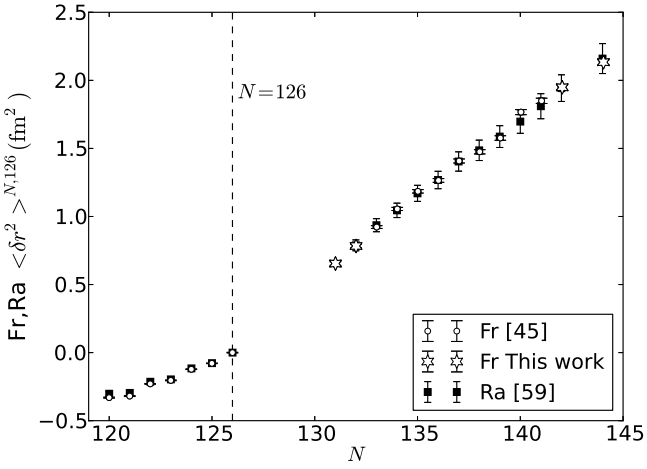

FIG. 10. Comparison of $\delta\langle r^2\rangle^{N,126}$ values for francium and radium. The francium $\delta\langle r^2\rangle^{N,126}$ values given in circles were taken from Dzuba et al. [45]. The radium $\delta\langle r^2\rangle^{N,126}$ values were taken from Wansbeek et al. [59].

associated with octupole deformations ([1] and references therein) and most noticeably ^{224}Ra displays a stable reflection-asymmetric deformation of its nuclear shape [2]. The theoretical error bands for radium are significant [59], making the comparison difficult, but nevertheless Fig. 10 shows that the two isotopic chains follow a very similar trend along the whole mass range. The newly measured ^{218m,219,229,231}Fr $\delta\langle r^2\rangle^{A,213}$ values follow the trend of the $\mathrm{Fr}_{133-141}$ isotopes measured by Coc. et al. [4].

The odd-even staggering (OES) effect of the changes in mean-square charge radii has been associated with reflection-asymmetric nuclear shapes [23, 24]. In most nuclei the OES order indicates that nuclei with odd-N have a smaller mean-square charge radius with respect to the average of their even-N neighbours. This is considered as normal OES ordering. The OES effect can be described by the $D(N;\delta\langle r^2\rangle^{N,126})$ factor, expressing how the change in mean-square charge radius deviates from the mean of its neighbours:

$$D(N;\delta\langle r^2\rangle^{N,126}) = (-1)^N \Bigg[\delta\langle r^2\rangle^{N,126} - \frac{\delta\langle r^2\rangle^{(N-1),126} + \delta\langle r^2\rangle^{(N+1),126}}{2}\Bigg]. \quad (4)$$

Eq. 4 is defined the same way as in Ref. [24], except that $\delta\nu$ was used in place of $\delta\langle r^2\rangle$. In the present discussion $D(N;\delta\nu)$ cannot be used due to the different transitions under consideration. Coc. et. al. [24] attributed normal OES ordering to $D(N;\delta\nu) < 0$. This type of ordering is seen in most nuclei, as in cesium ($Z = 55$) for example [24]. Since we compare $D(N;\delta\langle r^2\rangle^{N,126})$ and the field shift constant has a negative sign, the values of $D(N;\delta\langle r^2\rangle^{N,126})$ compared to $D(N;\delta\nu)$ will have an opposite sign and therefore we attribute normal OES ordering to $D(N;\delta\langle r^2\rangle^{N,126}) > 0$. Figure 11 shows the result of applying Eq. 4 to the radii from Fig. 10, taking only the experimental error from the isotope shift into account [4, 60] and neglecting the systematic theoretical error from the uncertainty of the mass and field shift values [45, 59].

A similar approach was used in Ref. [23] for the study of the radium charge radii, from which it was concluded that between ^{220}Ra and ^{226}Ra the inverted OES points to octupole deformation in the ground state being well developed for the odd-N isotopes (^{221,223,225}Ra). They also offered a qualitative interpretation of the correlation between the inversion in the OES order with reflection-asymmetric shapes, in terms of the different influences of pairing correlations on the shape of the nuclear potential between odd- and even-N nuclei (Fig. 7 in Ref. [23]).

Our $D(N;\delta\langle r^2\rangle^{N,126})(^{220}\text{Fr})$ value lies slightly below zero, which implies that it sits at the border of the region with reflection-asymmetric shapes (having inverted OES). That is confirmed by earlier studies [18, 20], where observables could be interpreted without including stable octupole deformations, while other observables did include some degree of octupole deformation. Indeed, in Ref. [20], the authors could not adequately interpret the configuration of ^{220}Fr using core-quasiparticle calculations without octupole degrees of freedom. Similarly in Ref. [18], the spin and parity $I(^{220}\text{Fr}) = 1^+$ could be interpreted by including octupole deformations. Evidence for reflection asymmetry was also found in

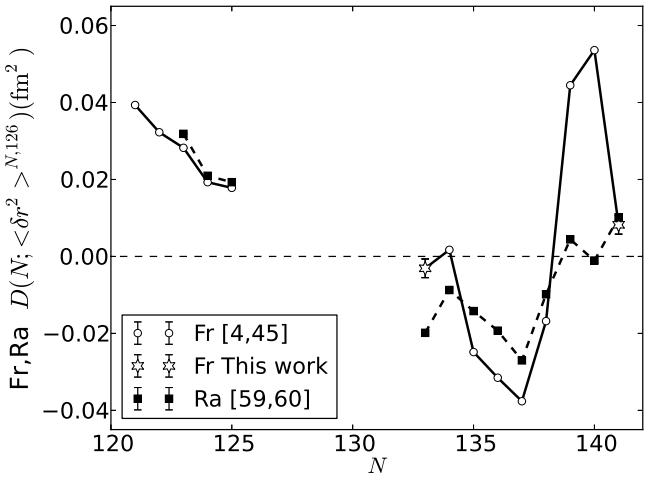

FIG. 11. Comparison of $D(N;\delta\langle r^2\rangle^{N,126})$ values for francium and radium. Only the uncertainties originating from the experimental isotope shift for the $\delta\langle r^2\rangle^{N,126}$ values were taken into account [4, 60], due to the large theoretical errors on the $\delta\langle r^2\rangle^{N,126}$ values for radium [59].

the form of parity doublet decay bands by [12], who interpreted this isotope to be in the transition region between quadrupole-octupole deformations and spherical symmetry.

The positive value for $D(N;\delta\langle r^2\rangle^{N,126})(^{228}\mathrm{Fr})$ establishes a normal OES extending from ^{226}Fr onwards. However, the value for ^{228}Fr is considerably lower than the $D(N;\delta\langle r^2\rangle^{N,126}(^{226,227}\mathrm{Fr}))$ values. The $\mu(^{228}\mathrm{Fr})$ and $Q_2^s(^{228}\mathrm{Fr})$ values were qualitatively well reproduced by Ref. [20] without including octupole deformations, while in Ref. [18] the $I(^{228}\mathrm{Fr}) = 2^-$ value is reproduced only by taking octupole deformation into account. Our positive $D(N;\delta\langle r^2\rangle^{N,126})(^{228}\mathrm{Fr})$ value supports the absence of octupole deformations in the ground state of ^{228}Fr.

V. SUMMARY AND CONCLUSIONS

The hyperfine spectra of ^{218m,219,229,231}Fr have been measured using the new Collinear Resonance Ionization Spectroscopy (CRIS) beam line at ISOLDE, CERN. From the measured spectra, the magnetic dipole moment, and changes in mean-square charge radii values

were extracted based on known and assumed spin values. This allowed nuclear structure conclusions to be drawn for these nuclei. The isomeric state ^{218m}Fr and the ground state of ^{219}Fr seem to possess the same degree of deformation, based on their mean-square charge radii. For ^{219}Fr, its spin-parity $9/2^-$ and $g(^{219}\text{Fr}) = +0.69(1)$ value are consistent with the unpaired valence proton occupying the $1h_{9/2}$ orbital. The $\mu(^{219}\text{Fr})$ value is smaller than the more neutron deficient ^{207,209,211,213}Fr isotopes, which are well described by the shell model $\pi 1h_{9/2}$ state and considered weakly deformed [20]. Its g-factor agrees well with those of ^{221,223,225}Fr isotopes, known to be well-deformed with $\epsilon_2 > 0.15$ [20]. The small negative value for $D(N;\delta\nu)(^{220}\text{Fr})$, supports the interpretation of this isotope being at the border of the region dominated by octupole deformations [12]. For ^{228}Fr there is no clear consensus on the presence of reflection asymmetry, but the relatively large positive $D(N;\delta\langle r^2\rangle^{N,126})(^{228}\text{Fr})$ value implies this nucleus lies outside of the region of reflection asymmetry. The $g(^{229}\text{Fr}) = +3.06(4)$ and $g(^{231}\text{Fr}) = +3.12(4)$ values, agree with the unpaired valence proton occupying the $\pi 3s_{1/2}$ intruder orbital. These values also compare well to the g-factor values of odd-A thallium isotopes, having a single $\pi 3s^{-1}_{1/2}$ hole state in the Z = 82 shell. For ^{229}Fr, the relative intensity ratios between the hyperfine structure peaks favor an $I = (1/2)$ spin assignment. Even though these considerations cannot be used to confirm the nuclear spins for ^{229,231}Fr, they do support the previous tentative $I^\pi(^{229,231}\text{Fr}) = (1/2^+)$ [17, 40] spin assignments. New theoretical work is required to better understand the specific structure of the neutron-rich francium isotopes. Further experimental information will be obtained using a narrow linewidth laser system, enabling the measurement of spin and spectroscopic quadrupole moments ($I > 1/2$), which will provide further information on the deformations of these nuclei.

ACKNOWLEDGEMENTS

We would like to thank the ISOLDE technical group for their support and assistance, and the GSI Target Laboratory for providing the carbon foils. This work has been supported by the BriX Research Program No. P7/12 and FWO-Vlaanderen (Belgium) and GOA 10/010 from KU Leuven, the Science and Technology Facilities Council consolidated grant ST/F012071/1 and continuation grant ST/J000159/1, and the EU Seventh Frame-

work through ENSAR(506065). K.T. Flanagan was supported by STFC Advanced Fellowship Scheme grant number ST/G006415/1. We acknowledge the financial aid from the Ed Schneiderman Fund at NYU.

[1] P. A. Butler and W. Nazarewicz, Reviews of Modern Physics **68**, 349 (1996).

[2] L. P. Gaffney, P. A. Butler, M. Scheck, A. B. Hayes, F. Wenander, M. Albers, B. Bastin, C. Bauer, A. Blazhev, S. Bönig, N. Bree, J. Cederkäll, T. Chupp, D. Cline, T. E. Cocolios, T. Davinson, H. De Witte, J. Diriken, T. Grahn, A. Herzan, M. Huyse, D. G. Jenkins, D. T. Joss, N. Kesteloot, J. Konki, M. Kowalczyk, T. Kröll, E. Kwan, R. Lutter, K. Moschner, P. Napiorkowski, J. Pakarinen, M. Pfeiffer, D. Radeck, P. Reiter, K. Reynders, S. V. Rigby, L. M. Robledo, M. Rudigier, S. Sambi, M. Seidlitz, B. Siebeck, T. Stora, P. Thoele, P. Van Duppen, M. J. Vermeulen, M. von Schmid, D. Voulot, N. Warr, K. Wimmer, K. Wrzosek-Lipska, C. Y. Wu, and M. Zielinska, Nature **497**, 199 (2013).

[3] R. K. Sheline, Phys. Lett. B **197**, 3 (1987).

[4] A. Coc, C. Thibault, F. Touchard, H. T. Duong, P. Juncar, S. Liberman, J. Pinard, J. Lermé, J. L. Vialle, S. Büttgenbach, A. C. Mueller, and A. Pesnelle, Phys. Lett. B **163**, 66 (1985).

[5] H. T. Duong, P. Juncar, S. Liberman, A. C. Mueller, R. Neugart, E. W. Otten, B. Peuse, J. Pinard, H. H. Stroke, C. Thibault, F. Touchard, J. L. Vialle, K. D. A. Wendt, and I. Collaboration, Europhysics Letters (EPL) **3**, 175 (1987).

[6] Y. A. Akovali, Nuclear Data Sheets **66**, 237 (1992).

[7] E. Browne, Nuclear Data Sheets **93**, 763 (2001).

[8] M. Aiche, A. Chevallier, J. Chevallier, S. Hulne, S. Khazrouni, N. Schulz, and J. C. Sens, Journal of Physics G: Nuclear Physics **14**, 1191 (1988).

[9] R. K. Sheline, C. F. Liang, and P. Paris, International Journal of Modern Physics E **03**, 1267 (1994).

[10] M. E. Debray, M. A. Cardona, D. Hojman, A. J. Kreiner, M. Davidson, J. Davidson, H. Somacal, G. Levinton, D. R. Napoli, S. Lenzi, G. de Angelis, M. De Poli, A. Gadea, D. Bazzacco, C. Rossi-Alvarez, and N. Medina, Phys. Rev. C **62**, 024304 (2000).

[11] C. F. Liang, P. Paris, J. Kvasil, and R. K. Sheline, Phys. Rev. C: Nuclear physics **44**, 676 (1991).

[12] C. F. Liang, P. Paris, and R. K. Sheline, International Journal of Modern Physics E **01**, 363 (1992).

[13] C. F. Liang, A. Péghaire, and R. K. Sheline, Modern Physics Letters A **05**, 1243 (1990).

[14] W. Kurcewicz, G. Løvhøiden, T. F. Thorsteinsen, M. J. G. Borge, D. G. Burke, M. Cronqvist, H. Gabelmann, H. Gietz, P. Hill, N. Kaffrell, R. A. Naumann, K. Nybø, G. Nyman, and J. Rogowski, Nucl. Phys. A **539**, 451 (1992).

[15] D. G. Burke, W. Kurcewicz, G. Løvhøiden, M. J. G. Borge, M. Cronqvist, H. Gabelmann, H. Gietz, P. Hill, N. Kaffrell, S. Mattsson, R. A. Naumann, K. Nybø, G. Nyman, J. Rogowski, G. L. Struble, and T. F. Thorsteinsen, Nucl. Phys. A **612**, 91 (1997).

[16] W. Kurcewicz, I. S. Grant, K. Gulda, A. J. Aas, J. Billowes, M. J. G. Borge, D. G. Burke, P. A. Butler, J. F. C. Cocks, B. Fogelberg, S. J. Freeman, G. D. Jones, E. Hagebø, P. Hoff, J. Hønsi, A. Lindroth, G. Løvhøiden, H. Mach, T. Martinez, R. A. Naumann, K. Nybø, G. Nyman, H. L. Ravn, B. Rubio, J. Simpson, A. G. Smith, J. F. Smith, K. Steffensen, J. L. Tain, O. Tengblad, and T. F. Thorsteinsen, Nucl. Phys. A **621**, 827 (1997).

[17] L. M. Fraile, M. J. G. Borge, H. Mach, R. Boutami, A. J. Aas, B. Fogelberg, L. M. García-Raffi, I. S. Grant, K. Gulda, E. Hagebø, W. Kurcewicz, J. Kvasil, M. J. López, G. Løvhøiden, T. Martnez, B. Rubio, J. L. Taín, and O. Tengblad, Nucl. Phys. A **686**, 71 (2001).

[18] R. K. Sheline, Phys. Rev. C **37**, 423 (1988).

[19] G. A. Leander and R. K. Sheline, Nucl. Phys. A **413**, 375 (1984).

[20] C. Ekström, L. Robertsson, and A. Rosén, Physica Scripta **34**, 624 (1986).

[21] S. E. Larsson, G. A. Leander, and I. Ragnarsson, Nucl. Phys. A **307**, 189 (1978).

[22] J. Kvasil, R. K. Sheline, I. Hivnáčová, C. F. Liang, and P. Paris, International Journal of Modern Physics E **01**, 845 (1992).

[23] S. A. Ahmad, W. Klempt, R. Neugart, E. W. Otten, P. G. Reinhard, G. Ulm, and K. D. A. Wendt, Nucl. Phys. A **483**, 244 (1988).

[24] A. Coc, C. Thibault, F. Touchard, H. T. Duong, P. Juncar, S. Liberman, J. Pinard, M. Carre, J. Lerme, J. L. Vialle, S. Büttgenbach, A. C. Mueller, and A. Pesnelle, Nucl. Phys. A **468**, 1 (1987).

[25] W. Borchers, R. Neugart, E. W. Otten, H. T. Duong, G. Ulm, and K. D. A. Wendt, Hyperfine Interactions **34**, 25 (1987).

[26] E. W. Otten, in *Treatise on Heavy Ion Science*, edited by D. A. Bromley, Vol. 8 (Springer US, Boston, MA, 1989) pp. 598–600.

[27] I. Talmi, Nuclear Physics A **423**, 189 (1984).

[28] K. T. Flanagan, K. M. Lynch, J. Billowes, M. L. Bissell, I. Budinčević, T. E. Cocolios, R. P. de Groote, S. De Schepper, V. N. Fedosseev, S. Franchoo, R. F. Garcia Ruiz, H. Heylen, B. A. Marsh, G. Neyens, T. J. Procter, R. E. Rossel, S. Rothe, I. Strashnov, H. H. Stroke, and K. D. A. Wendt, Phys. Rev. Letters **111**, 212501 (2013).

[29] T. E. Cocolios, H. H. Al Suradi, J. Billowes, I. Budinčević, R. P. de Groote, S. De Schepper, V. N. Fedosseev, K. T. Flanagan, S. Franchoo, R. F. Garcia Ruiz, H. Heylen, F. Le Blanc, K. M. Lynch, B. A. Marsh, P. J. R. Mason, G. Neyens, J. Papuga, T. J. Procter, M. M. Rajabali, R. E. Rossel, S. Rothe, G. S. Simpson, A. J. Smith, I. Strashnov, H. H. Stroke, D. Verney, P. M. Walker, K. D. A. Wendt, and R. T. Wood, Nucl. Instrum. & Methods B **317**, 565 (2013).

[30] K. M. Lynch, J. Billowes, M. L. Bissell, I. Budinčević, T. E. Cocolios, R. P. de Groote, S. De Schepper, V. N. Fedosseev, K. T. Flanagan, S. Franchoo, R. F. Garcia Ruiz, H. Heylen, B. A. Marsh, G. Neyens, T. J. Procter, R. E. Rossel, S. Rothe, I. Strashnov, H. H. Stroke, and K. D. A. Wendt, Physical Review X **4**, 011055 (2014).

[31] G. T. Ewan, E. Hagberg, B. Jonson, S. Mattsson, and P. Tidemand-Petersson, Nuclear Physics A **380**, 423 (1982).

[32] W. W. Meinke, A. Ghiorso, and G. T. Seaborg, Phys. Rev. **81**, 782 (1951).

[33] H. Frånberg, P. Delahaye, J. Billowes, K. Blaum, R. Catherall, F. Duval, O. Gianfrancesco, T. Giles, A. Jokinen, M. Lindroos, D. Lunney, E. Mané, and I. Podadera, Nucl. Instrum. & Methods in Physics Research Section B: Beam Interactions with Materials and Atoms **266**, 4502 (2008).

[34] E. Mané, J. Billowes, K. Blaum, P. Campbell, B. Cheal, P. Delahaye, K. T. Flanagan, D. H. Forest, H. Franberg, C. Geppert, T. Giles, A. Jokinen, M. Kowalska, R. Neugart, G. Neyens, W. Nörtershäuser, I. Podadera, G. Tungate, P. Vingerhoets, and D. T. Yordanov, The European Physical Journal A **42**, 503 (2009).

[35] C. Schulz, E. Arnold, W. Borchers, W. Neu, R. Neugart, M. Neuroth, E. W. Otten, M. Scherf, K. D. A. Wendt, P. Lievens, Y. A. Kudryavtsev, V. S. Letokhov, V. I. Mishin, and V. V. Petrunin, Journal of Physics B: Atomic, Molecular and Optical Physics **24**, 4831 (1991).

[36] S. Rothe, B. A. Marsh, C. Mattolat, V. N. Fedosseev, and K. D. A. Wendt, Journal of Physics: Conference Series **312**, 052020 (2011).

[37] M. M. Rajabali, K. M. Lynch, T. E. Cocolios, J. Billowes, M. L. Bissell, S. De Schepper, K. Dewolf, K. T. Flanagan, F. Le Blanc, B. A. Marsh, P. J. R. Mason, I. Matea, G. Neyens, J. Papuga, T. J. Procter, S. Rothe, G. S. Simpson, A. J. Smith, H. H. Stroke, D. Verney, P. M. Walker, K. D. A. Wendt, and R. T. Wood, Nucl. Instrum. & Methods in Physics Research Section A: Accelerators, Spectrometers, Detectors and Associated Equipment **707**, 35 (2013).

[38] K. M. Lynch, M. M. Rajabali, H. Aghaei-Khozani, J. Billowes, M. L. Bissell, F. Le Blanc, B. Cheal, T. E. Cocolios, S. D. Schepper, K. Dewolf, K. T. Flanagan, M. Hori, T. Kobayashi, B. A. Marsh, G. Neyens, J. Papuga, T. J. Procter, S. Rothe, G. S. Simpson, A. J. Smith, H. H. Stroke, and K. D. A. Wendt, Journal of Physics: Conference Series **381**, 012128 (2012).

[39] R. K. Sheline, P. Alexa, C. F. Liang, and P. Paris, Phys. Rev. C **59**, 101 (1999).

[40] M. J. G. Borge, D. G. Burke, H. Gietz, P. Hill, N. Kaffrell, W. Kurcewicz, G. Løvhøiden, S. Mattson, R. A. Naumann, K. Nybø, G. Nyman, and T. F. Thorsteinsen, Nucl. Phys. A **539**, 249 (1992).

[41] J. S. Grossman, L. A. Orozco, M. R. Pearson, J. E. Simsarian, G. D. Sprouse, and W. Z. Zhao, Phys. Rev. Letters **83**, 935 (1999).

[42] C. Ekström, S. Ingelman, G. Wannberg, and M. Skarestad, Hyperfine Interactions **4**, 165 (1978).

[43] E. Gomez, S. Aubin, L. A. Orozco, G. D. Sprouse, E. Iskrenova-Tchoukova, and M. S. Safronova, Phys. Rev. Letters **100**, 172502 (2008).

[44] K. M. Lynch, *Laser assisted nuclear decay spectroscopy: A new method for studying neutron-deficient francium*, Ph.D. thesis, The University of Manchester (2013), presented 19 Sep 2013.

[45] V. A. Dzuba, W. R. Johnson, and M. S. Safronova, Phys. Rev. A **72**, 022503 (2005).

[46] M. Wang, G. Audi, A. Wapstra, F. Kondev, M. MacCormick, X. Xu, and B. Pfeiffer, Chinese Physics C **36**, 1603 (2012).

[47] W. H. King, *Isotope Shifts in Atomic Spectra* (1984).

[48] A. K. Jain and B. Singh, Nuclear Data Sheets **107**, 1027 (2006).

[49] R. Bauer, J. Speth, V. Klemt, P. Ring, E. Werner, and T. Yamazaki, Nuclear Physics A **209**, 535 (1973).

[50] G. A. Leander and Y. S. Chen, Phys. Rev. C **37**, 2744 (1988).

[51] C. E. Bemis, Jr., F. K. McGowan, J. L. C. Ford, Jr., W. T. Milner, P. H. Stelson, and R. L. Robinson, Phys. Rev. C **8**, 1466 (1973).

[52] R. Menges, U. Dinger, N. Boos, G. Huber, S. Schröder, S. Dutta, R. Kirchner, O. Klepper, T. Köhl, D. Marx, and G. D. Sprouse, Zeitschrift für Physik A Hadrons and Nuclei **341**, 475 (1992).

[53] J. A. Bounds, C. R. Bingham, H. K. Carter, G. A. Leander, R. L. Mlekodaj, E. H. Spejewski, and W. M. Fairbank, Jr., Phys. Rev. C **36**, 2560 (1987).

[54] C. Bengtsson, C. Ekström, L. Robertsson, and J. Heinemeier, Physica Scripta **30**, 164 (1984).

[55] C. Ekström, G. Wannberg, and Y. S. Shishodia, Hyperfine Interactions **1**, 437 (1975).

[56] P. Raghavan, Atomic Data and Nuclear Data Tables **42**, 189 (1989).

[57] R. Neugart, H. H. Stroke, S. A. Ahmad, H. T. Duong, H. L. Ravn, and K. D. A. Wendt, Phys. Rev. Letters **55**, 1559 (1985).

[58] R. C. Thompson, W. Wilcke, J. R. Huizenga, W. K. Hensley, and D. G. Perry, Phys. Rev. C **15**, 2019 (1977).

[59] L. W. Wansbeek, S. Schlesser, B. K. Sahoo, A. E. L. Dieperink, C. J. G. Onderwater, and R. G. E. Timmermans, Phys. Rev. C **86**, 015503 (2012).

[60] K. D. A. Wendt, S. A. Ahmad, W. Klempt, R. Neugart, E. W. Otten, and H. H. Stroke, Zeitschrift für Physik D Atoms, Molecules and Clusters **4**, 227 (1987).

5.3 Discussion of high-resolution results

The technical developments described in Chapter 3 and Article II in Appendix A, made it possible to resolve the upper state $8p\ ^2P_{3/2}$ hyperfine structure during the 2014 experimental campaign. This allowed the extraction of the spectroscopic quadrupole moments, as described in Chapter 4. The good agreement of the experimental spectroscopic quadrupole moment of ^{221}Fr with literature value justifies a good level of confidence in the new experimental value for the spectroscopic quadrupole moment of ^{219}Fr: $Q_s(^{221}\mathrm{Fr}) = -1.21(2)$ eb. This section will present an extended discussion of the physical interpretation of this result, while a short version of this discussion is featured in Article II in Appendix A. In order to understand the interpretation of the results given in literature for the neighboring francium isotopes and build on them using this new result, the nuclear Coriolis interaction will first be introduced.

5.3.1 The Coriolis interaction in nuclei

The Coriolis effect in classical physics is a consequence of rotational motion, with the most prominent effects originating from the rotational motion of the Earth. As an example, consider a projectile fired from the equator directly northwards. If there were no rotational motion of the Earth, the projectile would land in a location directly north of the starting point. However, due to the rotation of the Earth the object starting at the equator will have a higher velocity component towards the east in the direction of the spinning of the earth compared to northern parts of the Earth. Therefore the object will in fact land in a location to the north-east with respect to the starting point, following a curved path. This can lead to significant observable effects such as the deflection of winds and currents in the ocean and also effects on airplanes and missiles. This same principle is behind the Corolis effects in nuclei which will now be discussed.

Figure 5.7 shows a prolate deformed nucleus with Z being the axis of deformation. If the valence nucleon is considered a single particle with angular momentum $\mathbf{j}$ outside of the rotating core with rotational angular momentum $\mathbf{R}$, then the total angular momentum of the nucleus (also referred to as nuclear spin) $\mathbf{I}$ is given by the vector sum $\mathbf{I} = \mathbf{R} + \mathbf{j}$. Here it is assumed that the valence nucleon does not further polarize the nucleus, which is already assumed to be deformed. The projection of the total angular momentum on the axis of deformation is labeled as K in Fig. 5.7. Now the rotational Hamiltonian of the nucleus can be defined as

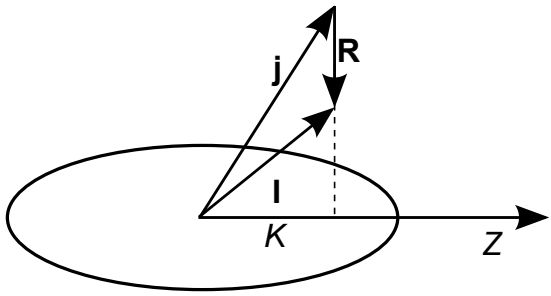

Figure 5.7: A graphical representation of a nucleus which is prolate deformed along the Z axis. Here $\mathbf{j}$ represents the single particle orbital angular momentum. The nucleus rotates around an axis perpendicular to the axis of deformation with total rotational angular momentum $\mathbf{R}$. The total angular momentum $\mathbf{I}$ is then a result of the coupling between $\mathbf{R}$ and $\mathbf{j}$. The projection of the total angular momentum on the axis of deformation is labeled as K.

$$H_{rot} = \frac{\hbar^2}{2\Theta}\mathbf{R}^2 = \frac{\hbar^2}{2\Theta}(\mathbf{I}-\mathbf{j})^2 = \frac{\hbar^2}{2\Theta}(\mathbf{I}^2+\mathbf{j}^2-2\mathbf{I}\cdot\mathbf{j}), \tag{5.7}$$

where $\hbar$ is the Planck constant $\hbar = 1.05457173 \times 10^{-34}\mathrm{m^2kg/s}$ and Θ is the moment of inertia of the nucleus. Introducing raising and lowering operators $\mathbf{I}_\pm = \mathbf{I}_1 \pm i\mathbf{I}_2$ and $\mathbf{j}_\pm = \mathbf{j}_1 \pm i\mathbf{j}_2$ into Eq. 5.7, the eigenvalues of the rotational Hamiltonian can be calculated in the Nilsson basis $|I, K\rangle$, with good quantum numbers I and K

$$E(I) = \frac{\hbar^2}{2\Theta}\left[I(I+1) - 2K^2 + \langle \mathbf{j}^2\rangle\right] + V_{\mathrm{Coriolis}}, \tag{5.8}$$

where

$$V_{\mathrm{Coriolis}} = -\frac{\hbar^2}{2\Theta}\langle \mathbf{I}_+\mathbf{j}_- + \mathbf{I}_-\mathbf{j}_+\rangle. \tag{5.9}$$

In Eq. 5.8, $\langle \mathbf{j}^2\rangle$ is the expectation value of the single particle angular momentum and I is the eigenvalue of the total angular momentum operator. This equation expresses the energy levels of different states in a rotational band. For a given value of K and $\langle \mathbf{j}^2\rangle$ (so a fixed orientation of the single particle spins with respect to the Z-axis), different combinations of I and R are possible, thus defining the states of increasing spin I within the same rotational band. For an odd-A nucleus, the sequence of spins within a band will be $I = K, K+1, K+2...$

From the first term in Eq. 5.8, it can be seen that the energy spacings between the different members of a band are multiples of the inertial parameter $\frac{\hbar^2}{2\Theta}$. However, if the Coriolis term is sufficiently large, it can have a significant impact on these energy spacings, even changing the ordering of the different I levels, as illustrated below. An explicit calculation of the value of the Coriolis matrix element between two Nilsson wave functions ψ_{IK}, ψ_{IK+1} is given in the book of Casten [124], yielding:

$$\langle \psi_{IK} | V_{\mathrm{Cor}} | \psi_{IK+1} \rangle = \frac{-\hbar}{2\Theta} \sqrt{(I-K)(I+K+1)}\, \langle \psi_{IK} | \mathbf{j}_- | \psi_{IK+1} \rangle\, (U_1U_2 + V_1V_2), \tag{5.10}$$

where the $(U_1U_2 + V_1V_2)$ factor takes into account the effects of pairing. This factor in general reduces the Coriolis matrix element since its maximum value is unity. The $\langle \psi_{jK} | \mathbf{j}_- | \psi_{jK+1} \rangle$ matrix element in Eq. 5.10 can be calculated for a total Nilsson wave function consisting of different single j Nilsson wave functions by the expression:

$$\langle \psi_{jK} | \mathbf{j}_- | \psi_{jK+1} \rangle = \sum_j C_j^K C_j^{K+1} \sqrt{(j-K)(j+K+1)}, \tag{5.11}$$

where the coefficients C_j^K, C_j^{K+1} describe the contribution from each single j Nilsson wave function. Equation 5.10 shows that the Coriolis interaction will change the values of K by $\Delta K = \pm 1$, meaning that this interaction will mostly be a non-diagonal interaction, mixing states between rotational bands which differ by $\Delta K = \pm 1$. However, the states within a $K^\pi = 1/2^\pm$ rotational band are special, since they will have non-zero diagonal Coriolis matrix elements, which will be made clear in the following discussion. Due to the fact that it is not possible to distinguish states with a positive or negative projection of K on the deformation axis Z due to the reflection symmetric shape of the nucleus (as seen for example in Fig. 5.7), the wave function of a Nilsson state within a $K = 1/2$ band can be written as

$$|\psi_{K=1/2}\rangle = \alpha |K = 1/2\rangle + \beta |K = -1/2\rangle, \tag{5.12}$$

where $\alpha^2 + \beta^2 = 1$. It is now clear that the diagonal Coriolis matrix element $\langle \psi_{K=1/2} | V_{\mathrm{Cor}} | \psi_{K=1/2} \rangle$ will be different from zero, due to the $\Delta K = \pm 1$ contributions between the $|K = 1/2\rangle$ and $|K = -1/2\rangle$ states. This will cause the rotational energy levels of states within such $K^\pi = 1/2^\pm$ bands to be

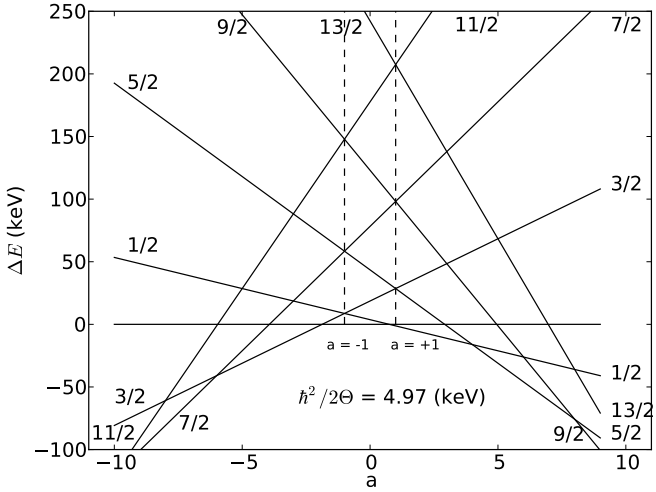

Figure 5.8: Rotational energy levels for different I within a $K^\pi = 1/2^\pm$ band as a function of the decoupling parameter a, calculated using Eq. 5.13.

perturbed just from the Coriolis interaction between the states within the same band, which will not occur for rotational bands with $K > 1/2$.

It is possible to calculate the rotational energy levels of the states within a $K^\pi = 1/2^\pm$ rotational band by applying Eqs. 5.10, 5.11 in Eq. 5.8, giving:

$$E(I)_{K^\pi=1/2^\pm} = \frac{\hbar^2}{2\Theta}\left[I(I+1) + a(-1)^{I+1/2}(I+\frac{1}{2})\right], \tag{5.13}$$

with the decoupling parameter $a = \sum_j (-1)^{j-1/2}(j+\frac{1}{2})C_j^2$. Due to the phase factor $(-1)^{I+1/2}$ in Eq. 5.13, the contribution to the Coriolis interaction alternates in sign depending on I. The change in the ordering of the different I levels of the same rotational band (same $K^\pi = 1/2^\pm$) due to the Coriolis interaction is shown in Fig. 5.8 as a function of the changing decoupling parameter a.

The dashed lines in the figure represent the $a = -1$ and $a = 1$ cases, for which pairs of energy levels with different I become degenerate such as the $I = 3/2, 5/2$, $I = 7/2, 9/2$ and $I = 11/2, 13/2$ levels in the case of $a = 1$. As the absolute value of the decoupling factor becomes larger than 1, the level orderings start to change as can be seen in Fig. 5.8. If $a = +5$ for example, the

lowest level is the $I = 5/2$ followed by the $I = 1/2$ and $I = 9/2$ levels. As for the phase factor $(-1)^{I+1/2}$ in Eq. 5.13, its effect can be seen in the fact that the $I = 1/2, 5/2, 9/2, 13/2$ levels all differing by $\Delta I = 2$ are all pushed down in energy while the $I = 3/2, 7/2, 11/2$ levels are pushed up with increasing positive a. This inversion of the level ordering will be important in the discussion of the ^{219}Fr results from literature and their relation with the new result for the spectroscopic quadrupole moment.

After introducing the Coriolis coupling and describing the evolution of its effects with the increasing decoupling parameter a on the rotational band energy levels, the next step is to show the relationship of these effects with the spectroscopic quadrupole moment. The physical interpretation of the increase of the decoupling parameter a lies in the increase of decoupling of the single valence particle motion from the rotating core, hence the term "decoupling". In the case of $a = 1$, the energy differences between the $I = 1/2, 3/2, 5/2, ...$ levels for an odd-A nucleus are the same as for the $I = 2, 4, 6...$ states of the neighboring even-even core. This means that the single particle acts as a spectator to the rotation of the core. This is the so-called **rotation aligned coupling scheme**, which is depicted in Fig. 5.9 b). In this scheme the single particle angular momentum **j** tends to be aligned with the rotational angular momentum **R** of the core. This results in low K values of the projection of the total angular momentum **I** on the deformation axis Z. The projection of **j** precessing around the axis X, leads to the introduction of α - the projection of **j** on the X axis. A consequence of this will be that the energy spacings between the levels in a rotational band will only depend on the rotation of the core R [125].

Figure 5.9 a) represents the case of **strong coupling**, which is present in well deformed nuclei, usually occurring in isotopes away from the shell closure. In this case **j** tends to be aligned with the deformation axis Z, giving rise to large K values. In order for this scenario to occur, the coupling of the valence particle angular momentum **j** to the deformation of the nucleus has to be much stronger than the perturbation on the motion of the valence particle due to the Coriolis interaction. This **strong coupling condition** can be expressed by the relation [126]:

$$|\langle -\hbar\omega_0\beta_2 r^2 Y_2^0(\theta_i, \phi_i)\rangle| \gg |\langle -\frac{\hbar^2}{2\Theta}(\mathbf{I}_+\mathbf{j}_- + \mathbf{I}_-\mathbf{j}_+)\rangle|, \tag{5.14}$$

where β_2 is the quadrupole deformation parameter. The moment of inertia Θ is in general small for weakly-deformed nuclei (near closed shells), it increases towards the mid-shell and decreases again when going towards the next shell closure [127]. Thus in the transitional region from deformed to spherical, where the deformation and moment of inertia decrease in going back towards

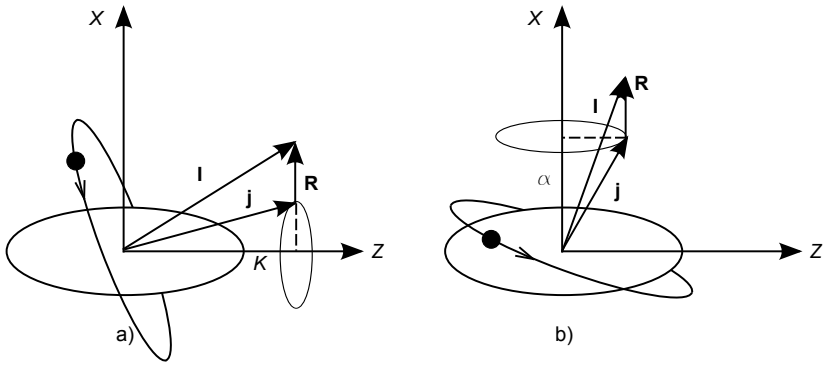

Figure 5.9: Figure showing the motion of a single valence particle of an odd-A nucleus outside a prolate deformed core: a) strong coupling of the valence nucleon spin **j** to the core deformation axis Z, b) decoupling of the valence nucleon from the symmetry axis, due to the Coriolis force that aligns the single particle angular momentum **j** to the rotational angular momentum of the core **R**.

spherical nuclei, the coupling to the deformation will decrease while the Coriolis interaction effect will increase due to factor $\frac{\hbar^2}{2\Theta}$, leading to a rotation aligned coupling scheme.

As mentioned in Chapter 2, the spectroscopic quadrupole moment Q_s that is measured experimentally can be used to extract the intrinsic quadrupole moment Q_0. In the strong coupling limit, the formula relating these two values is

$$Q_s = Q_0 \frac{3K^2 - I(I+1)}{(I+1)(2I+3)}. \tag{5.15}$$

Equation 5.15 shows that in the case of small K values and a prolate intrinsic shape ($Q_0 > 0$), the spectroscopic quadrupole moment becomes negative. Thus a large negative value of the spectroscopic quadrupole moment in a region of strong prolate deformation would be indicative of a low K value and a decoupled regime in which the Coriolis interaction plays an important role. The following section discusses the application of this reasoning to the interpretation of the new value of the spectroscopic quadrupole moment of ^{219}Fr.

5.3.2 Quadrupole moment of ^{219}Fr

The spectroscopic quadrupole moments of the francium chain $^{207-213,220-228}$Fr were measured with laser spectroscopy in 1985. by Coc et al., [28] and in 2013 the study was extended down to ^{204,205,206}Fr by Voss et al., [128]. The circles in figure 5.10 show the spectroscopic quadrupole moments for the odd-A francium isotopes below $N = 126$ and the neutron rich isotopes above $A = 220$ from these papers. The star point in the plot represents the new value for the spectroscopic quadrupole moment of ^{219}Fr, as measured using the high-resolution CRIS technique established in 2014. With 5 protons in the $h_{9/2}$ orbital, the quadrupole moment of odd-A francium isotopes is expected to be zero (half-filled orbits have no spectroscopic quadrupole moment [62]). A non-zero quadrupole moment thus reflects the effect of configuration mixing and core polarization, or in the case of a large quadrupole moment, points to core deformation. The quadrupole moment of the neutron-deficient odd-A francium isotopes is very small, suggesting a quasi-spherical core for these isotopes. The

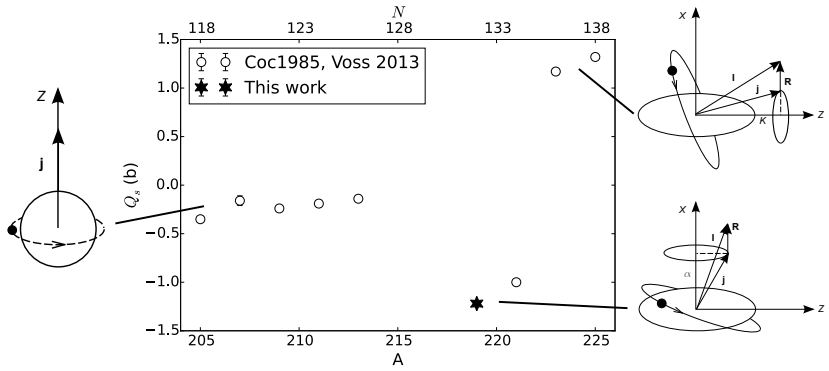

Figure 5.10: Spectroscopic quadrupole moment value of ^{219}Fr measured in this work, along with literature values for the neighboring francium isotopes. The strong coupling scheme from Fig. 5.9 a) is shown next to $Q_s(^{223,225}\text{Fr})$, while the rotational aligned scheme from Fig. 5.9 b) is associated with $Q_s(^{219,221}\text{Fr})$. The polarization of the nearly spherical neutron deficient francium isotopes by the valence proton to an oblate shape is indicated by a dashed line.

low negative Q_s values of the neutron deficient francium isotopes are due to configuration mixing with a configuration where a proton is excited out of the $h_{9/2}$ orbital, inducing a small oblate core polarization, as depicted in Fig. 5.10. The well deformed ^{223,225}Fr isotopes have large positive Q_s values, which is, assuming an intrinsic prolate shape of the nucleus as was done in the calculations

by Möller and Nix [129], an indication of the strong coupling scheme as indicated in Fig. 5.10 and Fig. 5.9 a). The ground state rotational bands for ^{223,225}Fr have previously been determined to have $K^\pi = 3/2-$ [35, 36]. For ^{225}Fr this was done by comparing to calculated cross sections for the ^{226}Ra(t, α)^{225}Fr reaction with observed experimental ones for different Nilsson states, with the state $3/2^-[532]$ determined to be the best candidate [36]. For ^{223}Fr, the $3/2^-[532]$ Nilsson state is assigned to the ground state based on the agreement of the experimentally measured magnetic dipole and electric quadrupole moments with results from particle-rotor calculations for this state [130]. Since the nuclear spin for both isotopes is $I(^{223,225}\text{Fr}) = 3/2$, it is clear that $K = I$ as would be expected for a strong coupling of the valence particle j to the nuclear deformation axis.

The newly measured $Q_s(^{219}\text{Fr}) = -1.21(2)$ eb value is negative, like that of ^{221}Fr. If the intrinsic shape of the nucleus is assumed to be prolate, this would indicate a small K value and thus a decoupling of the valence particle **j** from the core deformation. This is in line with the fact that ^{219}Fr lies in a transitional region between the strongly deformed isotopes, such as ^{229,231}Fr which were discussed in Article I, Sect. 5.2, and the more spherical isotopes below $N = 126$. Further support for this claim can be found in the literature interpretations for ^{219}Fr based on its rotational band structure.

This structure was investigated by Liang et al., [18], by studying the alpha decay and following gamma and electron transitions of ^{223}Ac. They concluded that the ground state rotational band of ^{219}Fr is of $K^\pi = 1/2^-$ character, with a very large decoupling parameter $a = 7.03$. This was determined by fitting the experimental rotational energy levels of the states within this band using the formula

$$E_I = E_0 + \frac{\hbar^2}{2\Theta}\left[I(I+1) + a(-1)^{I+1/2}(I+\frac{1}{2})\right], \tag{5.16}$$

where E_0 is the energy of the rotational band head. The same procedure was done by Sheline *et al.* [33] for the $K^\pi = 1/2^-$ ground state band in ^{221}Fr yielding $a = 4.33$. As previously mentioned, the ground state rotational band in ^{223}Fr is of $K^\pi = 3/2^-$ character, but there is also a $K^\pi = 1/2^-$ band at 55 keV which was determined by Kurcewicz *et al.* [35] to have a decoupling parameter of $a = 0.96$. Burke *et al.* [36] followed the same approach for the $K^\pi = 1/2^-$ band in ^{225}Fr, yielding unrealistic results, which the authors attributed to the uncertainty in assigning all of the levels to specific bands and mixing between other close-lying states. These results show that the decoupling parameter a is decreasing with increasing neutron number in the ^{219,221,223}Fr isotopes, supporting the claim that the effects of the Coriolis interaction are weakening in the heavier deformed isotopes. In the following paragraphs, the effects of the changing decoupling parameter on the energy level ordering within the $K^\pi = 1/2^-$ rotational bands in ^{219,221}Fr will be demonstrated.

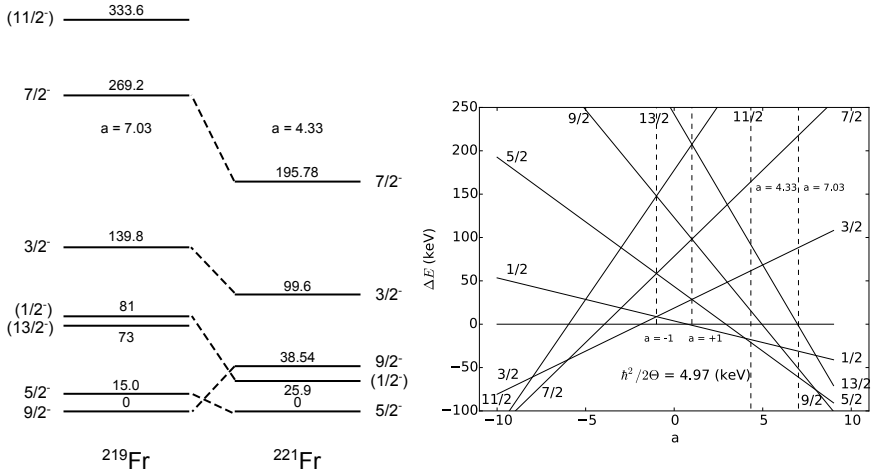

Figure 5.11: The left panel shows the $K^\pi = 1/2^-$ ground state rotational bands in ^{219,221}Fr, adapted from [18]. The right panel shows the change in the rotational energy level ordering in function of the decoupling parameter a. The $a = 7.03$ value as observed ^{219}Fr (see text for details) and the $a = 4.33$ value observed for ^{221}Fr are marked by dashed lines in the right panel.

The effect of the decreasing decoupling parameter between ^{219}Fr and ^{221}Fr can be seen in Fig. 5.11. As the deformation in ^{221}Fr gradually increases, the effect of the Coriolis interaction decreases, as seen from Eq. 5.14. Following this reasoning, the decoupling scheme given in the right hand side of Fig. 5.11 can be used to explain the different rotational band level orderings between the two isotopes. The effect of the large decoupling parameter value in ^{219}Fr is reflected in the pushing down of the $I = 9/2$ level of the ground state $K^\pi = 1/2^-$ rotational band. Figure 5.11 does not yet predict an inversion of the 9/2 and 5/2 levels at $a = 7.03$, but this is most likely related to the fact that the energy levels were calculated as a function of a using Eq. 5.13, with the assumption that the decoupling parameter is defined by a single j orbit. This approximation would strictly only be valid for a unique parity orbital and a realistic calculation would have to take into account contributions from other Nilsson levels. As for ^{221}Fr, the decreased decoupling parameter $a = 4.33$ can account for the ordering of the levels 5/2, 1/2, 9/2, as seen in Fig. 5.11.

The measured negative value of the spectroscopic quadrupole moment of ^{219}Fr can thus be interpreted as providing evidence for a decoupling of the single particle angular momentum **j** of the valence proton from the core deformation, leading to an increased Coriolis interaction that pushes the $I = 9/2$ state of the $K^\pi = 1/2^-$ rotational band down to be the ground state.

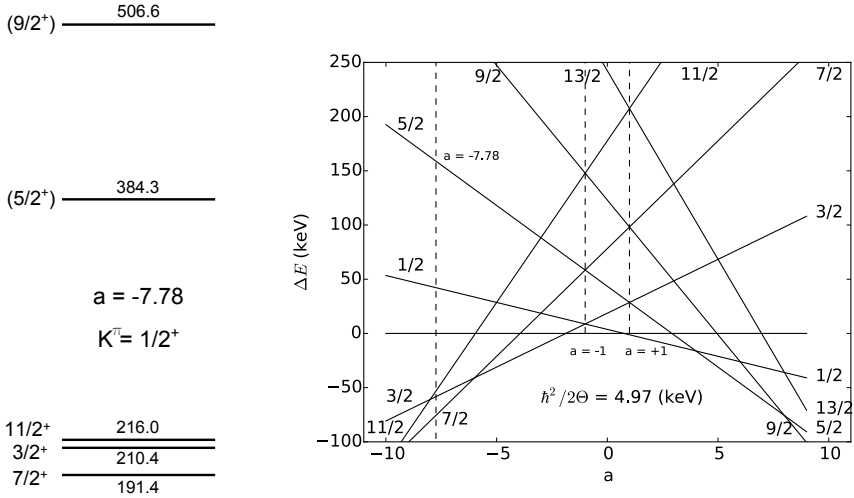

Figure 5.12: The left panel shows the $K^\pi = 1/2^+$ ground state rotational band in ^{219}Fr, adapted from [18]. The right panel shows the change in the rotational energy level ordering in function of the decoupling parameter a. The $a = -7.78$ value observed for this band is marked by a dashed line in the right panel.

A relevant point to note is that a rotational band of $K^\pi = 1/2^+$ lies at 191.4 keV above this ground state band with a large negative decoupling parameter $a = -7.78$ [18]. Figure 5.12 shows that the level ordering of the lowest levels within this band 7/2, 3/2, 11/2 is well reproduced by assuming a value of $a = -7.78$. The relevance of the decoupling parameter values of the $K^\pi = 1/2^\pm$ bands in ^{219}Fr lies in the fact that parity doublet bands lying relatively close in energy with decoupling parameters of equal magnitude but opposite sign are a characteristic sign of reflection-asymmetric shapes [17]. The discussion of whether or not the experimental result for the spectroscopic quadrupole moment can confirm the presence of octupole deformations in ^{219}Fr will be carried out in the next section.

Finally, an estimate of the quadrupole deformation parameter β_2 for ^{219}Fr can be made by using the spectroscopic quadrupole moment value and Eq. 5.15, with $K = 1/2$, to extract the intrinsic quadrupole moment Q_0. Then by using the relation [61]

$$\beta_2 = -7\sqrt{\frac{\pi}{80}} + \sqrt{\frac{49\pi}{80} + \frac{7\pi Q_0}{6Z1.2^2A^{2/3}}}, \tag{5.17}$$

the value of β_2 can be obtained. This procedure yielded the values: $Q_0(^{219}\text{Fr}) =$

335.5 e · fm^2 and $\beta_2(^{219}\mathrm{Fr}) = 0.094$. This is in line with the quadrupole deformation decreasing in ^{219}Fr as compared to ^{221}Fr, since Leander and Chen [8] obtained a value of $\beta_2(^{221}\mathrm{Fr}) = 0.1$ from their calculations. It is important to note here that our experimental $\beta_2(^{219}\mathrm{Fr})$ value was extracted by assuming that Eq. 5.15 still holds for ^{219}Fr, even though that formula is derived for the strong coupling limit.

5.3.3 Octupole deformation considerations

As previously discussed in Article I in Sec. 5.2, there are several indications that ^{219}Fr might possess a reflection-asymmetric deformation of its nuclear shape. The large decoupling parameters of opposite sign for the parity doublet bands as mentioned in the previous section, and the presence of parity doublet bands lying relatively close in energy are considered characteristic signs of reflection asymmetry [17].

Section 5.1.3 introduced the reflection-asymmetric rotor model, used to explain the experimentally determined properties of the odd-A francium isotopes ^{221,223,225,227}Fr in terms of octupole deformations. This section presents an application of this model for theoretically calculating the spectroscopic quadrupole moment of ^{219}Fr, to try and determine if the inclusion of octupole deformation improves agreement with our experimental value.

Based on this model, the value of the intrinsic quadrupole moment can be calculated using the equation

$$Q_{20} = \frac{3}{\sqrt{5\pi}} Z R_0^2 \bar{\beta}_2, \tag{5.18}$$

where $R_0 = 1.2\ A^{1/3}$ fm and $\bar{\beta}_2$ can be calculated as [8]

$$\begin{aligned} \bar{\beta}_2 \;=\; & \beta_2 + \sqrt{\frac{5}{4\pi}}\left[\frac{4}{7}\beta_2^2 + \frac{8}{15}\beta_3^2 + \frac{40}{77}\beta_4^2 + \frac{20}{39}\beta_5^2\right. \\ & \left. + \frac{196}{386}\beta_6^2 + \frac{24}{7}\frac{1}{\sqrt{5}}\beta_2\beta_4 + \frac{40}{21}\sqrt{\frac{7}{11}}\beta_3\beta_5 + \frac{60}{11}\frac{1}{\sqrt{13}}\beta_4\beta_6\right]. \end{aligned} \tag{5.19}$$

In order to try and reproduce the experimentally observed spectroscopic quadrupole moment of ^{219}Fr, the intrinsic quadrupole moment Q_{20} was first calculated from Eq. 5.18 and then used to extract the spectroscopic quadrupole moment using Eq. 5.15, by assuming that $K = 1/2$ since this is the ground

state rotational band. The β_2 value was estimated by linearly extrapolating the β_2 values from Table I in [8] of the neighboring francium isotopes. The values for $\beta_4, \beta_5, \beta_6$ were calculated from [8]:

$$\beta_4 = 0.5\beta_2 + 0.01, \tag{5.20}$$

$$\beta_5 = \beta_3(0.0089 + 0.117\beta_2 + 0.655\beta_4 - 0.0352\beta_3^2), \tag{5.21}$$

$$\beta_6 = 0.1055\beta_3^2 + 0.2215\beta_4^2 + 0.1476\beta_2\beta_4 - 0.0285\beta_2^3. \tag{5.22}$$

The value of β_3 was varied from $0.00 - 0.15$, and β_2 was adjusted so that the calculated theoretical spectroscopic quadrupole moment matches the experimental value. The different combinations of β_2 and β_3 that could reproduce the experimental spectroscopic quadrupole moment are given in Table 5.1.

Table 5.1: Table showing various combinations of the quadrupole β_2 and octupole β_3 deformation parameters which are able to reproduce the experimental value of the spectroscopic quadrupole moment $Q^s_{\text{exp}} = -1.21(2)$ eb. Further details in the text.

β_2	β_3	Q^s_{theo}
0.0880	0.0	-1.21
0.0875	0.05	-1.21
0.0865	0.07	-1.21
0.0855	0.09	-1.21
0.0835	0.12	-1.21
0.0805	0.15	-1.21

It is clear from Table 5.1 that any value of $\beta_3 = 0.00 - 0.15$ is able to reproduce the experimentally observed spectroscopic quadrupole moment with the corresponding β_2 value not changing significantly. Therefore the measured spectroscopic quadrupole moment value $Q_s(^{219}\text{Fr}) = -1.21(2)$eb, cannot confirm nor reject the presence of octupole deformations in this nucleus. The estimated theoretical values of $\beta_2 = 0.0805 - 0.0880$ on the other hand, do almost agree with the $\beta_2(^{219}\text{Fr}) = 0.094$ value extracted from the experimental Q_s moment in the previous section.

Chapter 6

Conclusions and outlook

This thesis presented the results of studies on radioactive francium isotopes with the newly developed technique of Collinear Resonance Ionization Spectroscopy (CRIS). The study of these isotopes was first performed in two experimental campaigns in August and October 2012, yielding results on the magnetic dipole moments and changes in mean-square charge radii of the $^{202-206}$Fr and ^{218m,219,229,231}Fr isotopes. This thesis focused on the analysis and interpretation of the neutron rich francium isotopes, which occur in/near a region of reflection-asymmetry. The experiments also provided results on the α-decay of the ground and isomeric states of ^{202,204,206}Fr, which were the subject of the PhD thesis of Kara Lynch [4] and the article by Lynch *et al.* [3]. The thesis also reported on the development work performed on the off-line ion source which contributed to the testing of the new laser system, which was used to increase the resolution of the CRIS technique enabling the measurement of the spectroscopic quadrupole moment of ^{219}Fr in November 2014. The results demonstrated the capabilities of the CRIS technique and extended the known nuclear properties of the francium isotopes towards the limits of stability.

The first experimental campaigns of 2012 demonstrated the high efficiency of the CRIS technique, which was determined to be > 1 %, with a background rate on the order of 10^{-5}. This high efficiency in combination with a nearly background-free signal detection, enabled the study of ^{202}Fr, produced at a rate of < 100 particles/s. This sensitivity in collinear laser spectroscopy yields an increase with 2 orders of magnitude as compared to collinear experiments based on resonance fluorescence photon detection. The systematic studies on the reference isotopes ^{207,211,220,221}Fr performed during these campaigns, determined a minimal error of 30 MHz on the extracted hyperfine parameter

and 100 MHz error on the isotope shift. The linewidth of the pulsed Ti:Sa laser used during these experimental campaigns was ~ 1.5 GHz, leading to the large uncertainty in the extracted $A(7s\ ^2P_{3/2})$ hyperfine parameter values. The large error on the extracted isotope shifts, originates from the scatter of the centroid value of the reference isotope ^{221}Fr as well as on the uncertainty of the readout of the wavemeter used in the experiment.

The magnetic dipole moments and changes in mean square charge radii of ^{218m,219,229,231}Fr, provided new insights into the structure of these neutron rich francium isotopes, located on both sides of the actinide region of reflection asymmetry. The g-factor value of ^{219}Fr showed that the valence protons in this nucleus occupy the $\pi 1h_{9/2}$ shell model orbital. Its value is indeed very close to the effective single particle g-factor for a proton in this orbital. The g-factor of ^{219}Fr is very close to that of the deformed ^{221,223,225}Fr isotopes, which are somewhat smaller than the g-factors of the near-spherical neutron deficient odd-A francium isotopes with $A < 213$, below the $N = 126$ shell closure. The magnetic dipole moments and resulting g-factor values for ^{229,231}Fr agree with the tentative $(1/2^+)$ spin assignments given in literature and point to an occupation of the intruder $3s^{-1}_{1/2}$ orbital, also assigned to be the ground state in ^{227}Fr. The measured changes in mean-square charge radii of ^{218m,219,229,231}Fr allowed a discussion of the odd-even staggering of these values. The discussion by Coc *et al.* [29] could be extended to include ^{220,228}Fr. The odd-even staggering values agree with the interpretation of ^{220}Fr being a nucleus with weak octupole correlations, and implies that ^{228}Fr lies outside of the region of reflection asymmetry.

During the period before the experimental campaign performed in November 2014, the off-line ion source was installed and demonstrated the capability of providing stable beams of ^{39}K. These stable beams were used to test the new laser system developments in a collinear geometry in the CRIS beamline prior to the on-line run on francium. The laser developments consisted of the use of a Pockels cell to chop the laser light of a narrow-band continuous wave laser, and to study the effect of the separation in time between the CW pulses and the ionizing laser pulses. Since the probed excited state $8p\ ^2P_{3/2}$ in francium is relatively long-lived with a lifetime of $\tau = 83.5 \pm 1.5$ ns [89], the optimal separation in time of the chopped CW pulses was found to be 100 ns, with the optimal pulse length of 100 ns. This separation served to reduce the lineshape distortions which can arise due to the simultaneous interaction of the atoms with both laser pulses. The total result of these laser developments was an increase in resolution of the CRIS technique to the level of laser spectroscopy with fluorescence detection, obtaining hyperfine structure spectra with 20(1) MHz full width at half-maximum. This made it possible to resolve the upper state $8p\ ^2P_{3/2}$ hyperfine splittings of francium, allowing for the extraction of spectroscopic

quadrupole moments. The newly measured spectroscopic quadrupole moment value of ^{219}Fr showed that the motion of the odd proton in this nucleus is decoupled from the nuclear quadrupole deformation of the core, which is in agreement with the literature interpretations based on measured rotational bands in this nucleus by Liang *et al.*[18].

The next step in the study of the francium isotopes near the region of reflection asymmetry, could be the study of the magnetic dipole moments and changes in mean-square charge radii of the odd-odd ^{230,232}Fr and extending the study to ^{233}Fr, as is part of an accepted addendum to the original francium experimental proposal at ISOLDE [91]. Just the measurement of the change in mean square charge radius for ^{230}Fr would add the points for ^{229,230}Fr on the odd-even staggering plot of Article I, while performing high resolution measurements on ^{229,231}Fr would finally firmly establish the $I = 1/2$ spin assignments by simply counting the number of observed hyperfine transitions.

Another interesting addition to the systematic study of the neutron rich francium isotopes in this region could come not from laser spectroscopy, but rather alpha decay spectroscopy of the odd-odd isotopes ^{222,224,226,228}Fr. The rotational bands in ^{220}Fr have been studied by Liang *et al.*[**?**] who observed a $K^\pi = 1^\pm$ parity doublet separated by ~ 140 keV and a tentative $K^\pi = 2^\pm$ parity doublet. The nearby odd-odd nucleus ^{224}Ac has been reported by Sheline *et al.*[123] to have a $K^\pi = 3^\pm$ parity doublet with a splitting off 7.3 keV, while Ahmad*et al.*[131] reported the same doublet with a splitting of 6 keV, claiming that this was the most octupole deformed nucleus ever observed. It would thus be interesting to study the francium isotopes in this region with alpha decay spectroscopy using the CRIS Decay Spectroscopy Station (DSS) and check for the presence of such closely spaced parity doublets.

In order to complete the picture of the evolution of the spectroscopic quadrupole moment values of the francium isotopes as reported in Article II, it would be interesting to measure these values for ^{217,215}Fr. Unfortunately, the extremely short half-lives of these isotopes of $t_{1/2}(^{215}\text{Fr}) = 86(5)$ ns [23] and $t_{1/2}(^{217}\text{Fr}) = 19(3)$ µs [132], make them impossible for study with the CRIS technique. The short half-lives would be appropriate for use with the time differential perturbed angular distribution (TDPAD) method [133], applied to fragment-separated beams of these exotic isotopes. It has been shown at GSI that alignment of a spin ensemble is created in a projectile-fragmentation reaction, and can be maintained if a fully-stripped fragment beam can be selected with a proper momentum distribution [134]. However, another complication then arises from the fact that these isotopes are known to be α-emitters. Thus, it would be very difficult to detect the α-decays, since such a fast beam needs to be implanted in a thick stopper material, from which the α-particles would not be able to escape. The measurement of these spectroscopic quadrupole moment

values will thus have to be delayed, until a suitable technique is developed.

Finally, it is worth to mention some of the plans for further studies of nuclear properties of other elements using the CRIS beamline at ISOLDE. The copper isotopes $^{76-79}$Cu with $Z = 29$ are planned to be studied to measure their magnetic dipole moments, quadrupole moments and charge radii in order to study the rigidity of the $Z = 28$ shell closure [135]. A plan also exists to extend the studies on neutron-rich potassium isotopes, which recently reached the new magic number $N = 32$. By measuring the electromagnetic moments and charge radii of ^{52,53}K with $Z = 19$, we can test the strength of these sub-shell closures at $N = 32, 34$. The gallium isotopes $^{80-87}$Ga with $Z = 31$ will also be used to study the $Z = 28$ and $N = 50$ shell closures, along with using the DSS for beta-gamma detection to distinguish the decay of the isomeric ^{80m}Ga state from that of the ground state and studying the half-lives of ^{86,87}Ga which are very important for understanding the astrophysical r-process [136]. Closer to the region of francium, a proposal has been accepted to study the neutron deficient isotopes of radium $^{205-214}$Ra[137]. The study of the charge radii of these isotopes will probe the departure from sphericity below $N = 126$ into more collective states, providing a rigorous test for relativistic mean-field theoretical models [138].

Appendix A

Use of Continuous Wave Laser and Pockells Cell for Sensitive High-Resolution Collinear Resonance Ionization Spectroscopy

A.1 Article II

This article describes the technical developments that lead to an increase in the resolving power of the CRIS technique, allowing for the measurement of hyperfine spectra with a 20(1) MHz full width at half-maximum. The key development was the use of a continuous wave laser together with an external Pockels cell, along with an optimal separation in time of the excitation and ionization laser pulses. The resulting increase in resolving power led to the first time measurement of the spectroscopic quadrupole moment of ^{219}Fr. The measured value is consistent with the interpretation of ^{219}Fr being a nucleus in the transitional region between the heavily deformed region of reflection asymmetry with $A \sim 223$ and the nearly spherical region with $A < 216$. The relatively large negative value of the quadrupole moment implies that the single particle motion of the odd-proton is decoupled from the nuclear deformation.

My contribution to this article was in the data analysis performed on the measured hyperfine spectra to extract the spectroscopic quadrupole moment and in writing the physics discussion of the results. My contribution to the technical developments was in my work on the off-line CRIS ion source which was used to test the high-resolution of the technique on stable beams of ^{39}K prior to the experimental campaign on radioactive beams of francium.

This paper has been accepted for publication in Physical Review Letters.

Use of a Continuous Wave Laser and Pockells Cell for Sensitive High-Resolution Collinear Resonance Ionization Spectroscopy

R. P. de Groote,[1,*] I. Budinčević,[1] J. Billowes,[2] M. L. Bissell,[1,2] T. E. Cocolios,[2] G.J. Farooq-Smith,[2] V. N. Fedosseev,[3] K. T. Flanagan,[2] S. Franchoo,[4] R. F. Garcia Ruiz,[1] H. Heylen,[1] R. Li,[4] K. M. Lynch,[1,2,5] B. A. Marsh,[3] G. Neyens,[1] R. E. Rossel,[3,6] S. Rothe,[3] H. H. Stroke,[7] K. D. A. Wendt,[6] S.G. Wilkins,[2] and X. Yang[1]

[1]*KU Leuven, Instituut voor Kern- en Stralingsfysica, B-3001 Leuven, Belgium*

[2]*School of Physics and Astronomy, The University of Manchester, Manchester M13 9PL, UK*

[3]*Engineering Department, CERN, CH-1211 Geneva 23, Switzerland*

[4]*Institut de Physique Nucléaire d'Orsay, F-91406 Orsay, France*

[5]*Physics Department, CERN, CH-1211 Geneva 23, Switzerland*

[6]*Institut für Physik, Johannes Gutenberg-Universität, D-55128 Mainz, Germany*

[7]*Department of Physics, New York University, New York, New York 10003, USA*

Abstract

New technical developments have led to a two orders of magnitude improvement of the resolution of the collinear resonance ionization spectroscopy (CRIS) experiment at ISOLDE, CERN, without sacrificing the high efficiency of the CRIS technique. Experimental linewidths of 20(1) MHz were obtained on radioactive beams of francium, allowing for the first time to determine the electric quadrupole moment of the short lived ($t_{1/2} = 22.0(5)$ ms) ^{219}Fr $Q_s = -1.21(2)$ eb, which would not have been possible without the advantages offered by the new method. This method relies on a continuous-wave laser and an external Pockels cell to produce narrowband light pulses, required to reach the high resolution in two-step resonance ionization. Exotic nuclei produced at rates of a few hundred ions/s can now be studied with high-resolution, allowing detailed studies of the anchor points for nuclear theories.

Laser spectroscopy of radioactive ion beams provides key nuclear observables to understand the evolution of the quantum many-body problem at the extremes of isospin by providing model-independent measurements of essential quantum observables. These observables are required to refine the current theories of the atomic nucleus and to further our understanding of the nuclear forces (see e.g. [1–3]). Alternatively, laser spectroscopy on exotic isotopes also provides input for precision tests of many-body QED [4] or to investigate hyperfine anomalies [5].

As the nucleon drip-lines are approached, nuclei often have short half-lives and are produced in minute quantities, which imposes strong efficiency requirements on laser spectroscopy techniques. At the same time, the spectral resolution of these experiments needs to be sufficiently high to allow extraction of all of the observables of interest. Over the past decades, many techniques have been developed with the aim of meeting both requirements, see for example [6] for a recent review.

One of these techniques is collinear laser spectroscopy, applied in a number of experiments around the world [7–11]. In this technique an accelerated ion or atom beam of a particular isotope is collinearly overlapped with a continuous wave (cw) laser beam, inducing resonant excitation of the hyperfine levels of the studied isotope. In most of these experiments the hyperfine structure is observed by measuring the fluorescence photons emitted by the de-excitations from the resonantly excited hyperfine levels. The use of accelerated ion beams in a collinear geometry enables typical collinear laser spectroscopy experiments to achieve resonance peak linewidths of the order of 40-70 MHz [7, 12, 13], which are sufficient to resolve the hyperfine structure in most elements. In combination with a bunched ion beam produced with a linear Paul trap, the technique is nowadays routinely performed on radioactive species with production rates down to several 1000 particles per second [7, 8]. A second very successful laser spectroscopic technique to study exotic isotopes is in-source laser spectroscopy [14]. It is based on the efficient resonant excitation of the hyperfine levels using a narrowband pulsed laser and the subsequent (resonant or non-resonant) laser ionization of these radioisotopes in the ion source. Ion detection is very efficient due to the high quantum efficiency of the particle detector and complete solid angle coverage. This allows very exotic nuclei with production rates down to a few particles per second to be accessed [15]. Resonance ionization spectroscopy (RIS) of radioactive beams is usually only performed with pulsed lasers, since only pulsed lasers can provide the high laser power densities required for

efficient ionization in an ion source. Because the resonance ionization takes place in a hot cavity, Doppler broadening limits the experimental linewidths to typically 4-5 GHz [15, 16]. A modification of the in-source approach relies on resonance ionization of atoms in a gas cell [17]. A combination of Doppler and pressure broadening results in linewidths of a few GHz. The in-gas cell laser spectroscopy method has recently been improved by doing the RIS in a supersonic gas jet rather than in the gas cell, which allows for a reduction of the total linewidth to several hundred MHz [18].

The collinear resonance ionization spectroscopy (CRIS) technique was proposed as a way to combine the efficiency of RIS with the Doppler-free conditions of a collinear experiment [19]. The method relies on collinearly overlapping an atom beam with a laser beam, thus avoiding Doppler and pressure broadening, and uses the detection of the laser-ionized atoms rather than the fluorescence photons, enhancing the sensitivity and selectivity. The first demonstration of the technique in the nineties served as a promising proof-of-principle, reaching a total efficiency of 10^{-5}, background rate of 10^{-8} and a linewidth of 50 MHz [20]. Results obtained at the dedicated CRIS beam line at ISOLDE, CERN in 2012 demonstrated an improved total experimental efficiency reaching 1 %, using a combination of bunched beams and pulsed lasers [21]. This efficiency extended laser spectroscopy measurements to radioactive species with production yields down to 100 particles per second. The spectral linewidth of 1.5 GHz was completely determined by the pulsed titanium-sapphire laser system that was used [22].

Pulsed laser light with a linewidth of the order of 50 MHz has been produced by pulse dye amplification (PDA) of a cw laser beam [20]. With this method, the final linewidth of the pulsed light is limited by the width of the Fourier transform of the laser pulse and further increased by frequency chirp caused by nano-second scale changes in the refractive index of the medium. For solid-state Ti:Sa lasers, this chirp can be corrected to reduce the linewidth to 6 MHz [23–26]. Another way of producing spectrally narrow laser pulses is by using injection seeding [27]. An important advantage of both methods is the high output powers such systems can achieve, although both come with the disadvantage of a rather challenging experimental setup. A different approach to the production of narrowband laser pulses uses an Electro-Optical Modulator (EOM) to modulate the amplitude of a cw laser beam rather than amplifying it [9, 28]. The extinction ratio, defined as the laser power during the pulse divided by the laser power during the off-time can be as good as 1:180 [28].

Since there is no amplification of the cw beam, the peak fluence of the laser pulses is low, but the final spectral linewidth is purely determined by the transform of the modulation and is not influenced by frequency chirp effects. An additional advantage is the smaller experimental footprint, since no pump laser or stabilization electronics are required. The radio-frequency modulation can induce sidebands in the atomic spectra which have to be accounted for.

In this Letter, we present the development of a laser ionization method based on a Pockels cell and a cw laser system to overcome some of the disadvantages of the methods described above. Using this system, the spectral resolution of the CRIS experiment was improved by nearly two orders of magnitude, without inducing optical pumping to dark states or reducing the experimental efficiency. The spectral linewidth of the laser pulses is purely Fourier-limited. The ability to tune the pulse length to the decay time of the atomic excited state under investigation is a key advantage compared to PDA or injection seeding, where the pulse length is fixed. The system was running at a repetition rate of 100 or 200 Hz to match the Nd:YAG laser, which means the induced sidebands will appear at 100 or 200 Hz. These sidebands are therefore too close to influence the atomic spectra. Furthermore, for a sufficiently long-lived excited state, the ionization laser can be delayed until after the excitation pulse, which has two important implications. Firstly, the excitation laser can probe the atomic system without the perturbation of the strong ionizing laser field, removing potential lineshape distortions. Secondly, power broadening due to both the excitation and the ionization laser is removed completely, even for high laser powers [29–31]. By exciting to a long-lived state, the resolution of the experiment is also enhanced significantly due to the smaller natural linewidth. This advantage is more difficult to exploit for techniques that use fluorescence detection, since the use of weak tranistions will considerably reduce signal rates.

The advantages described in the previous paragraph in combination with the efficiency of the CRIS technique will give access to nuclei with lower production rates and shorter half-lives across the nuclear chart. The improved performance of the CRIS technique is illustrated here with the measurement of the electric quadrupole moments of ^{219}Fr. This isotope is situated near the region of reflection-asymmetry [32–35]. Previous laser spectroscopy experiments performed on francium beams [36–39] did not have the required combination of resolution and sensitivity to extract the electric quadrupole moment of ^{219}Fr

($t_{1/2} = 22.0(5)$ ms [40]), produced with rates around $10^3 - 10^4$ particles per second. From the measured spins and magnetic moments of ^{219,221}Fr [36, 38] it was concluded that the unpaired valence proton in these nuclei occupies the $h_{9/2}$ orbital, while the charge radii of the francium isotopes follow the trend of the neighboring radium isotopes, indirectly showing that ^{219}Fr is located at the border of a region of octupole collectivity [38]. Direct measurements of octupole moments of radioactive beams with laser spectroscopy require a resolution below 10 MHz and are at present not possible, but indirect information can be derived from the quadrupole collectivity.

The ^{219,221}Fr beams are produced at the ISOLDE facility at CERN through a spallation reaction in a thick UC_x target induced by 1.4 GeV protons. The francium atoms are surface ionized in a hot capillary tube, accelerated to 40 keV, mass separated and then cooled and bunched in a gas-filled linear Paul trap [41]. The ion beam is then transported into the CRIS experiment [42], where it is neutralized through collisions with a potassium vapor. After passing through a differential pumping section, the neutral fraction of the beam is temporally and spatially overlapped with the laser beams in a UHV interaction region. The time synchronization is controlled using a Quantum Composers QC9258 digital delay generator. Once in the interaction region, the isotopes are resonantly excited through the $7s\ ^2S_{1/2} - 8p\ ^2P_{3/2}$ transition at 422.7 nm using chopped cw light. The lifetime of the excited state is $\tau = 83.5 \pm 1.5$ ns [43] and very well suited for delayed RIS. The resonantly excited atoms are non-resonantly ionized using 1064 nm laser light, using different delay times between the excitation and ionization laser pulses. These ions are deflected onto a copper plate, and the secondary electrons are detected using a microchannel plate (MCP). The signals produced by the MCP are then amplified, discriminated and processed by a National Instruments USB-6211 DAQ card. This USB card is triggered by the Quantum composer every 100 ms, in synchronization with the laser system and ion beam delivery.

The laser system used for the high-resolution resonance laser ionization is presented in Fig. 1. The laser light for the resonant step was provided by a Matisse TS cw titanium-sapphire laser, which was frequency scanned using the Matisse Commander software. A small pick-off of the 2.7 W fundamental laser beam was sent into a HighFinesse WSU2 wavemeter, which was regularly calibrated to an external temperature stabilized HeNe laser. The fundamental laser beam of the Matisse was frequency doubled to 422.7 nm using a Wavetrain external cavity frequency doubler. The laser beam then passed through a half-

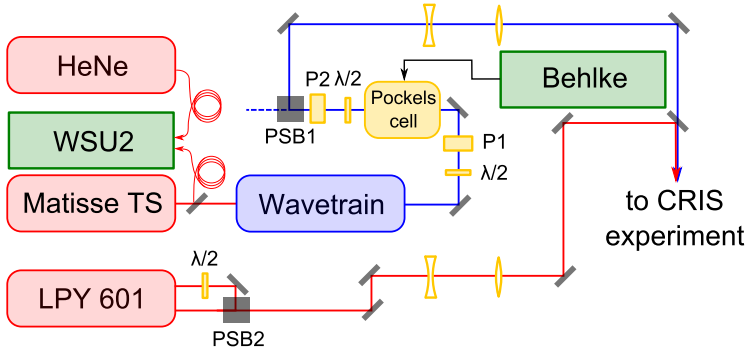

FIG. 1. [Color online] A schematic overview of the laser setup. The laser light for the excitation step is produced by a Matisse TS titanium-sapphire continuous wave laser which is frequency doubled by a Wavetrain doubler and sent through a light chopping setup (see text for more details). The 1064 nm light for the non-resonant ionization step is produced by a Litron LPY 601 50-100 PIV Nd:YAG laser operating at either 100 or 200 Hz. Light of both lasers is focused and spatially overlapped before being sent to the CRIS experiment.

wave plate, Glan-Taylor polarizer (P1) and Pockels cell, and then through another half-wave plate and a second Glan-Taylor polarizer (P2). A polarizing beam splitter cube (PSB1) positioned further along the beam path only reflected light with one particular polarization, which was then further transported into the CRIS beam line. The polarization axis of the light was rotated by $\pi/2$ by the Pockels cell for an applied voltage of 2.4 kV. Through the use of a Behlke FSWP91-01 fast square wave pulser, the voltage applied to the Pockels cell could be rapidly switched from 0 to 2.4 kV. The combination of the rapid switching of the laser light polarization and the polarization-sensitive beam splitter cube therefore allowed for creating short pulses of laser light. Optimized transmission efficiencies of 65% and extinction ratios of 1:2000 were achieved. The measured rise and fall times of the light pulses were 10 ns. The power of the 422.7 nm light was 25 mW just before the entry window to the CRIS beamline. The laser efficiency obtained with this laser system was comparable to the low-resolution laser system that was used for the previous CRIS experiment [21]. This was determined by comparing back-to-back measurements using the high-resolution laser system and the previous system on ^{206}Fr. Fig. 2 shows the saturation curve for the excitation step.

The red curve is the best fitting saturation function, defined as

$$I(P) = A \cdot \frac{P/P_0}{1 + P/P_0}, \tag{1}$$

which yields a saturation power of $P_0 = 9 \pm 4\,\mathrm{mW}$. Light from the two Nd:YAG cavities in the Litron LPY 601 50-100 PIV laser system was overlapped using a half wave plate and a polarizing beam splitting cube (PSB2), yielding $2{\times}4\,\mathrm{W}$ of laser light just before the CRIS entry window. The synchronization of the two cavities can be tuned to change the repetition rate of the Litron laser system to either 100 or 200 Hz.

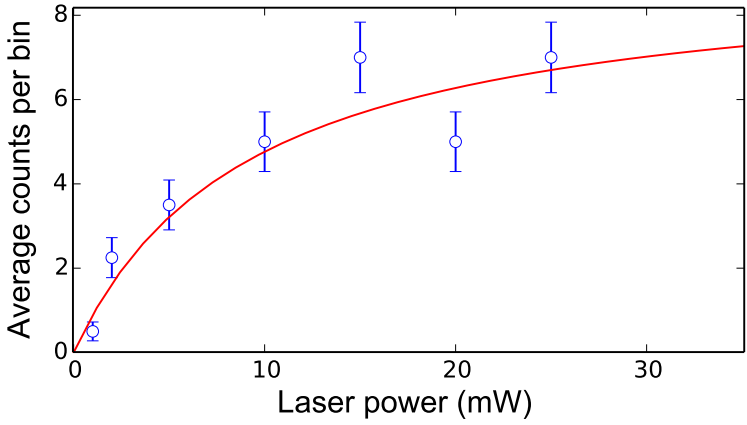

FIG. 2. [Color online] Saturation curve for the excitation laser step, obtained by fixing the laser frequency at the resonance frequency of the strongest peak in the left multiplet of ^{221}Fr. The ionization laser fired at the end of the excitation pulse, with a power of 8 W. From the best fitting saturation function (shown in red), a saturation power of $P_0 = 9 \pm 4\,\mathrm{mW}$ is extracted.

By performing systematic measurements of the hyperfine structure of ^{221}Fr, optimal pulse lengths of 100 ns and ionization laser delay of 100 ns with respect to the rise time of the excitation pulse were determined. With these settings the blue histogram in Fig. 3 is obtained. If the ionization step is delayed less then 100 ns, and therefore arrives temporally overlapped with the excitation pulse, the grey spectrum in Fig. 3 is obtained. The peaks broaden and shift to the high-frequency side, and an additional structure also appears on the high-frequency side of the resonance peaks. When a constant 2.4 kV voltage is applied

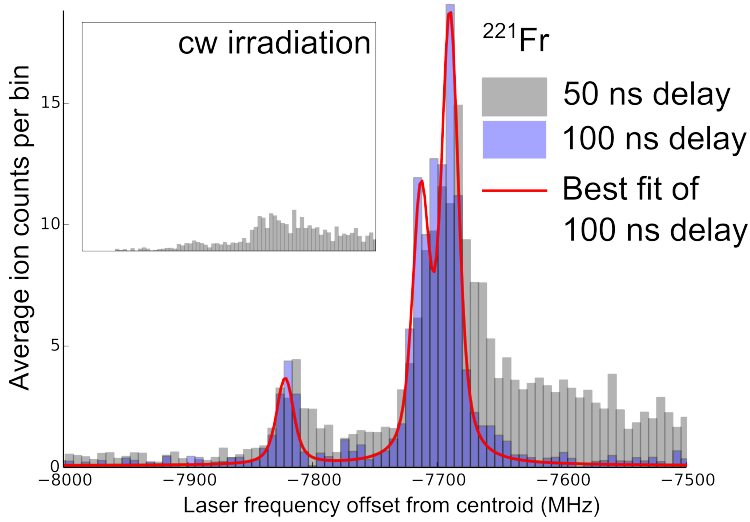

FIG. 3. [Color online] Inset: Resonance ionization spectrum with continuous wave laser light in the first step. The scale and range on x- and y-axis are the same as the main plot. Main: RIS of the lowest frequency multiplet of ^{221}Fr using chopped cw light with a pulse length of 100 ns for two delay times of the ionization step.

(and the atoms are therefore continuously irradiated), the spectrum in the inset of Fig. 3 is obtained. The event rate is much lower due to optical pumping effects, and the peaks are significantly broadened and shifted to higher frequencies. Fig. 3 also shows the best fitting function for the optimal settings (in red), consisting of the sum of Voigt profiles centered on the resonance positions. A total linewidth of 20(1) MHz is obtained. The total linewidth is dominated by the remaining Doppler spread of the atom beam and the spectral broadening of the excitation pulse due to the chopping, estimated at approximately 10 MHz by taking the Fourier transform of the time profile of the laser pulse.

An example of a resonance ionization spectrum of ^{219}Fr is shown in Fig. 4. The linewidth of 20(1) MHz is sufficient to resolve all six expected resonance peaks, which are fitted as described in e.g. [38]. The weighted mean of the fitted hyperfine parameters are summarized in Table I. From these parameters, the nuclear magnetic dipole moment μ and electric quadrupole moment Q_s were determined relative to the values for ^{221}Fr in [36, 37]. The

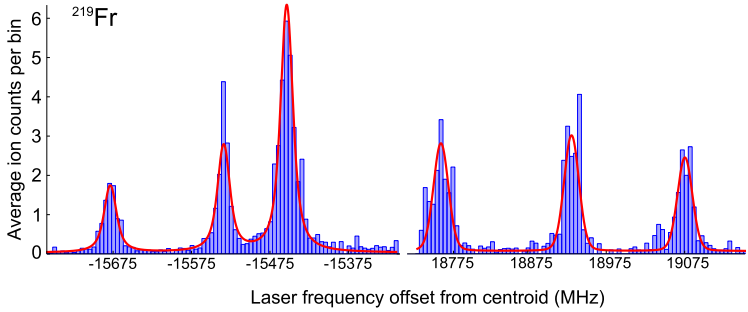

FIG. 4. [Color online] Example of an experimental hyperfine spectrum of ^{219}Fr and the best fitting function (red line) consisting of a sum of Voigt profiles centered on the resonance positions.

TABLE I. Summary of the extracted hyperfine structure constants for the $7s^2S_{1/2}$ atomic ground state and $8p^2P_{3/2}$ excited state of ^{219,221}Fr (values in MHz). The extracted magnetic dipole moment and electric quadrupole moment are also given. Literature values were obtained from [36–38].

	A($7s^2S_{1/2}$)	A($8p^2P_{3/2}$)	B($8p^2P_{3/2}$)	$\mu(\mu_N)$	Q_s(eb)
$219_{\text{lit.}}$	+6820(30)	–	–	+ 3.11(4)	–
$219_{\text{exp.}}$	+6851(1)	+24.7(5)	-104(1)	+ 3.13(4)	-1.21(2)
$221_{\text{lit.}}$	+6210(1)	+22.4(1)	-85.7(8)	+ 1.57(2)	-1.00(1)
$221_{\text{exp.}}$	+6209(1)	+22.3(5)	-87(2)	+ 1.57(2)	-1.02(3)

newly measured value of $Q_s = -1.21(2)$ eb ($\beta_2 = 0.094$) for ^{219}Fr is plotted along with the Q_s values of other francium isotopes from literature [9, 36] in Fig. 5. The Q_s values illustrate the different structures in these odd-A francium isotopes: for $A < 215$ the quadrupole moment is nearly zero, as expected in the shell model for isotopes with a half-filled $h_{9/2}$ proton orbit [44]. The small deviation from zero is a signature of configuration mixing and an increasing contribution from core polarization towards the neutron-deficient region. The large absolute values for the quadrupole moments of $^{219-225}$Fr are a signature for deformation in their ground states. The sudden change from strongly negative to strongly positive spectroscopic quadrupole moments is understood in the Nilsson model as due to the changing influence of Coriolis mixing on these prolate deformed structures. Coriolis mixing is strongest in $K = 1/2$ bands and tends to decouple the odd-particle spin from the deformation axis [45, 46]. The

$9/2^-$ ground state in ^{219}Fr is known to be a member of the $K = 1/2^-$ band [47]. Thus the odd-proton spin is decoupled from the nuclear deformation axis (see (b) in Fig. 5), yielding a negative quadrupole moment ($K < I$). In the heavier francium isotopes, the deformation gradually increases and the nuclear spin gets gradually more coupled to the deformation axis. The $5/2^-$ ground state in ^{221}Fr was interpreted also as a member of the $K = 1/2^-$ band, but with a much smaller decoupling parameter a. In ^{223,225}Fr the $3/2^-$ ground state is a member of the $K = 3/2^-$ band and thus strongly coupled to the deformation axis ($K = I$), resulting in a positive quadrupole moment.

In summary, we have presented a novel high resolution, highly efficient collinear resonance ionization spectroscopy technique. By probing a weak atomic transition in francium, a linewidth of 20(1) MHz was achieved, which represents an improvement of the experimental resolution by nearly two orders of magnitude compared to our previous measurements [21]. The advantages of the new method in terms of resolution, efficiency and systematic lineshape effects were illustrated by performing laser spectroscopy on beams of radioactive francium, using the 422.7 nm transition to the excited $8p^2P_{3/2}$ state. The performance of the technique allowed measurement of the electric quadrupole moment of ^{219}Fr ($t_{1/2} = 22.0(5)$ ms) for the first time.

We acknowledge the support of the ISOLDE collaboration and technical teams. We are grateful to the COLLAPS collaboration for the use of their CW Ti:Sa laser system and wavetrain doubling unit. This work was supported by the BriX Research Program No. P7/12 and FWO-Vlaanderen (Belgium) and GOA 10/010 from KU Leuven, the Science and Technology Facilities Council consolidated grant ST/F012071/1 and continuation grant ST/J000159/1, and the EU Seventh Framework through ENSAR(506065). K. T. F. was supported by STFC Advanced Fellowship Scheme Grant No. ST/G006415/1 and ERC Consolidator Grant no. 648381. We acknowledge the financial aid from the Ed Schneiderman Fund at New York University.

* ruben.degroote@fys.kuleuven.be

[1] S. R. Beane, E. Chang, S. Cohen, W. Detmold, H. W. Lin, K. Orginos, A. Parreño, M. J. Savage, and B. C. Tiburzi ((NPLQCD Collaboration)), Phys. Rev. Lett. **113**, 252001 (2014).

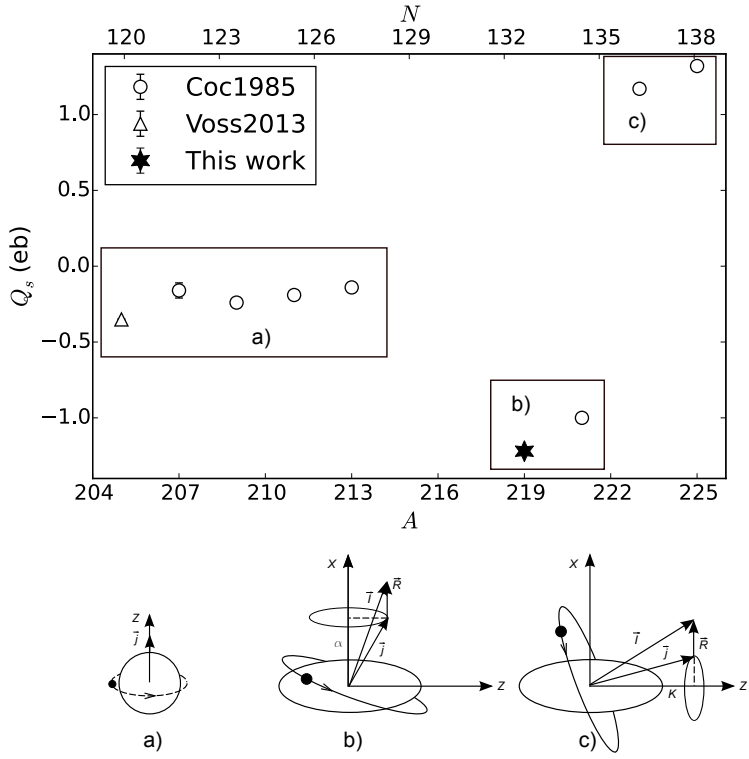

FIG. 5. Spectroscopic quadrupole moment values of ^{219}Fr measured in this work, along with literature values for the neighboring odd francium isotopes. The Z axis in the three schemes is the axis of deformation. $\vec{j}$ is the single particle angular momentum of the valence proton, $\vec{I}$ the total nuclear spin, and $\vec{R}$ the rotational angular momentum of the nucleus. K is the projection of j on Z and α is the projection on the X axis.

[2] A. Ekström, G. R. Jansen, K. A. Wendt, G. Hagen, T. Papenbrock, B. D. Carlsson, C. Forssén, M. Hjorth-Jensen, P. Navrátil, and W. Nazarewicz, Phys. Rev. C **91**, 051301 (2015).

[3] Z.-T. Lu, P. Mueller, G. W. F. Drake, W. Nörtershäuser, S. C. Pieper, and Z.-C. Yan, Rev. Mod. Phys. **85**, 1383 (2013).

[4] W. Nörtershäuser, C. Geppert, A. Krieger, K. Pachucki, M. Puchalski, K. Blaum, M. L. Bissell, N. Frömmgen, M. Hammen, M. Kowalska, J. Krämer, K. Kreim, R. Neugart, G. Neyens,

R. Sánchez, and D. T. Yordanov, Phys. Rev. Lett. **115**, 033002 (2015).

[5] J. Zhang, M. Tandecki, R. Collister, S. Aubin, J. A. Behr, E. Gomez, G. Gwinner, L. A. Orozco, M. R. Pearson, and G. D. Sprouse (FrPNC collaboration), Phys. Rev. Lett. **115**, 042501 (2015).

[6] K. Blaum, J. Dilling, and W. Nörtershäuser, Phys. Scripta **T152**, 014017 (2013).

[7] J. Papuga, M. L. Bissell, K. Kreim, C. Barbieri, K. Blaum, M. De Rydt, T. Duguet, R. F. Garcia Ruiz, H. Heylen, M. Kowalska, R. Neugart, G. Neyens, W. Nörtershäuser, M. M. Rajabali, R. Sánchez, N. Smirnova, V. Somà, and D. T. Yordanov, Phys. Rev. C **90**, 034321 (2014).

[8] A. Nieminen, P. Campbell, J. Billowes, D. H. Forest, J. A. R. Griffith, J. Huikari, A. Jokinen, I. D. Moore, R. Moore, G. Tungate, and J. Äystö, Phys. Rev. Lett. **88**, 094801 (2002).

[9] A. Voss, M. R. Pearson, J. Billowes, F. Buchinger, B. Cheal, J. E. Crawford, A. A. Kwiatkowski, C. D. P. Levy, and O. Shelbaya, Phys. Rev. Lett. **111**, 122501 (2013).

[10] K. Minamisono, P. Mantica, A. Klose, S. Vinnikova, A. Schneider, B. Johnson, and B. Barquest, Nuclear Instruments and Methods in Physics Research Section A: Accelerators, Spectrometers, Detectors and Associated Equipment **709**, 85 (2013).

[11] H. Iimura, M. Koizumi, M. Miyabe, M. Oba, T. Shibata, N. Shinohara, Y. Ishida, T. Horiguchi, and H. A. Schuessler, Phys. Rev. C **68**, 054328 (2003).

[12] K. Blaum, W. Geithner, J. Lassen, P. Lievens, K. Marinova, and R. Neugart, Nuclear Physics A **799**, 30 (2008).

[13] B. Cheal, E. Mané, J. Billowes, M. L. Bissell, K. Blaum, B. A. Brown, F. C. Charlwood, K. T. Flanagan, D. H. Forest, C. Geppert, M. Honma, A. Jokinen, M. Kowalska, A. Krieger, J. Krämer, I. D. Moore, R. Neugart, G. Neyens, W. Nörtershäuser, M. Schug, H. H. Stroke, P. Vingerhoets, D. T. Yordanov, and M. Žáková, Phys. Rev. Lett. **104**, 252502 (2010).

[14] V. N. Fedosseev, Y. Kudryavtsev, and V. I. Mishin, Phys. Scripta **85**, 058104 (2012).

[15] H. D. Witte, A. Andreyev, N. Barré, M. Bender, T. Cocolios, S. Dean, D. Fedorov, V. Fedoseyev, L. Fraile, S. Franchoo, V. Hellemans, P. Heenen, K. Heyde, G. Huber, M. Huyse, H. Jeppessen, U. Köster, P. Kunz, S. Lesher, B. Marsh, I. Mukha, B. Roussière, J. Sauvage, M. Seliverstov, I. Stefanescu, E. Tengborn, K. V. de Vel, J. V. de Walle, P. V. Duppen, and Y. Volkov, Phys. Rev. Lett. **98**, 112502 (2007).

[16] U. Köster, N. J. Stone, K. T. Flanagan, J. R. Stone, V. N. Fedosseev, K. L. Kratz, B. A.

Marsh, T. Materna, L. Mathieu, P. L. Molkanov, M. D. Seliverstov, O. Serot, A. M. Sjödin, and Y. M. Volkov, Phys. Rev. C **84**, 034320 (2011).

[17] R. Ferrer, N. Bree, T. Cocolios, I. Darby, H. D. Witte, W. Dexters, J. Diriken, J. Elseviers, S. Franchoo, M. Huyse, N. Kesteloot, Y. Kudryavtsev, D. Pauwels, D. Radulov, T. Roger, H. Savajols, P. V. Duppen, and M. Venhart, Phys. Lett. B **728**, 191 (2014).

[18] Y. Kudryavtsev, R. Ferrer, M. Huyse, P. V. den Bergh, and P. V. Duppen, Nucl.Nucl. Instrum. Meth. B **297**, 7 (2013).

[19] Y. A. Kudriavtsev and V. S. Letokhov, Appl. Phys. B **29**, 219 (1982).

[20] C. Schulz, E. Arnold, W. Borchers, W. Neu, R. Neugart, M. Neuroth, E. W. Otten, M. Scherf, K. Wendt, P. Lievens, Y. A. Kudryavtsev, V. S. Letokhov, V. I. Mishin, and V. V. Petrunin, J. Phys. B: At. Mol. Opt. Phys. **24**, 4831 (1991).

[21] K. T. Flanagan, K. M. Lynch, J. Billowes, M. L. Bissell, I. Budinčević, T. E. Cocolios, R. P. de Groote, S. D. Schepper, V. N. Fedosseev, S. Franchoo, R. F. Garcia Ruiz, H. Heylen, B. A. Marsh, G. Neyens, T. J. Procter, R. E. Rossel, S. Rothe, I. Strashnov, H. H. Stroke, and K. D. A. Wendt, Phys. Rev. Lett. **111**, 212501 (2013).

[22] S. Rothe, V. N. Fedosseev, T. Kron, B. A. Marsh, R. E. Rossel, and K. D. A. Wendt, Nucl. Instrum. Meth. B **317**, 561 (2013).

[23] V. Meyer, S. N. Bagayev, P. E. G. Baird, P. Bakule, M. G. Boshier, A. Breitrück, S. L. Cornish, S. Dychkov, G. H. Eaton, A. Grossmann, D. Hübl, V. W. Hughes, K. Jungmann, I. C. Lane, Y.-W. Liu, D. Lucas, Y. Matyugin, J. Merkel, G. zu Putlitz, I. Reinhard, P. G. H. Sandars, R. Santra, P. V. Schmidt, C. A. Scott, W. T. Toner, M. Towrie, K. Träger, L. Willmann, and V. Yakhontov, Phys. Rev. Lett. **84**, 1136 (2000).

[24] K. S. E. Eikema, W. Ubachs, W. Vassen, and W. Hogervorst, Phys. Rev. A **55**, 1866 (1997).

[25] M. Hori and A. Dax, Opt. Lett. **34**, 1273 (2009).

[26] M. Hori, A. Sótér, D. Barna, A. Dax, R. Hayano, S. Friedreich, B. Juhász, T. Pask, E. Widmann, D. Horváth, *et al.*, Nature **475**, 484 (2011).

[27] M. Reponen, I. Moore, T. Kessler, I. Pohjalainen, S. Rothe, and V. Sonnenschein, Eur. Phys. J. A **48**, 45 (2012), 10.1140/epja/i2012-12045-2.

[28] J. Sell, K. Gulyuz, and G. Sprouse, Review of Scientific Instruments **80**, 123108 (2009).

[29] N. Vitanov, B. Shore, L. Yatsenko, K. Böhmer, T. Halfmann, T. Rickes, and K. Bergmann, Opt.Commun. **199**, 117 (2001).

[30] T. Halfmann, T. Rickes, N. Vitanov, and K. Bergmann, Opt.Commun. **220**, 353 (2003).

[31] R. de Groote, G. Neyens, and K. Flanagan, *Modeling and simulation of two-step resonance ionization processes using CW and pulsed lasers*, Master's thesis, Leuven U. (2013), presented 31 Jun 2013.

[32] P. A. Butler, Reviews of Modern Physics **68**, 349 (1996).

[33] L. P. Gaffney, P. A. Butler, M. Scheck, A. B. Hayes, F. Wenander, M. Albers, B. Bastin, C. Bauer, A. Blazhev, S. Bönig, N. Bree, J. Cederkll, T. Chupp, D. Cline, T. E. Cocolios, T. Davinson, H. D. Witte, J. Diriken, T. Grahn, A. Herzan, M. Huyse, D. G. Jenkins, D. T. Joss, N. Kesteloot, J. Konki, M. Kowalczyk, T. Kröll, E. Kwan, R. Lutter, K. Moschner, P. Napiorkowski, J. Pakarinen, M. Pfeiffer, D. Radeck, P. Reiter, K. Reynders, S. V. Rigby, L. M. Robledo, M. Rudigier, S. Sambi, M. Seidlitz, B. Siebeck, T. Stora, P. Thoele, P. V. Duppen, M. J. Vermeulen, M. von Schmid, D. Voulot, N. Warr, K. Wimmer, K. Wrzosek-Lipska, C. Y. Wu, and M. Zielinska, Nature **497**, 199 (2013).

[34] D. A. Fink, T. E. Cocolios, A. N. Andreyev, S. Antalic, A. E. Barzakh, B. Bastin, D. V. Fedorov, V. N. Fedosseev, K. T. Flanagan, L. Ghys, A. Gottberg, M. Huyse, N. Imai, T. Kron, N. Lecesne, K. M. Lynch, B. A. Marsh, D. Pauwels, E. Rapisarda, S. D. Richter, R. E. Rossel, S. Rothe, M. D. Seliverstov, A. M. Sjödin, C. Van Beveren, P. Van Duppen, and K. D. A. Wendt, Phys. Rev. X **5**, 011018 (2015).

[35] R. K. Sheline, Phys. Lett. B **197**, 500 (1987).

[36] A. Coc, C. Thibault, F. Touchard, H. Duong, P. Juncar, S. Liberman, J. Pinard, J. Lermé, J. Vialle, S. Büttgenbach, A. Mueller, and A. Pesnelle, Phys. Lett. B **163**, 66 (1985).

[37] H. T. Duong, P. Juncar, S. Liberman, A. C. Mueller, R. Neugart, E. W. Otten, B. Peuse, J. Pinard, H. H. Stroke, C. Thibault, F. Touchard, J. L. Vialle, K. Wendt, and I. Collaboration, Europhys. Lett. **3**, 175 (1987).

[38] I. Budinčević, J. Billowes, M. L. Bissell, T. E. Cocolios, R. P. de Groote, S. D. Schepper, V. N. Fedosseev, K. T. Flanagan, S. Franchoo, R. F. Garcia Ruiz, H. Heylen, K. M. Lynch, B. A. Marsh, G. Neyens, T. J. Procter, R. E. Rossel, S. Rothe, I. Strashnov, H. H. Stroke, and K. D. A. Wendt, Phys. Rev. C **90**, 014317 (2014).

[39] K. M. Lynch, J. Billowes, M. L. Bissell, I. Budinčević, T. E. Cocolios, R. P. de Groote, S. De Schepper, V. N. Fedosseev, K. T. Flanagan, S. Franchoo, R. F. Garcia Ruiz, H. Heylen, B. A. Marsh, G. Neyens, T. J. Procter, R. E. Rossel, S. Rothe, I. Strashnov, H. H. Stroke,

Bibliography

[1] T. E. Cocolios, H. H. Al Suradi, J. Billowes, I. Budinčević, R. P. de Groote, S. De Schepper, V. N. Fedosseev, K. T. Flanagan, S. Franchoo, R. F. Garcia Ruiz, H. Heylen, F. Le Blanc, K. M. Lynch, B. A. Marsh, P. J. R. Mason, G. Neyens, J. Papuga, T. J. Procter, M. M. Rajabali, R. E. Rossel, S. Rothe, G. S. Simpson, A. J. Smith, I. Strashnov, H. H. Stroke, D. Verney, P. M. Walker, K. D. A. Wendt, and R. T. Wood, "The Collinear Resonance Ionization Spectroscopy (CRIS) experimental setup at CERN-ISOLDE," *Nucl. Instrum. & Methods B*, vol. 317, pp. 565–569, Dec. 2013.

[2] K. T. Flanagan, K. M. Lynch, J. Billowes, M. L. Bissell, I. Budinčević, T. E. Cocolios, R. P. de Groote, S. De Schepper, V. N. Fedosseev, S. Franchoo, R. F. Garcia Ruiz, H. Heylen, B. A. Marsh, G. Neyens, T. J. Procter, R. E. Rossel, S. Rothe, I. Strashnov, H. H. Stroke, and K. D. A. Wendt, "Collinear Resonance Ionization Spectroscopy of Neutron-Deficient Francium Isotopes," *Phys. Rev. Letters*, vol. 111, p. 212501, Nov. 2013.

[3] K. M. Lynch, J. Billowes, M. L. Bissell, I. Budinčević, T. E. Cocolios, R. P. de Groote, S. De Schepper, V. N. Fedosseev, K. T. Flanagan, S. Franchoo, R. F. Garcia Ruiz, H. Heylen, B. A. Marsh, G. Neyens, T. J. Procter, R. E. Rossel, S. Rothe, I. Strashnov, H. H. Stroke, and K. D. A. Wendt, "Decay-Assisted Laser Spectroscopy of Neutron-Deficient Francium," *Physical Review X*, vol. 4, p. 011055, Mar. 2014.

[4] K. M. Lynch, *Laser assisted nuclear decay spectroscopy: A new method for studying neutron-deficient francium.* PhD thesis, The University of Manchester, Aug 2013. Presented 19 Sep 2013.

[5] I. Budinčević, J. Billowes, M. L. Bissell, T. E. Cocolios, R. P. de Groote, S. De Schepper, V. N. Fedosseev, K. T. Flanagan, S. Franchoo, R. F. Garcia Ruiz, H. Heylen, K. M. Lynch, B. A. Marsh, G. Neyens, T. J.

Procter, R. E. Rossel, S. Rothe, I. Strashnov, H. H. Stroke, and K. D. A. Wendt, "Laser spectroscopy of francium isotopes at the borders of the region of reflection asymmetry," *Phys. Rev. C*, vol. 90, p. 014317, July 2014.

[6] R. P. de Groote, I. Budinčević, J. Billowes, M. L. Bissell, T. E. Cocolios, G. Farooq-smith, V. N. Fedosseev, K. T. Flanagan, S. Franchoo, R. F. Garcia Ruiz, H. Heylen, R. Li, K. M. Lynch, B. A. Marsh, G. Neyens, R. E. Rossel, S. Rothe, H. H. Stroke, K. D. A. Wendt, S. G. Wilkins, and X. Yang, "Use of a Continuous Wave Laser and Pockells Cell for Sensitive High-Resolution Collinear Resonance Ionization Spectroscopy," 2015. Accepted for publication in *Phys. Rev. Letters*.

[7] L. P. Gaffney, P. A. Butler, M. Scheck, A. B. Hayes, F. Wenander, M. Albers, B. Bastin, C. Bauer, A. Blazhev, S. Bönig, N. Bree, J. Cederkäll, T. Chupp, D. Cline, T. E. Cocolios, T. Davinson, H. De Witte, J. Diriken, T. Grahn, A. Herzan, M. Huyse, D. G. Jenkins, D. T. Joss, N. Kesteloot, J. Konki, M. Kowalczyk, T. Kröll, E. Kwan, R. Lutter, K. Moschner, P. Napiorkowski, J. Pakarinen, M. Pfeiffer, D. Radeck, P. Reiter, K. Reynders, S. V. Rigby, L. M. Robledo, M. Rudigier, S. Sambi, M. Seidlitz, B. Siebeck, T. Stora, P. Thoele, P. Van Duppen, M. J. Vermeulen, M. von Schmid, D. Voulot, N. Warr, K. Wimmer, K. Wrzosek-Lipska, C. Y. Wu, and M. Zielinska, "Studies of pear-shaped nuclei using accelerated radioactive beams.," *Nature*, vol. 497, pp. 199–204, May 2013.

[8] G. A. Leander and Y. S. Chen, "Reflection-asymmetric rotor model of odd A 219–229 nuclei," *Phys. Rev. C*, vol. 37, no. 6, pp. 2744–2778, 1988.

[9] W. Nazarewicz, P. Olanders, I. Ragnarsson, J. Dudek, G. Leander, P. Möller, and E. Ruchowsa, "Analysis of octupole instability in medium-mass and heavy nuclei," *Nucl. Phys. A*, vol. 429, pp. 269–295, Nov. 1984.

[10] R. Sheline, "Definition of the actinide region of static quadrupole-octupole deformation," *Phys. Lett. B*, vol. 197, no. 4, pp. 3–7, 1987.

[11] G. Leander and R. Sheline, "Intrinsic reflection asymmetry in odd- A nuclei," *Nucl. Phys. A*, vol. 413, pp. 375–415, 1984.

[12] B. Cheal and K. T. Flanagan, "Progress in laser spectroscopy at radioactive ion beam facilities," *J. Phys. G Nucl. Part. Phys.*, vol. 37, p. 113101, Nov. 2010.

[13] E. Mané, J. Billowes, K. Blaum, P. Campbell, B. Cheal, P. Delahaye, K. T. Flanagan, D. H. Forest, H. Franberg, C. Geppert, T. Giles, A. Jokinen, M. Kowalska, R. Neugart, G. Neyens, W. Nörtershäuser, I. Podadera,

G. Tungate, P. Vingerhoets, and D. T. Yordanov, "An ion cooler-buncher for high-sensitivity collinear laser spectroscopy at ISOLDE," *Eur. Phys. J. A*, vol. 42, pp. 503–507, June 2009.

[14] `https://github.com/rubendegroote/Networked-Data-Acquisition/tree/v0.1`.

[15] S. Falke, E. Tiemann, C. Lisdat, H. Schnatz, and G. Grosche, "Transition frequencies of the D lines of ^{39}K, ^{40}K, and ^{41}K measured with a femtosecond laser frequency comb," *Phys. Rev. A*, vol. 74, no. 3, pp. 1–9, 2006.

[16] R. Casten, *Nuclear Structure From A Simple Perspective*. Oxford University Press Inc, 1990.

[17] P. A. Butler and W. Nazarewicz, "Intrinsic reflection asymmetry in atomic nuclei," *Reviews of Modern Physics*, vol. 68, no. 2, pp. 349–421, 1996.

[18] C. F. Liang, P. Paris, J. Kvasil, and R. K. Sheline, "219Fr, a transitional reflection asymmetric nucleus.," *Phys. Rev. C: Nuclear physics*, vol. 44, pp. 676–688, Aug. 1991.

[19] `https://oraweb.cern.ch/pls/isolde/yield?v_url=query_tgt&v_z=87`.

[20] A. Unsöld, *Physik der Sternatmosphären*. Springer Verlag, Berlin: 90-91, 1968.

[21] J. Papuga, M. L. Bissell, K. Kreim, K. Blaum, B. A. Brown, M. De Rydt, R. F. Garcia Ruiz, H. Heylen, M. Kowalska, R. Neugart, G. Neyens, W. Nörtershäuser, T. Otsuka, M. M. Rajabali, R. Sánchez, Y. Utsuno, and D. T. Yordanov, "Spins and Magnetic Moments of ^{49}K and ^{51}K: Establishing the 1/2^{+} and 3/2^{+} Level Ordering Beyond N=28," *Phys. Rev. Lett.*, vol. 110, p. 172503, Apr. 2013.

[22] V. A. Dzuba, W. R. Johnson, and M. S. Safronova, "Calculation of isotope shifts for cesium and francium," *Phys. Rev. A*, vol. 72, p. 022503, Aug. 2005.

[23] D. Decman, H. Grawe, H. Kluge, K. Maier, A. Maj, M. Menningen, N. Roy, and W. Wiegner, "In-beam α-, e- and γ-spectroscopy of 215Fr," *Nucl. Phys. A*, vol. 419, no. 1, pp. 163–186, 1984.

[24] A. Abdul-Hadi, V. Barci, B. Weiss, H. Maria, G. Ardisson, M. Hussonnois, and O. Constantinescu, "^{223}Ra levels fed in the ^{223}Fr β decay," *Phys. Rev. C*, vol. 47, pp. 94–109, Jan 1993.

[25] S. Liberman, J. Pinard, H. Duong, P. Juncar, P. Pillet, J.-L. Vialle, P. Jacquinot, F. Touchard, S. Büttgenbach, C. Thibault, M. de Saint-Simon, R. Klapisch, A. Pesnelle, and G. Huber, "Laser optical spectroscopy on francium D_{2} resonance line," *Phys. Rev. A*, vol. 22, pp. 2732–2737, Dec. 1980.

[26] S. Liberman, J. Pinard, H. Duong, P. Juncar, J.-L. Vialle, P. Jacquinot, G. Huber, F. Touchard, S. B uttgenbach, A. Pesnelle, C. Thibault, and R. Klapisch, "," *C.R. Acad. Sci. B*, vol. 286, p. 253, Feb. 1978.

[27] N. Bendali, H. Duong, P. Juncar, S. Liberman, J. Pinard, J.-M. Saint-Jalm, J.-L. Vialle, S. B uttgenbach, C. Thibault, F. Touchard, A. Pesnelle, A. Mueller, and C. ISOLDE, "," *C.R. Acad. Sci. B*, vol. 299, p. 1157, Feb. 1984.

[28] A. Coc, C. Thibault, F. Touchard, H. Duong, P. Juncar, S. Liberman, J. Pinard, J. Lermé, J. Vialle, S. Büttgenbach, A. Mueller, and A. Pesnelle, "Hyperfine structures and isotope shifts of ; Possible evidence of octupolar deformation," *Phys. Lett. B*, vol. 163, pp. 66–70, Nov. 1985.

[29] A. Coc, C. Thibault, F. Touchard, H. Duong, P. Juncar, S. Liberman, J. Pinard, M. Carre, J. Lerme, J. Vialle, S. Buttgenbach, A. Mueller, and A. Pesnelle, "Isotope shifts, spins and hyperfine structures of 118,146Cs and of some francium isotopes," *Nucl. Phys. A*, vol. 468, pp. 1–10, June 1987.

[30] W. Borchers, R. Neugart, E. W. Otten, H. T. Duong, G. Ulm, and K. Wendt, "Hyperfine structure and isotope shift investigations in202–222Rn for the study of nuclear structure beyond Z=82," *Hyperfine Interact.*, vol. 34, pp. 25–29, Mar. 1987.

[31] S. Ahmad, W. Klempt, R. Neugart, E. Otten, P.-G. Reinhard, G. Ulm, and K. Wendt, "Mean square charge radii of radium isotopes and octupole deformation in the 220–228Ra region," *Nucl. Phys. A*, vol. 483, pp. 244–268, June 1988.

[32] C. F. LIANG, P. PARIS, and R. K. SHELINE, "REFLECTION ASYMMETRY IN THE TRANSITIONAL ODD-ODD NUCLEUS 220 Fr," *Int. J. Mod. Phys. E*, vol. 01, pp. 363–377, June 1992.

[33] R. K. Sheline, "Octupole deformation in 221fr," *Physics Letters B*, vol. 205, no. 1, pp. 11 – 15, 1988.

[34] C. LIANG, A. PÉGHAIRE, and R. SHELINE, "OCTUPOLE DEFORMATION IN 221 Fr; E1 TRANSITION RATES," *Mod. Phys. Lett. A*, vol. 05, pp. 1243–1250, July 1990.

[35] W. Kurcewicz, G. Lø vhøiden, T. Thorsteinsen, M. Borge, D. Burke, M. Cronqvist, H. Gabelmann, H. Gietz, P. Hill, N. Kaffrell, R. Naumann, K. Nybø, G. Nyman, and J. Rogowski, "The nuclear structure of 223Fr," *Nuclear Physics A*, vol. 539, pp. 451–477, Mar. 1992.

[36] D. Burke, W. Kurcewicz, G. Lø vhøiden, M. Borge, M. Cronqvist, H. Gabelmann, H. Gietz, P. Hill, N. Kaffrell, S. Mattsson, R. Naumann, K. Nybø, G. Nyman, J. Rogowski, G. Struble, and T. Thorsteinsen, "Search for stable octupole deformation in 225Fr," *Nuclear Physics A*, vol. 612, pp. 91–142, Jan. 1997.

[37] W. Kurcewicz, I. Grant, K. Gulda, A. Aas, J. Billowes, M. Borge, D. Burke, P. Butler, J. Cocks, B. Fogelberg, S. Freeman, G. Jones, E. Hagebø, P. Hoff, J. Hø nsi, A. Lindroth, G. Lø vhøiden, H. Mach, T. Martinez, R. Naumann, K. Nybø, G. Nyman, H. Ravn, B. Rubio, J. Simpson, A. Smith, J. Smith, K. Steffensen, J. Tain, O. Tengblad, and T. Thorsteinsen, "The nuclear structure of 227Fr," *Nucl. Phys. A*, vol. 621, pp. 827–852, Aug. 1997.

[38] K. Lee and D. Inglis, "Stability of Pear-Shaped Nuclear Deformations," *Phys. Rev.*, vol. 108, pp. 774–778, Nov. 1957.

[39] E. G. Adelberger and W. C. Haxion, "Parity Violation in the Nucleon-Nucleon Interaction," *Annu. Rev. Nucl. Part. Sci.*, vol. 35, pp. 501–558, Dec. 1985.

[40] E. Gomez, S. Aubin, G. D. Sprouse, L. a. Orozco, and D. P. Demille, "Measurement method for the nuclear anapole moment of laser-trapped alkali-metal atoms," *Phys. Rev. A - At. Mol. Opt. Phys.*, vol. 75, no. 3, pp. 1–10, 2007.

[41] M. Tandecki, J. Zhang, R. Collister, S. Aubin, J. a. Behr, E. Gomez, G. Gwinner, L. a. Orozco, and M. R. Pearson, "Commissioning of the Francium Trapping Facility at TRIUMF," *J. Instrum.*, vol. 8, no. 12, pp. P12006–P12006, 2013.

[42] M. K. Craddock, K. L. Erdman, and J. T. Sample, "Basic and applied research at the TRIUMF meson factory," *Nature*, vol. 270, pp. 671–676, Dec. 1977.

[43] C. Maples, "Nuclear data sheets for A = 223," *Nucl. Data Sheets*, vol. 22, pp. 243–274, Oct. 1977.

[44] C. Liang, P. Paris, and R. Sheline, "Shell model level structure inˆ{215} At," *Phys. Rev. C*, vol. 47, no. 4, pp. 1801–1803, 1993.

[45] R. K. Sheline, C. F. Liang, P. Paris, and J. Kvasil, "The spestroscopy and structure of odd-A Fr isotopes withA= 213–225," *Czechoslovak Journal of Physics*, vol. 50, no. 8, 2000.

[46] E. W. Otten, in *Treatise on Heavy Ion Science*, vol. 8. Boston, MA: Springer US, 1989.

[47] J. Billowes and P. Campbell, "High-resolution laser spectroscopy for the study of nuclear sizes and shapes," *J. Phys. G Nucl. Part. Phys.*, vol. 21, pp. 707–739, June 1995.

[48] T. Sonoda, T. Cocolios, J. Gentens, M. Huyse, O. Ivanov, Y. Kudryavtsev, D. Pauwels, P. Van den Bergh, and P. Van Duppen, "The Laser Ion Source Trap (LIST) coupled to a gas cell catcher," *Nucl. Instruments Methods Phys. Res. Sect. B Beam Interact. with Mater. Atoms*, vol. 267, pp. 2918–2926, Sept. 2009.

[49] R. Neugart, "Laser spectroscopy on mass-separated radioactive beams," *Nucl. Instruments Methods Phys. Res.*, vol. 186, pp. 165–175, July 1981.

[50] J. Papuga, M. L. Bissell, K. Kreim, C. Barbieri, K. Blaum, M. De Rydt, T. Duguet, R. F. Garcia Ruiz, H. Heylen, M. Kowalska, R. Neugart, G. Neyens, W. Nörtershäuser, M. M. Rajabali, R. Sánchez, N. Smirnova, V. Somà, and D. T. Yordanov, "Shell structure of potassium isotopes deduced from their magnetic moments," *Phys. Rev. C*, vol. 90, p. 034321, Sep 2014.

[51] H. De Witte, A. Andreyev, N. Barré, M. Bender, T. Cocolios, S. Dean, D. Fedorov, V. Fedoseyev, L. Fraile, S. Franchoo, V. Hellemans, P. Heenen, K. Heyde, G. Huber, M. Huyse, H. Jeppessen, U. Köster, P. Kunz, S. Lesher, B. Marsh, I. Mukha, B. Roussière, J. Sauvage, M. Seliverstov, I. Stefanescu, E. Tengborn, K. Van de Vel, J. Van de Walle, P. Van Duppen, and Y. Volkov, "Nuclear Charge Radii of Neutron-Deficient Lead Isotopes Beyond N=104 Midshell Investigated by In-Source Laser Spectroscopy," *Phys. Rev. Lett.*, vol. 98, p. 112502, Mar. 2007.

[52] T. E. Cocolios, W. Dexters, M. D. Seliverstov, A. N. Andreyev, S. Antalic, A. E. Barzakh, B. Bastin, J. Büscher, I. G. Darby, D. V. Fedorov, V. N. Fedosseyev, K. T. Flanagan, S. Franchoo, S. Fritzsche, G. Huber, M. Huyse, M. Keupers, U. Köster, Y. Kudryavtsev, E. Mané, B. A. Marsh, P. L. Molkanov, R. D. Page, A. M. Sjoedin, I. Stefan, J. Van de Walle, P. Van Duppen, M. Venhart, S. G. Zemlyanoy, M. Bender, and P.-H. Heenen, "Early Onset of Ground State Deformation in Neutron Deficient Polonium Isotopes," *Phys. Rev. Lett.*, vol. 106, p. 052503, Feb. 2011.

[53] M. D. Seliverstov, A. N. Andreyev, N. Barré, A. E. Barzakh, S. Dean, H. De Witte, D. V. Fedorov, V. N. Fedoseyev, L. M. Fraile, S. Franchoo, J. Genevey, G. Huber, M. Huyse, U. Köster, P. Kunz, S. R. Lesher, B. A. Marsh, I. Mukha, B. Roussière, J. Sauvage, I. Stefanescu, K. Van de Vel, P. Van Duppen, and Y. M. Volkov, "Charge radii and magnetic moments of odd- A 183-189Pb isotopes," *Eur. Phys. J. A*, vol. 41, pp. 315–321, July 2009.

[54] M. Seliverstov, T. Cocolios, W. Dexters, A. Andreyev, S. Antalic, A. Barzakh, B. Bastin, J. Büscher, I. Darby, D. Fedorov, V. Fedoseyev, K. Flanagan, S. Franchoo, S. Fritzsche, G. Huber, M. Huyse, M. Keupers, U. Köster, Y. Kudryavtsev, B. Marsh, P. Molkanov, R. Page, A. S. din, I. Stefan, J. Van de Walle, P. Van Duppen, M. Venhart, and S. Zemlyanoy, "Charge radii of odd-A 191–211Po isotopes," *Phys. Lett. B*, vol. 719, pp. 362–366, Feb. 2013.

[55] V. N. Fedosseev, Y. Kudryavtsev, and V. I. Mishin, "Resonance laser ionization of atoms for nuclear physics," *Phys. Scr.*, vol. 85, p. 058104, May 2012.

[56] Y. Kudryavtsev, R. Ferrer, M. Huyse, P. Van den Bergh, and P. Van Duppen, "The in-gas-jet laser ion source: Resonance ionization spectroscopy of radioactive atoms in supersonic gas jets," *Nucl. Instruments Methods Phys. Res. Sect. B Beam Interact. with Mater. Atoms*, vol. 297, pp. 7–22, Feb. 2013.

[57] H. Kopfermann, *Nuclear Moments*. Academic Press, New York, 1958.

[58] M. De Rydt. PhD thesis, KU Leuven, 2010. Available at https://lirias.kuleuven.be/handle/123456789/256023.

[59] C. Schwartz, "Theory of Hyperfine Structure," *Physical Review*, vol. 97, pp. 380–395, Jan. 1955.

[60] B. Castel and I. S. Towner, *Modern Theories of Nuclear Moments*. Clarendon Press, Oxford, 1990.

[61] G. Neyens, "Nuclear magnetic and quadrupole moments for nuclear structure research on exotic nuclei," *Reports on Progress in Physics*, vol. 66, pp. 633–689, Apr. 2003.

[62] K. L. G. Heyde, *The Nuclear Shell Model*. Springer, Berlin Heidelberg, 1994.

[63] A. Bohr and V. F. Weisskopf, "The influence of nuclear structure on the hyperfine structure of heavy elements," *Phys. Rev.*, vol. 77, no. 1, pp. 94–98, 1950.

[64] S. Büttgenbach, "Magnetic hyperfine anomalies," *Hyperfine Interact.*, vol. 20, pp. 1–64, July 1984.

[65] J. Rosenthal and G. Breit, "The Isotope Shift in Hyperfine Structure," *Phys. Rev.*, vol. 41, no. 4, pp. 459–470, 1932.

[66] A.-M. Må rtensson Pendrill, "Magnetic Moment Distributions in Tl Nuclei," *Phys. Rev. Lett.*, vol. 74, pp. 2184–2187, Mar. 1995.

[67] J. Zhang, M. Tandecki, R. Collister, S. Aubin, J. a. Behr, E. Gomez, G. Gwinner, L. a. Orozco, M. R. Pearson, and G. D. Sprouse, "Hyperfine Anomalies in Fr: Boundaries of the Spherical Single Particle Model," *Phys. Rev. Lett.*, vol. 115, no. 4, p. 042501, 2015.

[68] W. H. King, *Isotope Shifts in Atomic Spectra*. Plenum Press, New York, 1984.

[69] K. Heilig and A. Steudel, "Changes in mean-square nuclear charge radii from optical isotope shifts," *At. Data Nucl. Data Tables*, vol. 14, pp. 613–638, Nov. 1974.

[70] W. Nörtershäuser, R. Sánchez, G. Ewald, A. Dax, J. Behr, P. Bricault, B. A. Bushaw, J. Dilling, M. Dombsky, G. W. F. Drake, S. Götte, H.-J. Kluge, T. Kühl, J. Lassen, C. D. P. Levy, K. Pachucki, M. Pearson, M. Puchalski, A. Wojtaszek, Z.-C. Yan, and C. Zimmermann, "Isotope-shift measurements of stable and short-lived lithium isotopes for nuclear-charge-radii determination," *Phys. Rev. A*, vol. 83, p. 012516, Jan. 2011.

[71] B. Cheal, T. E. Cocolios, and S. Fritzsche, "Laser spectroscopy of radioactive isotopes: Role and limitations of accurate isotope-shift calculations," *Phys. Rev. A*, vol. 86, p. 042501, Oct. 2012.

[72] W. H. KING, "Comments on the Article "Peculiarities of the Isotope Shift in the Samarium Spectrum"," *J. Opt. Soc. Am.*, vol. 53, p. 638, May 1963.

[73] J. Äystö, "CERN's longest serving experimental facility," *Phys. Rep.*, vol. 403-404, pp. 459–469, Dec. 2004.

[74] `http://home.web.cern.ch/about/accelerators/antiproton-decelerator`.

[75] `http://home.web.cern.ch/about/accelerators/cern-neutrinos-gran-sasso`.

[76] `http://home.web.cern.ch/about/experiments/ntof`.

[77] http://home.web.cern.ch/about/accelerators/compact-linear-collider.

[78] http://home.web.cern.ch/topics/large-hadron-collider.

[79] http://home.web.cern.ch/about/accelerators.

[80] http://home.web.cern.ch/about/accelerators/proton-synchrotron-booster.

[81] A. Herlert, "The ISOLDE Facility," *Nucl. Phys. News*, vol. 20, no. 4, 2010.

[82] S. V. Andreev, V. S. Letokhov, and V. I. Mishin, "Laser resonance photoionization spectroscopy of rydberg levels in fr," *Phys. Rev. Lett.*, vol. 59, pp. 1274–1276, Sep 1987.

[83] T. Giles, R. Catherall, V. Fedosseev, U. Georg, E. Kugler, J. Lettry, and M. Lindroos, "The high resolution spectrometer at ISOLDE," *Nucl. Instruments Methods Phys. Res. Sect. B Beam Interact. with Mater. Atoms*, vol. 204, pp. 497–501, May 2003.

[84] P. V. Duppen, "Isotope separation on line and post acceleration," *Euroschool Lect. Phys. with Exot. Beams ...*, vol. 77, pp. 37–77, 2006.

[85] E. Kugler, "The ISOLDE facility," vol. 129, pp. 23–42, 2000.

[86] C. Schulz, E. Arnold, W. Borchers, W. Neu, R. Neugart, M. Neuroth, E. W. Otten, M. Scherf, K. Wendt, P. Lievens, Y. A. Kudryavtsev, V. S. Letokhov, V. I. Mishin, and V. V. Petrunin, "Resonance ionization spectroscopy on a fast atomic ytterbium beam," *J. Phys. B At. Mol. Opt. Phys.*, vol. 24, pp. 4831–4844, Nov. 1991.

[87] I. Podadera Aliseda, T. Fritioff, T. Giles, A. Jokinen, M. Lindroos, and F. Wenander, "Design of a second generation RFQ Ion Cooler and Buncher (RFQCB) for ISOLDE," *Nucl. Phys. A*, vol. 746, pp. 647–650, Dec. 2004.

[88] *Atomic Physics*. Foot, Christopher J.: Oxford University Press, 2005.

[89] S. Aubin, E. Gomez, L. A. Orozco, and G. D. Sprouse, "Lifetimes of the 9s and 8p levels of atomic francium," *Physical Review A - Atomic, Molecular, and Optical Physics*, vol. 70, no. 4, pp. 1–11, 2004.

[90] J. Billowes, F. Le Blanc, M. L. Bissell, P. Campbell, B. Cheal, K. Flanagan, D. Forest, E. Mane, G. Neyens, M. De Rydt, H. H. Stroke, B. Tastet, G. Tungate, and P. Vingerhoets, "Collinear resonant ionization laser spectroscopy of rare francium isotopes.," Tech. Rep. CERN-INTC-2008-010. INTC-P-240, CERN, Geneva, Jan 2008.

[91] K. T. Flanagan, K. M. Lynch, J. Billowes, M. L. Bissell, I. Budinčević, T. E. Cocolios, T. D. Goodacre, R. P. de Groote, V. N. Fedosseev, S. Franchoo, R. F. Garcia Ruiz, H. Heylen, T. Kron, B. A. Marsh, G. Neyens, T. J. Procter, R. E. Rossel, S. Rothe, I. Strashnov, H. H. Stroke, and K. D. A. Wendt, "Collinear resonance ionization spectroscopy of rare francium isotopes," Tech. Rep. CERN-INTC-2014-020. INTC-P-240-ADD-1, CERN, Geneva, Jan 2014.

[92] A. Andrei. (private communication).

[93] `http://home.web.cern.ch/about/accelerators/synchrocyclotron`.

[94] S. Rothe, B. A. Marsh, C. Mattolat, V. N. Fedosseev, and K. D. A. Wendt, "A complementary laser system for ISOLDE RILIS," *Journal of Physics: Conference Series*, vol. 312, p. 052020, Sept. 2011.

[95] O. Svelto, *Principles of Lasers*. Springer, 1998.

[96] `http://www.rp-photonics.com/encyclopedia.html`.

[97] K. M. Lynch, M. M. Rajabali, H. Aghaei-Khozani, J. Billowes, M. L. Bissell, F. Le Blanc, B. Cheal, T. E. Cocolios, S. D. Schepper, K. Dewolf, K. T. Flanagan, M. Hori, T. Kobayashi, B. A. Marsh, G. Neyens, J. Papuga, T. J. Procter, S. Rothe, G. S. Simpson, A. J. Smith, H. H. Stroke, and K. D. A. Wendt, "Laser assisted decay spectroscopy at the CRIS beam line at ISOLDE," *Journal of Physics: Conference Series*, vol. 381, p. 012128, Sept. 2012.

[98] M. M. Rajabali, K. M. Lynch, T. E. Cocolios, J. Billowes, M. L. Bissell, S. De Schepper, K. Dewolf, K. T. Flanagan, F. Le Blanc, B. A. Marsh, P. J. R. Mason, I. Matea, G. Neyens, J. Papuga, T. J. Procter, S. Rothe, G. S. Simpson, A. J. Smith, H. H. Stroke, D. Verney, P. M. Walker, K. D. A. Wendt, and R. T. Wood, "A dedicated decay-spectroscopy station for the collinear resonance ionization experiment at ISOLDE," *Nucl. Instrum. & Methods in Physics Research Section A: Accelerators, Spectrometers, Detectors and Associated Equipment*, vol. 707, pp. 35–39, Apr. 2013.

[99] P. Dendooven. PhD thesis, Afdeling Kern- en Stralingsfysica, KU Leuven, 1992.

[100] A. N. Andreyev, J. Elseviers, M. Huyse, P. Van Duppen, S. Antalic, A. Barzakh, N. Bree, T. E. Cocolios, V. F. Comas, J. Diriken, D. Fedorov, V. Fedosseev, S. Franchoo, J. A. Heredia, O. Ivanov, U. Köster, B. A. Marsh, K. Nishio, R. D. Page, N. Patronis, M. Seliverstov, I. Tsekhanovich, P. Van Den Bergh, J. Van De Walle, M. Venhart, S. Vermote, M. Veselsky,

C. Wagemans, T. Ichikawa, A. Iwamoto, P. Möller, and A. J. Sierk, "New type of asymmetric fission in proton-rich nuclei," *Phys. Rev. Lett.*, vol. 105, no. December, pp. 1–5, 2010.

[101] `http://www.ni.com/labview/`.

[102] R. E. Rossel, V. N. Fedosseev, B. A. Marsh, D. Richter, S. Rothe, and K. D. a. Wendt, "Data acquisition, remote control and equipment monitoring for ISOLDE RILIS," *Nucl. Instruments Methods Phys. Res. Sect. B Beam Interact. with Mater. Atoms*, vol. 317, pp. 557–560, 2013.

[103] I. Langmuir and K. H. Kingdon, "Thermionic Effects Caused by Vapours of Alkali Metals," *Proceedings of the Royal Society A: Mathematical, Physical and Engineering Sciences*, vol. 107, pp. 61–79, Jan. 1925.

[104] R. Neugart and G. Neyens, "Nuclear Moments," in *The Euroschool Lectures on Physics with Exotic Beams, Vol. II*, vol. 189, pp. 135–189, Springer Berlin Heidelberg, 2006.

[105] H. T. Duong, P. Juncar, S. Liberman, A. C. Mueller, R. Neugart, E. W. Otten, B. Peuse, J. Pinard, H. H. Stroke, C. Thibault, F. Touchard, J. L. Vialle, K. D. A. Wendt, and I. Collaboration, "First Observation of the Blue Optical Lines of Francium," *Europhysics Letters (EPL)*, vol. 3, pp. 175–182, Jan. 1987.

[106] `http://docs.scipy.org/doc/scipy/reference/odr.html`.

[107] S. Gheysen, G. Neyens, and J. Odeurs, "Calculated hyperfine spectra for in-source laser spectroscopy and deduced magnetic moments and isomer shifts of 68Cu and 70Cu isomeric states," *Phys. Rev. C - Nucl. Phys.*, vol. 69, pp. 064310–1, 2004.

[108] M. E. Debray, M. A. Cardona, D. Hojman, A. J. Kreiner, M. Davidson, J. Davidson, H. Somacal, G. Levinton, D. R. Napoli, S. Lenzi, G. de Angelis, M. De Poli, A. Gadea, D. Bazzacco, C. Rossi-Alvarez, and N. Medina, "Alternating parity bands in 87218Fr," *Phys. Rev. C*, vol. 62, p. 024304, July 2000.

[109] E. Browne, "Nuclear Data Sheets for A = 215,219,223,227,231," *Nuclear Data Sheets*, vol. 93, pp. 763–1061, Aug. 2001.

[110] M. J. G. Borge, D. G. Burke, H. Gietz, P. Hill, N. Kaffrell, W. Kurcewicz, G. Løvhøiden, S. Mattson, R. A. Naumann, K. Nybø, G. Nyman, and T. F. Thorsteinsen, "On the nuclear structure of 229Ra," *Nucl. Phys. A*, vol. 539, pp. 249–262, Mar. 1992.

[111] R. K. Sheline, P. Alexa, C. F. Liang, and P. Paris, "The configurations and level structure ofˆ{214} At," *Phys. Rev. C*, vol. 59, pp. 101–110, Jan. 1999.

[112] G. T. Ewan, E. Hagberg, B. Jonson, S. Mattsson, and P. Tidemand-Petersson, "New isomeric states in 218Fr and 214At," *Nuclear Physics A*, vol. 380, pp. 423–437, May 1982.

[113] L. M. Fraile, M. J. G. Borge, H. Mach, R. Boutami, A. J. Aas, B. Fogelberg, L. M. García-Raffi, I. S. Grant, K. Gulda, E. Hagebø, W. Kurcewicz, J. Kvasil, M. J. López, G. Løvhøiden, T. Martínez, B. Rubio, J. L. Taín, and O. Tengblad, "Persistence of octupole correlations in Ra," *Nucl. Phys. A*, vol. 686, pp. 71–108, Apr. 2001.

[114] V. a. Dzuba and V. V. Flambaum, "Calculation of energy levels and transition amplitudes for barium and radium," *J. Phys. B At. Mol. Opt. Phys.*, vol. 40, pp. 227–236, Jan. 2007.

[115] C. Ekström, S. Ingelman, G. Wannberg, and M. Skarestad, "Hyperfine structure, nuclear spins and moments of short-lived nuclides studied by on-line atomic-beam magnetic resonance techniques," *Hyperfine Interactions*, vol. 4, no. 1-2, pp. 165–169, 1978.

[116] E. Gomez, S. Aubin, L. A. Orozco, G. D. Sprouse, E. Iskrenova-Tchoukova, and M. S. Safronova, "Nuclear Magnetic Moment of Fr210: A Combined Theoretical and Experimental Approach," *Phys. Rev. Letters*, vol. 100, p. 172502, May 2008.

[117] L. W. Wansbeek, S. Schlesser, B. K. Sahoo, A. E. L. Dieperink, C. J. G. Onderwater, and R. G. E. Timmermans, "Charge radii of radium isotopes," *Phys. Rev. C*, vol. 86, p. 015503, July 2012.

[118] J. Papuga. PhD thesis, KU Leuven, 2015. Available at https://lirias.kuleuven.be/handle/123456789/489388.

[119] E. Caurier, G. Martinez-Pinedo, and F. Nowacki, "The shell model as a unified view of nuclear structure," *Rev. Mod. Phys.*, vol. 77, no. 2, pp. 427–488, 2005.

[120] P. Ring and P. Schuck, *The Nuclear Many-Body Problem.* Springer-Verlag New York, 1980.

[121] A. Bohr and B. R. Mottelson, *Nuclear Structure Vol II.* World Scientific Publishing, 1998.

[122] G. Leander, R. Sheline, and P. Möller, "The breaking of intrinsic reflection symmetry in nuclear ground states," *Nuclear Physics A*, vol. 388, pp. 452–476, 1982.

[123] R. K. Sheline, J. Kvasil, C. F. Liang, and P. Paris, "Reflection asymmetry in the odd-odd nucleus 224Ac," 1993.

[124] R. Casten, *Modern Theories of Nuclear Moments.* Oxford University Press Inc, 1990.

[125] I. Ragnarsson and S. G. Nilsson, *Shapes and Shells in Nuclear Structure.* Cambridge University Press, 2005.

[126] A. Faessler, "What can nuclear physics learn from nuclear moments?," *Hyperfine Interact.*, vol. 9, pp. 3–18, 1981.

[127] S. Wong, *Introductory Nuclear Physics, 2nd Edition.* Wiley-VCH, 1998.

[128] A. Voss, M. R. Pearson, J. Billowes, F. Buchinger, B. Cheal, J. E. Crawford, A. A. Kwiatkowski, C. D. P. Levy, and O. Shelbaya, "First Use of High-Frequency Intensity Modulation of Narrow-Linewidth Laser Light and Its Application in Determination of ˆ{206,205,204}Fr Ground-State Properties," *Phys. Rev. Lett.*, vol. 111, p. 122501, Sept. 2013.

[129] P. Möller and J. Rayford Nix, "Atomic masses and nuclear ground-state deformations calculated with a new macroscopic-microscopic model," *At. Data Nucl. Data Tables*, vol. 26, pp. 165–196, Mar. 1981.

[130] C. Ekström, L. Robertsson, and A. Rosén, "Nuclear and Electronic g-Factors of 211Fr, Nuclear Ground-State Spin of 207Fr and the Nuclear Single-Particle Structure in the Range 207-228Fr," *Physica Scripta*, vol. 34, pp. 624–633, 1986.

[131] I. Ahmad, J. Gindler, M. Carpenter, D. Henderson, E. Moore, R. Janssens, I. Bearden, and C. Foster, "Level structure of the odd-odd nucleus 22489Ac," vol. 576, no. 2, pp. 246–266, 1994.

[132] Y. AKOVALI, "Nuclear Data Sheets for A = 217," *Nucl. Data Sheets*, vol. 100, pp. 141–178, Sept. 2003.

[133] A. Byrne, R. Müsseler, H. Hübel, K. Maier, and H. Kluge, "Quadrupole moments of isomeric states in 213Fr and 212Fr," 1990.

[134] M. Kmiecik, A. Maj, J. Gerl, G. Neyens, L. Atanasova, D. L. Balabanski, F. Becker, P. Bednarczyk, G. Benzoni, N. Blasi, A. Bracco, S. Brambilla, L. Caceres, F. Camera, M. Ciemala, F. C. L. Crespi, S. K. Chamoli, S. Chmel, J. M. Daugas, P. Detistov, P. Doornenbal, G. Georgiev,

K. Gladnishki, M. Górska, H. Grawe, J. Grebosz, M. Hass, R. Hoischen, G. Ilie, M. Ionescu-Bujor, J. Jolie, I. Kojuharov, A. Krasznahorkay, R. Kulessa, M. Lach, S. Lakshmi, S. Leoni, G. L. Bianco, R. Lozeva, K. H. Maier, S. Mallion, K. Mazurek, W. Meczynski, B. Million, D. Montanari, S. Myalski, C. Petrache, M. Pfützner, S. Pietri, Z. Podolyák, W. Prokopowicz, D. Rudolph, N. Saito, T. R. Saito, A. Saltarelli, G. S. Simpson, J. Styczen, N. Vermeulen, E. Werner-Malento, O. Wieland, H. J. Wollersheim, and M. Zieblinski, "Spin-alignment and g-factor measurement of the Iπ = 12+ isomer in 192Pb produced in the relativistic-energy fragmentation of a 238U beam," *Eur. Phys. J. A*, vol. 45, no. 2, pp. 153–158, 2010.

[135] G. Neyens, M. Rajabali, and K. Flanagan, "Collinear resonant ionization spectroscopy for neutron rich copper isotopes.," Tech. Rep. CERN-INTC-2011-052. INTC-P-316, CERN, Geneva, Oct 2011.

[136] T. E. Cocolios, K. Flanagan, and K. M. Lynch, "Study of the stability of the gallium isotopes beyond the N = 50 neutron shell closure," Tech. Rep. CERN-INTC-2013-010. INTC-P-375, CERN, Geneva, May 2013. Requesting 2 runs of respectively 18 and 15 shifts Requires ISCOOL Requires neutron convertor Requesting ISOLDE DigiDAQ.

[137] K. M. Lynch, "Collinear resonance ionization spectroscopy of radium ions," Tech. Rep. CERN-INTC-2014-043. INTC-P-413, CERN, Geneva, May 2014.

[138] M. Bender, G. F. Bertsch, and P.-H. Heenen, "Global study of quadrupole correlation effects," *Phys. Rev. C*, vol. 73, p. 034322, Mar. 2006.

FACULTY OF SCIENCE
DEPARTMENT OF PHYSICS AND ASTRONOMY
INSTITUTE FOR NUCLEAR AND RADIATION PHYSICS
Celestijnenlaan 200D box 2418
3001 Leuven